12-2016

Innovative Electrode Nanocomposites for Energy Storage and Conversion Systems

Yiran Wang
University of Tennessee, Knoxville, ywang160@vols.utk.edu

To the Graduate Council:

I am submitting herewith a dissertation written by Yiran Wang entitled "Innovative Electrode Nanocomposites for Energy Storage and Conversion Systems." I have examined the final electronic copy of this dissertation for form and content and recommend that it be accepted in partial fulfillment of the requirements for the degree of Doctor of Philosophy, with a major in Chemical Engineering.

<div align="right">Zhanhu Guo, Major Professor</div>

We have read this dissertation and recommend its acceptance:

Robert M. Counce, Dibyendu Mukherjee, Bin Hu

<div align="right">Accepted for the Council:
Carolyn R. Hodges</div>

<div align="right">Vice Provost and Dean of the Graduate School</div>

(Original signatures are on file with official student records.)

Innovative Electrode Nanocomposites for Energy Storage

and Conversion Systems

A Dissertation Presented for the

Doctor of Philosophy

Degree

The University of Tennessee, Knoxville

Yiran Wang

December 2016

Acknowledgements

My parents' and my younger sister's support always surround me all through my Ph.D study time and I cannot find any better words to describe my great thankfulness to them. They always care about me no matter what I am confronted with and help me to solve issues I meet. They may not know exactly what I am working on, but they offered and will continue to offer me their unconditionally love and caring. My family member, my aunt, uncle, cousins and my grandma, they are always supporting me and encouraging me with their best wishes.

Abstract

Nanocomposites emerged as suitable alternatives for electrode materials, are defined as "two or more materials with different properties remain separate and distinct on a macroscopic level within one unity and with any dimension in any phase less than 100 nm". Recently, polymer/carbon based nanocomposites have attracted significant research interests for energy applications due to their multi-functionalities, improved structure stability and ease of production. This dissertation work focusing on the development of innovative electrode nanocomposites for proton exchange membrane fuel cell, supercapacitor and electrochromic applications.

Chapter 1 is an introduction. Chapter 2 & 3 focus on the synthesis of Pd-based nanocatalysts for EOR [ethanol oxidation reaction]. The effect of Pd loading in Pd/MWNTs [multi-walled carbon nanotubes], the conversion of Pd precursor and the variation of functionalized carboxylic groups on tube wall surface have been investigated through varying precursor ratios. A follow-up work focusing on integrating E [oxyphilic metal] and MO [metal oxides] into Pd/MWNTs nanocatalysts proceeds in Chapter 3. Ultrafine FePd nanoalloys deposited on γ-Fe_2O_3 [gamma iron oxides], FePd-Fe_2O_3, anchored on MWNTs, FePd-Fe_2O_3/MWNTs, have been successfully synthesized for EOR. A 3.65 fold increase of peak current density compared with that of Pd/MWNTs was observed in cyclic voltammetry after normalizing to Pd mass. Chapter 4 & 5 focus on the synthesis of electrode nanocomposites for supercapacitor and electrochromic applications, hybrid PANI [polyaniline] and $MnFe_2O_4$ [manganese iron oxide] nanocomposites film has been successfully synthesized for combined electrochromic and energy storage applications. The synthesized hybrid film exhibited enhanced electrochromic and energy storage performances compared to pristine PANI film due to the synergistic effect between the nanofillers and PANI matrix, nanofiller resulted porous structure of PANI and energy storage contribution of

MnFe$_2$O$_4$. Chapter 5 presents a facile hydrothermal method to enhance the energy storage property of graphene by employing KOH activation and N-doping processes. The synthesized graphene exhibited largely enhanced capacitance (186.63 F/g) and cycling stability compared with that of N-G [nitrogen doped graphene, 50.88 F/g] and AG [activated graphene, 58.38 F/g] due to the increased defects on graphene sheet and the introduced active N defects. Conclusions and future work are provided in Chapter 6.

Table of Contents

List of Tables

List of Figures

List of Scheme

Chapter 1 Introduction

1.1. Introduction

Given the dearth of fossil fuel and increasing environmental pollution, it is urgent to supply our society with clean and efficient power sources. A practical path to achieve significantly reduced carbon emissions in current transportation system is to find alternative fuels to gasoline and coal, as well as alternative power devices to internal combustion engine.[1,2] Nowadays, sustainable energy from renewable sources such as wind, hydroelectric, geothermal, biological, nuclear, and solar are emerging as promising alternatives due to their numerous merits. However, the intermittent nature of these renewable energy resources force the development of reliable energy storage systems to store and supply energy in a stable manner. Electrochemical energy storage systems including electrochemical capacitors (ECs), batteries, and fuel cells are attracting dramatic attention as proper candidates. Nanocomposites, emerging as suitable alternatives for electrode materials, are defined as "two or more materials with different properties remain separate and distinct on a macroscopic level within one unity and with any dimension in any phase less than 100 nm". Recently, polymer/carbon based nanocomposites have attracted significant research interests for energy storage and conversion applications due to their multi-functionalities, improved structure stabilities and ease of production. Over the past decades low-temperature fuel cells that can directly electro-oxidize small organic molecules for electricity with a high thermodynamic efficiency (up to 97%), have demonstrated as an alternative path to power supply.[3] However, sluggish reaction kinetics at the anode where catalysts oxidize small organic molecules into positively charged ions and negatively charged electrons is a main limitation for the commercialization of fuel cells. Even though numerous work has been devoted to tailoring the particle size and growth of palladium (Pd) which have been recognized more advantageous catalytic metal than platinum (Pt) for anodic nanocatalysts, the performance of the anodic catalysts

2

is still hindered by their easy agglomeration, easy poisoning and low specific area.[4,5] Nowadays, solid substrates such as carbon supports have been demonstrated to be effective for enhancing the utilization of metals, employing solid substrates can not only improve the physicochemical stability of Pd but also increase the specific catalytic activity of Pd.[6] Furthermore, oxyphilic metal (E) and metal oxide (MO) have also been demonstrated to be effective to minimize the usage of Pd. In addition, the electro-structure of Pd can be largely altered through d-band hybridizing with E and interfacial bonding with MO.[7–10] Therefore, fabricating catalytic nanocomposites integrating all these components (E, MO and C) appears to be a promising approach to improve the catalytic performance of Pd due to the increased Pd utilization, improved electronic structure and optimized existing status.

As a promising type of sustainable and renewable energy storage device, electrochemical capacitors have numerous merits such as long cycle life, lower maintenance cost and environmental friendliness.[11,12] They have been widely applied in portable electronics, hybrid electric vehicles, memory backup systems, and large industrial equipment.[13–15] The high power density vs. batteries and the high energy density vs. conventional capacitors enable electrochemical capacitors to be a good choice to fill in the gap between the batteries and the conventional electrostatic capacitors.[16,17] Electrochemical capacitors can be mainly classified into electric double layer capacitors (EDLCs) and pseudocapacitors. Different carbon nanomaterials such as activated carbon,[18] carbon black,[19,20] carbon onions,[21,22] carbon nanotubes[23,24] and carbon nanofibers[25,26] have been widely employed for EDLCs. All of these electrode materials exhibit excellent cycling stability but low capacitances. In contrast, metal oxides[27,28] and conducting polymers[29,30] are usually used in pseudocapacitors due to their high capacitance. However, the poor cycle life is the main limitation because the process are always accompanied with the swelling and

shrinkage of the electrodes.[31–33] Therefore, combining different components to synthesize the electrode nanocomposites is a promising route to improve the energy storage performance.

Meanwhile, electrochromism, as a phenomenon where the color of a material is changed through an electrochemical reaction, is also attractive over the last few years.[34,35] Reversible and persistent color change of the electrochromic materials is controlled by a temporarily applied electrical potential,[36] which consume low energy and have wide applications due to the energy saving property. These applications include smart windows, display devices, vehicle sunroofs, and antiglare mirrors for cars,[37–39] offering a paradigm for improving the energy efficiency of our daily comforts.[40] Several kinds of materials classified as transition-metal oxides, mixed valence materials, organic molecules, and conjugated polymers have all been reported to show electrochromic properties.[41–43] However, in order to increase the range of colors available, multiple electrochromic materials or "multicoloring" are employed to reproduce high-quality color in such devices. One simple method is mixing two discrete colors, which may be achieved by using two electrochromes, with complementary colors deposited onto different working electrodes.[38,44,45] In addition, since it is imperative for these materials that ions be transported into and out of the film during the redox chemistry so as to maintain electroneutrality.[46] Faster ion transport should directly enhance the switching rate of the electrochromic thin films. Therefore, preparing electrochromic nanocomposites films with nanofillers resulted uniform and tunable porosity is an attractive choice that enables facile ion transport and ensures that the entire film is redox-active.[34]

1.2. Mechanism

A fuel cell is a device that converts the chemical energy from a fuel into electricity through a chemical reaction of positively charged hydrogen ions with oxygen or another oxidizing agent. Figure 1.1 exhibits the working principle of direct methanol fuel cells (DMFCs) in acid and
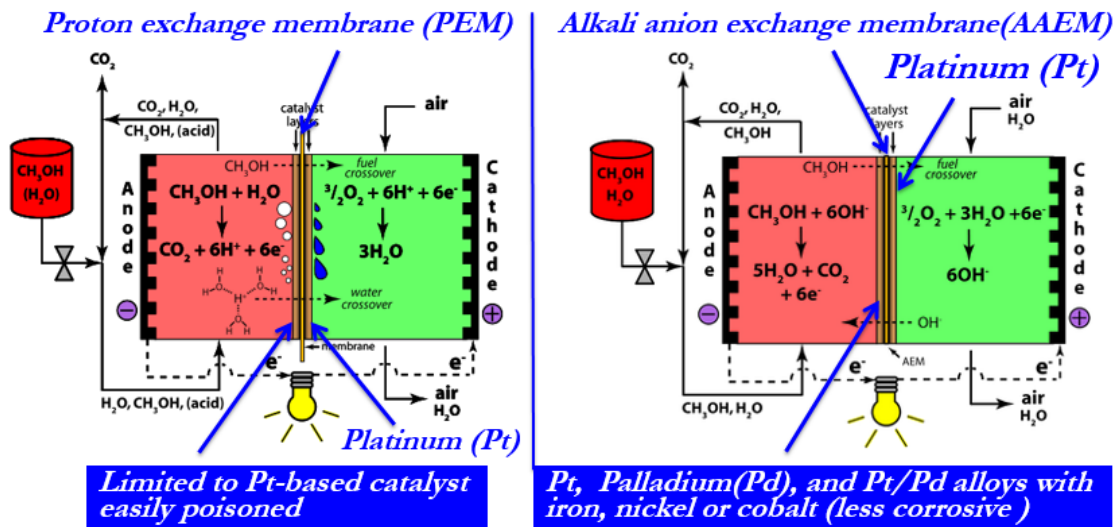
Figure 1.1. Schematic representation of the mechanism of DMFCs in acid medium (left) and alkaline medium (right).

alkaline media, the configurations are shown with specific anodic and cathodic reactions. Both anodic reactions produce CO_2 from the oxidation of methanol with other products transferring through the membrane to the other side to react and maintain a balance. Electrons are produced simultaneously and flow through a closed circuit to give electricity. For the cathodic reaction, Pt is well recognized as the best element for cathodic catalysts. For anodic catalysts, it is mainly limited to Pt-based catalyst in acid medium. However, it is allowable to use other catalytic metals such as Pd, and Pd/Pt alloys with Ni, Co and Fe due to the less corrosive environment of alkaline medium. Furthermore, although Pt has been widely used for methanol oxidation reaction, it can be easily poisoned by the CO intermediates species produced in acidic medium. In contrast, Pd as a much lower-cost catalyst can exhibit an increased CO tolerance stability and higher catalytic activity in alkaline medium, which provides a prior choice for methanol oxidation reaction.

A supercapacitor (sometimes ultracapacitor, formerly EDLC is a high-capacity electrochemical capacitor with capacitance values much higher than other capacitors (but lower voltage limits). Supercapacitor bridges the gap between electrolytic capacitors and rechargeable batteries. According to the working principle, capacitor can be classified as EDLC and pseudocapacitor or a Faradic supercapacitor (FS). The greatest advantage of EDLC is long life time while it suffers from its low energy density. The working principle, shown left in Figure 1.2 solely operates by electrostatic accumulation of surface charge. The EDLC capacitance comes from electrode materials, where an excess or a deficit of electric charges is accumulated on the electrode surfaces. Electrolyte ions with counterbalancing charge are built up on the electrolyte side in order to meet electroneutrality. Pseudocapacitor is based on interface reaction, therefore, it obtains much larger energy density, typically 10-100 times larger than EDLC, while it suffers from its low power density due to the slower faradic process. The life time is also relatively short due
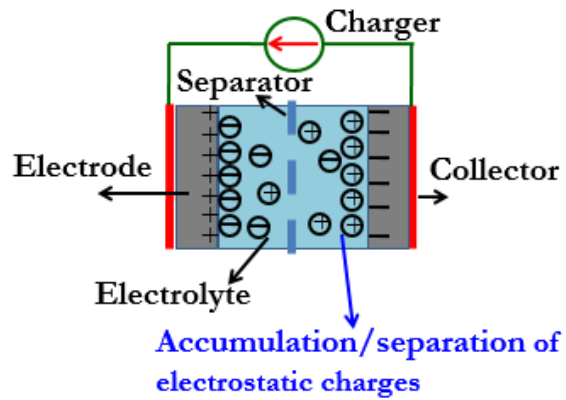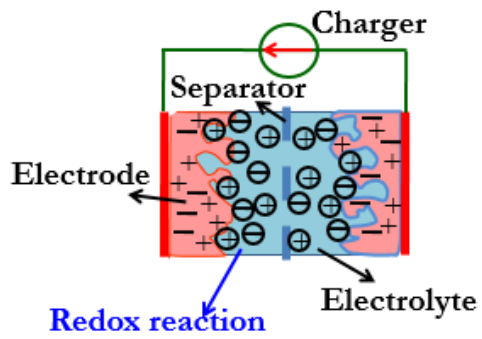
Figure 1.2. Schematic representation of the mechanism of supercapacitor as EDLCs (left) and pseudocapacitor (right).

to electrode microstructure damage during charge/discharge. As seen in the right part of Figure 1.2, when a potential is applied to a FS, fast and reversible redox reactions take place on the electrode materials and involve the passage of charge across the double layer, resulting in faradaic current passing through the supercapacitor.

Electrochromism is defined as "a reversible color change of a material induced by the reduction or oxidation after applying a proper electric potential" Figure 1.3 shows a typical electrochromic phenomenon displaying different colors on the left with potential ranging from -2.5 to 2.5 V. Conjudgated conducting polymers such as Polyaniline (PANI), Polypyrrole (PPy), Polythiophenes (PThs) and their derivatives have attracted significant interest due to their electrochromic properties. The color switching is caused by varying transition states arising from reversible redox reactions in the polymers.[47] PANI as a typical electrochromic material possesses a lot merits such as relatively higher electrochemical and thermal stabilities, tunable properties, low cost, and high conductivity.[48,49] In PANI, there are LB (fully reduced), EB (protonation of PANI's intermediate oxidation state), and PB (full oxidized) three states and different colors such as white, yellow, green and blue could be observed at different states. In addition, the pseudocapacitance arising from the versatile redox reactions and corresponding color change make PANI a promising candidate for combined supercapacitor and electrochromic applications.[50]

1.3. Dissertation Overview

This dissertation research is devoted to the development of innovative electrode nanocomposites for energy storage & conversion system applications such as proton exchange membrane fuel cells, supercapacitors and electrochromics. To achieve this goal, a wide range of nanostructures have been fabricated and investigated. The mechanistic picture as well as the important parameters/conditions that dominate their electrochemical performances have also been
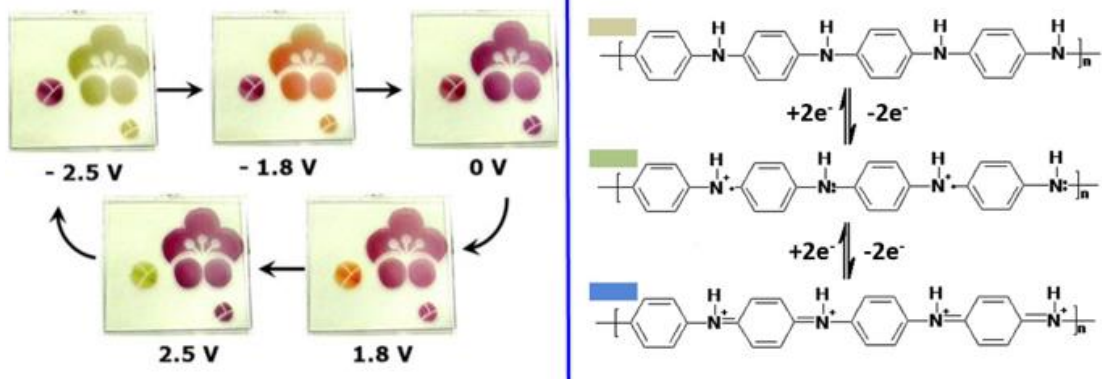
Figure 1.3. Schematic representation of the electrochromic phenomenon (left) and the mechanism of PANI (right).

studied. Chapter 1 is the introduction part, Chapter 2 & 3 aim at synthesizing highly active anodic Pd-based nanocatalysts by optimizing Pd loading and introducing E, MO and C toward ethanol oxidation reaction (EOR). A facile one-pot solution based synthesis method namely, thermal decomposing palladium(II) acetylacetonate ($Pd(acac)_2$) and other metal precursors in a refluxing organic solution in the presence of carbon substrates have been employed to synthesize a series of hierarchical nanocatalysts. The purpose of these nanocatalysts is to improve the anode reaction kinetics in fuel cells and lower the catalysts cost. For Pd/MWNTs (Pd decorated multi-walled carbon nanotubes), the Pd loading effect, conversion of $Pd(acac)_2$, variation of the functionalized -COOH on the tube wall surface, and catalytic activity of Pd/MWNTs have been investigated with the variation of precursor ratios. The basic concept of this method is that this thermal decomposition process can produce metastable nanostructures with controlled morphology, structure and composition/alloying nanocatalysts without adding any reducing agents, surfactants or stabilizing agents that are potentially harmful for the catalytic activity of Pd. For chapter 4, $PANI/MnFe_2O_4$ nanocomposites thin films have been successfully prepared by a combined spin coating and electropolymerization method and used for combined supercapacitor & electrochromic application. The synthesized $PANI/MnFe_2O_4$ films is demonstrated to enhance the energy storage and electrochromic properties of PANI after introducing $MnFe_2O_4$ nanofillers. The property improvements are probably due to the formed certain relationships between the $MnFe_2O_4$ and PANI matrix as well as the resulted much porous structure of $PANI/MnFe_2O_4$ film comparing with pristine PANI film. Chapter 5 presents a facile hydrothermal method to synthesize N-AG to enhance the energy storage property of graphene by employ KOH etching and nitrogen-doping process. The expected properties and the possibility of this scalable synthesis method make N-AG an attractive candidate for both fundamental study and potential industrial applications in catalysis,

10

adsorption, energy storage, and energy conversion systems. Conclusions and future work are provided in Chapter 6.

1.4. References

1. N. Armaroli and V. Balzani, Angew. Chem. Int. Ed., 2007, 46, 52–66.
2. J. R. Rostrup-Nielsen, Catal. Rev., 2004, 46, 247–270.
3. Y. Li, W. Gao, L. Ci, C. Wang and P. M. Ajayan, Carbon, 2010, 48, 1124–1130.
4. X. Chen, Y. Hou, H. Wang, Y. Cao and J. He, J. Phys. Chem. C, 2008, 112, 8172–8176.
5. X. Chen, G. Wu, J. Chen, X. Chen, Z. Xie and X. Wang, J. Am. Chem. Soc., 2011, 133, 3693–3695.
6. B. Yoon and C. M. Wai, J. Am. Chem. Soc., 2005, 127, 17174–17175.
7. P. Mukherjee, P. S. Roy, K. Mandal, D. Bhattacharjee, S. Dasgupta and S. K. Bhattacharya, Electrochimica Acta, 2015, 154, 447–455.
8. L. Zhao, S. Wang, Q. Ding, W. Xu, P. Sang, Y. Chi, X. Lu and W. Guo, J. Phys. Chem. C, 2015, 119, 20389–20400.
9. C. Xu, Z. Tian, P. Shen and S. P. Jiang, Electrochimica Acta, 2008, 53, 2610–2618.
10. L. M. Petkovic, S. N. Rashkeev and D. M. Ginosar, Catal. Today, 2009, 147, 107–114.
11. H. Wang, E. Zhu, J. Yang, P. Zhou, D. Sun and W. Tang, J. Phys. Chem. C, 2012, 116, 13013–13019.
12. W. Fan, C. Zhang, W. W. Tjiu, K. P. Pramoda, C. He and T. Liu, ACS Appl. Mater. Interfaces, 2013, 5, 3382–3391.
13. Z. Gao, W. Yang, J. Wang, B. Wang, Z. Li, Q. Liu, M. Zhang and L. Liu, Energy Fuels, 2013, 27, 568–575.
14. S. Dhibar and C. K. Das, Ind. Eng. Chem. Res., 2014, 53, 3495–3508.
15. C. Z. Yuan, B. Gao, L. F. Shen, S. D. Yang, L. Hao, X. J. Lu, F. Zhang, L. J. Zhang and X. G. Zhang, Nanoscale, 2011, 3, 529–545.
16. Y. Yin, C. Liu and S. Fan, J. Phys. Chem. C, 2012, 116, 26185–26189.
17. J. Zhang and X. S. Zhao, ChemSusChem, 2012, 5, 818–841.
18. G. Xu, C. Zheng, Q. Zhang, J. Huang, M. Zhao, J. Nie, X. Wang and F. Wei, Nano Res., 2011, 4, 870–881.
19. P. Kossyrev, J. Power Sources, 2012, 201, 347–352.
20. N. Jäckel, D. Weingarth, M. Zeiger, M. Aslan, I. Grobelsek and V. Presser, J. Power Sources, 2014, 272, 1122–1133.
21. J. K. McDonough, A. I. Frolov, V. Presser, J. Niu, C. H. Miller, T. Ubieto, M. V. Fedorov and Y. Gogotsi, Carbon, 2012, 50, 3298–3309.
22. Y. Gao, Y. S. Zhou, M. Qian, X. N. He, J. Redepenning, P. Goodman, H. M. Li, L. Jiang and Y. F. Lu, Carbon, 2013, 51, 52–58.
23. B. Kim, H. Chung and W. Kim, Nanotechnology, 2012, 23, 155401.
24. Y. J. Kang, H. Chung, C.-H. Han and W. Kim, Nanotechnology, 2012, 23, 65401.
25. Y.-H. Hsu, C.-C. Lai, C.-L. Ho and C.-T. Lo, Electrochimica Acta, 2014, 127, 369–376.
26. L.-F. Chen, X.-D. Zhang, H.-W. Liang, M. Kong, Q.-F. Guan, P. Chen, Z.-Y. Wu and S.-H. Yu, ACS Nano, 2012, 6, 7092–7102.
27. H. Wang, Z. Xu, H. Yi, H. Wei, Z. Guo and X. Wang, Nano Energy, 2014, 7, 86–96.
28. Y. Jiang, P. Wang, X. Zang, Y. Yang, A. Kozinda and L. Lin, Nano Lett., 2013, 13, 3524–3530.
29. H. Wei, Y. Wang, J. Guo, X. Yan, R. O'Connor, X. Zhang, N. Z. Shen, B. L. Weeks, X. Huang, S. Wei and Z. Guo, ChemElectroChem, 2015, 2, 119–126.

30. Y. Zhao, H. Wei, M. Arowo, X. Yan, W. Wu, J. Chen, Y. Wang and Z. Guo, Phys Chem Chem Phys, 2015, 17, 1498–1502.
31. K. Kai, Y. Kobayashi, Y. Yamada, K. Miyazaki, T. Abe, Y. Uchimoto and H. Kageyama, J. Mater. Chem., 2012, 22, 14691.
32. G. A. Snook, P. Kao and A. S. Best, J. Power Sources, 2011, 196, 1–12.
33. J. Yang, T. Lan, J. Liu, Y. Song and M. Wei, Electrochimica Acta, 2013, 105, 489–495.
34. C.-W. Kung, T. C. Wang, J. E. Mondloch, D. Fairen-Jimenez, D. M. Gardner, W. Bury, J. M. Klingsporn, J. C. Barnes, R. Van Duyne, J. F. Stoddart, M. R. Wasielewski, O. K. Farha and J. T. Hupp, Chem. Mater., 2013, 25, 5012–5017.
35. P. Monk, R. Mortimer and D. Rosseinsky, Electrochromism and Electrochromic Devices, Cambridge University Press, Cambridge, 2007.
36. M. R. J. Scherer, L. Li, P. M. S. Cunha, O. A. Scherman and U. Steiner, Adv. Mater., 2012, 24, 1217–1221.
37. H. W. Heuer, R. Wehrmann and S. Kirchmeyer, Adv. Funct. Mater., 2002, 12, 89–94.
38. R. J. Mortimer, A. L. Dyer and J. R. Reynolds, Displays, 2006, 27, 2–18.
39. R. Baetens, B. P. Jelle and A. Gustavsen, Sol. Energy Mater. Sol. Cells, 2010, 94, 87–105.
40. F. Lin, D. Nordlund, T.-C. Weng, D. Sokaras, K. M. Jones, R. B. Reed, D. T. Gillaspie, D. G. J. Weir, R. G. Moore, A. C. Dillon, R. M. Richards and C. Engtrakul, ACS Appl. Mater. Interfaces, 2013, 5, 3643–3649.
41. P. M. Beaujuge and J. R. Reynolds, Chem. Rev., 2010, 110, 268–320.
42. V. K. Thakur, G. Ding, J. Ma, P. S. Lee and X. Lu, Adv. Mater., 2012, 24, 4071–4096.
43. J. M. Wang, X. W. Sun and Z. Jiao, Materials, 2010, 3, 5029–5053.
44. E. Unur, J.-H. Jung, R. J. Mortimer and J. R. Reynolds, Chem. Mater., 2008, 20, 2328–2334.
45. T. Yashiro, S. Hirano, Y. Naijoh, Y. Okada, K. Tsuji, M. Abe, A. Murakami, H. Takahashi, K. Fujimura and H. Kondoh, SID Symp. Dig. Tech. Pap., 2011, 42, 42–45.
46. C.-Y. Tseng, C.-W. Hu, K.-C. Huang, L.-C. Chang, R. Vittal and K.-C. Ho, Electrochimica Acta, 2013, 101, 232–237.
47. H. Wei, X. Yan, S. Wu, Z. Luo, S. Wei and Z. Guo, J. Phys. Chem. C, 2012, 116, 25052–25064.
48. S. Bhadra, D. Khastgir, N. K. Singha and J. H. Lee, Prog. Polym. Sci., 2009, 34, 783–810.
49. S. Bhadra, N. K. Singha and D. Khastgir, J. Appl. Polym. Sci., 2007, 104, 1900–1904.
50. H. Wei, J. Zhu, S. Wu, S. Wei and Z. Guo, Polymer, 2013, 54, 1820–1831.

Chapter 2 Multiwalled Carbon Nanotubes Composited with

Palladium Nanocatalysts for Highly Efficient Ethanol Oxidation

This chapter is revised based on a paper first authored by myself.

My priority contribution to this paper include (i) development of the problem into a work, (ii) identification of the study area and objectives, (iii) design and conducting of the experiment, (iv) gathering and rendering literature, (v) processing and analysis the experimental data, (vi) pulling various contributions into a single paper. (vii) writing the paper.

Abstract

Carboxyl multi-walled carbon nanotubes (MWNTs-COOH) decorated with different Pd nanoparticle loadings were synthesized by thermally decomposing different amounts of palladium(II) acetylacetonate (Pd(acac)$_2$) in a refluxing xylene solution with a fixed amount of dispersed MWNTs-COOH. The increased ratio of D band/G band in Raman spectroscopy and the decreased area ratio of oxygen containing groups (COOH, C-O and C=O) to C-C group in X-ray photoelectron spectroscopy (XPS) suggested an increased occupation of defects on multi-walled carbon nanotubes (MWNTs). Transmission electron microscope (TEM) revealed different distributions of Pd nanoparticles (NPs) on the MWNTs with the variation of Pd(acac)$_2$ amount and the particle size increased with increasing the Pd loading. A relatively higher conversion of Pd(acac)$_2$ to Pd (76.21 %) was achieved when the initial precursor ratio of Pd(acac)$_2$ to MWNTs was 2 : 1 (product donates as Pd/MWNTs-(2:1)). The Pd/MWNTs-(2:1) catalysts were demonstrated to exhibit the most efficient performance towards ethanol oxidation reaction (EOR) among all the precursor ratios. This catalytic performance is characterized by the highest Pd mass-

based peak current density (1.23 A/mg $_{Pd}$) and stable current density (0.175 A/mg $_{Pd}$) as tested by cyclic voltammetry (CV) and chronoamperometry (CA). However, both reduced charge-transfer resistance and increased reaction kinetics with increasing the Pd loading were obtained by electrochemical impedance spectroscopy (EIS) and Tafel characterization.

2.1. Introduction

Nowadays, Pd as a substitute of Pt is widely used as catalysts in low temperature fuel cells, which have a wide range of promising applications such as portable power generation, stationary power generation, and power for transportation.[1-3] Ethanol as an excellent alternative to methanol has been deployed nowadays due to its nontoxicity,[4] ease of production from agricultural products/fermentation of biomass, high energy density,[5, 6] and low fuel crossover that is often encountered in methanol-based fuel cells.[7-9] Due to similar properties to Pt (same group in the periodic table, same fcc crystal structure, comparable atomic size) and certain advantages compared with Pt (lower price, greater resistance to CO, and inherently faster kinetics in alkaline medium), the Pd-based catalysts are attracting more interests in ethanol oxidation reaction (EOR) in alkaline electrolyte.[10] In addition, the onset potential and peak current density of Pd observed in the cyclic voltammetry for EOR are shifted negatively and much higher than those of Pt in alkaline media.[11, 12]

The preparation of Pd with controllable nanostructures and enhanced catalytic properties is the key to realize the final commercialization of fuel cells. The size control and full utilization of Pd atoms are largely prohibited due to the easy agglomeration of naked Pd NPs.[13] Although surfactants or polymers can facilitate the formation of uniform Pd nanoparticles (Pd NPs) with narrow size distribution,[14, 15] the covered organic materials can largely affect the catalytic activities due to the 'unclean' surface.[16] Introducing substrate to disperse Pd NPs is becoming more and more desirable since this method can not only facilitate the dispersion of Pd NPs but also incorporate the advantages of substrate to the final composites.[17-22] Among the supporting materials, carbon nanotubes (CNTs) have attracted intense interest due to their excellent electronic properties, good physical and chemical stability, and large specific surface area.[23-25]

Functionalized oxygen containing groups on the tube wall surface are demonstrated to favor the dispersion of NPs and contribute to stable nanocomposites due to the covalent bonding.[26-28]

Great efforts have been devoted to develop facile and practical synthesis methods to achieve a high conversion of Pd precursor thus minimizing the synthesis cost.[16, 29, 30] With great concerns about the minimization of Pd usage, proper ratio between Pd precursor and CNTs is needed to achieve a high conversion of Pd precursor.[31-38] Since high electro-catalytic activity often calls for small and highly dispersed Pd particles,[39] it is not always true that more Pd on CNTs would give the higher specific activity of Pd. Particle size and distribution also vary with the amount of Pd on the tube wall surface thus leading to different nanostructures of Pd NPs.[40-46] Therefore, significant electro-catalytic activity should be assessed under the premise of minimizing the consumption of Pd precursors. The conversion of Pd precursor and the final Pd loading on CNTs should be simultaneously considered in order to obtain the highest specific activity of Pd and to meet the economic requirements. Varying the ratio between CNTs and Pd precursors is a feasible and effective way to synthesize catalysts with optimal loading due to its easy manipulation and the exclusion of any new additives. Currently, numerous work has been done to improve the performance of Pd/CNTs, including exploiting new synthesis methods,[47-50] introducing additive transition metals,[24, 51-54] or optimize the application conditions such as employing suitable electrolyte, applying optimal electrolyte composition and improving the working temperature.[12, 55, 56] However, the investigation of Pd loading effect on CNTs as a basic direction is of great significance for the practical usage and has not been specifically reported yet.

In this work, a facile one-pot solution based method using palladium acetylacetonate (Pd(acac)$_2$) as Pd precursor and carboxylic groups functionalized multi-walled nanotubes (MWNTs-COOH) as support was employed to synthesize multi-walled nanotubes decorated with

Pd nanocatalysts (Pd/MWNTs) with different Pd loadings. The loadings were achieved through varying the amount of Pd(acac)$_2$ with a fixed amount of MWNTs-COOH. The crystalline structure, particle size and morphology differences of the Pd NPs with different loadings were investigated by X-ray diffraction (XRD) and transmission electron microscopy (TEM). The variation of the defects on the tube wall surface caused by the deposition of Pd NPs was characterized by Raman spectroscopy and X-ray photoelectron spectroscopy (XPS). The loading of Pd and corresponding conversion of Pd(acac)$_2$ of each specific loading nanocatalyst were determined by thermogravimetric analysis (TGA). The electro-catalytic performances of these nanocatalysts were evaluated toward ethanol oxidation reaction (EOR) by cyclic voltammetry (CV), chronoamperometry (CA) and electrochemical impedance spectroscopy (EIS). The reaction kinetics were also studied using slow Linear sweep voltammetry (LSV) and Tafel polarization characterization to probe the Pd loading effect on EOR.

2.2. Experimental

2.2.1. Materials

Palladium (II) acetylacetonate (Pd(C$_5$H$_7$O$_2$)$_2$, 99%, Mw=304.64 g/mol), potassium hydroxide (KOH, BioXtra, ≥85% KOH basis), and ethanol (anhydrous, C$_2$H$_5$OH, ≥99.5%) were purchased from Sigma Aldrich. Solvent xylene (laboratory grade, ρ=0.87 g/cm^3) was purchased from Fisher Scientific. Carboxylic group functionalized multi-walled nanotubes (MWNTs-COOH) (**Stock#:** 1272YJF, content of MWNTs: ≥ 95 wt%, content of -COOH: 0.47-0.51 wt%, outside diameter: 50-80 nm, inside diameter: 5-15 nm, length: 10-20 μm) were provided by Nanostructured & Amorphous Materials, Inc. All the chemicals were used as-received without any further treatments.

2.2.2. Synthesis of Catalysts

A facile one-pot solution-based method was used to synthesize Pd/MWNTs with different Pd loadings. Briefly, 100.0 mg MWNTs-COOH were dispersed in 60 mL xylene in a 100-mL beaker under sonication for one hour. The mixture was then transferred to a 250-mL 3-neck flask and heated to reflux (~140 °C) in ~ 20 min. Different amount of Pd(acac)$_2$ as 0.05, 0.1, 0.2, 0.3 and 0.4 g (corresponding ratios of Pd(acac)$_2$ to MWNTs-COOH are 1:2, 1:1, 2:1, 3:1 and 4:1) was dissolved in 20 mL xylene in a 50-mL beaker under sonication for 10 min and then added to the refluxing MWNTs-COOH/xylene solution, which was refluxed continuously for additional 3 hours to complete the reaction. Finally, the solution was cooled down to room temperature naturally, filtered under vacuum and rinsed with ethanol and acetone 3 times, respectively. For the synthesis of bare Pd NPs, 20 mL sonicated Pd(acac)$_2$/xylene solution was added to 60 mL refluxing pure xylene and refluxed for 3 hours, the bare Pd NPs were collected by centrifugation and rinsed with ethanol and acetone for three times. All the final products (denoted as bare Pd NPs, Pd/MWNTs-1:2, Pd/MWNTs-1:1, Pd/MWNTs-1:2, Pd/MWNTs-1:3 and Pd/MWNTs-1:4) were collected after vacuum drying at 60 °C for 24 hours.

2.2.3. Preparation of Pd/MWNTs Working Electrode

Prior to each experiment, the working glassy carbon electrode with a diameter of 3 mm was successively polished with 1 and 0.05 μm alumina powders on a microcloth wetted with DI water to provide an electrode with a mirror-like surface. For the preparation of a catalyst coated electrode, 1.0 mg catalyst was added to 1.0 mL ethanol solution of nafion (the content of nafion is 0.1 wt%), then the mixture was treated with 30 min ultrasonication to form a uniform suspension. The obtained suspension (5 μL) was dropped on the surface of the well-treated glassy

carbon electrode. Finally, the resultant modified glassy carbon electrode was dried naturally at room temperature.

2.2.4. Characterizations

The crystal structure of Pd NPs in different nanocatalysts was characterized using X-ray diffraction (XRD) analysis carried out on a Bruker D8ADVANCE X-ray diffractometer equipped with a Cu Kα source ($\lambda = 0.154$ nm) at 40 kV and 30 mA. The 2θ angular region between 20 and 70 ° was explored at a scan rate of 1 ° min^{-1}.

Raman spectra were obtained using a Horiba Jobin-Yvon LabRam Raman confocal microscope with 785 nm laser excitation at a 1.5 cm^{-1} resolution at room temperature.

The thermal stability and final loading of Pd were determined by thermogravimetric analysis (TGA) using a TA instruments Q-500 at a heating rate of 10 ˚C min^{-1} and an air flow rate of 60 mL min^{-1} from 25 to 800˚C.

X-ray photoelectron spectroscopy (XPS) measurements were performed on a Kratos AXIS 165 XPS/AES instrument. The samples were scanned with a monochromatic Al X-ray source at the anode of 10 kV and beam current of 15 mA. The Pd peaks were deconvoluted into the components on a Shirley background.

The morphologies of the Pd/MWNTs nanocatalysts were obtained by transmission electron microscopy (TEM) using a field emission transmission electron microscope (TEM, JEOL 2010F), operated at an accelerating voltage of 200 kV. The samples were prepared by drying a drop of ethanol suspension on the carbon-coated copper TEM grids and dried in air.

2.2.5. Electrochemical Evaluations

The electrochemical experiments were conducted in a conventional three-electrode cell. The as-prepared glassy carbon electrode deposited with catalyst was used as the working electrode,

platinum wire as the counter electrode, and saturated calomel electrode (SCE) (0.241 V vs. SHE) connected to the cell through a Luggin capillary serving as reference electrode. All the potentials were referring to the SCE. All the electrochemical measurements were performed on an electrochemical working station VersaSTAT 4 potentiostat (Princeton Applied Research). Stable cyclic voltammogram (CV) curves were recorded after potential extended cycles in the potential range from -1.0 to 0.3 V. The chronoamperometry (CA) was performed at -0.4 V for EOR for a duration of 1000 s. The electrochemical impedance spectroscopy (EIS) was carried out in the frequency range from 100 000 to 0.1 Hz at a 5 mV amplitude at -0.3 V (vs. reference electrode) for EOR. Tafel polarization curves were obtained from the linear polarization curves conducted from -0.8 to -0.2 V with a scan rate of 0.5 mV/s and the current density was normalized to the geometric area of coated nanocatalysts.

2.3. Results and Discussions

2.3.1. XRD Analysis

Figure 2.1(a-e) shows the XRD patterns of Pd/MWNTs-1:2, Pd/MWNTs-1:1, Pd/MWNTs-2:1, Pd/MWNTs-3:1 and Pd/MWNTs-4:1. For all the five nanocatalysts, four main diffraction peaks as C (002) centering around 25.97˚, (JCPDS 26-1077), Pd (111), (200) and (220) centering around 40.01, 46.54 and 67.65˚, (JCPDS 88-2335), are clearly observed, indicating the successful deposition of Pd on MWNTs. For Pd/MWNTs-1:2, Pd/MWNTs-1:1 and Pd/MWNTs-2:1, Figure 2.1(a-c), enhanced intensities of Pd planes and decreased intensity of C (002) are clearly observed with increasing the amount of Pd(acac)$_2$, indicating an increased loading of Pd. However, no obvious variation is observed when the Pd precursor amount increasing further due to the saturation of Pd on MWNTs.
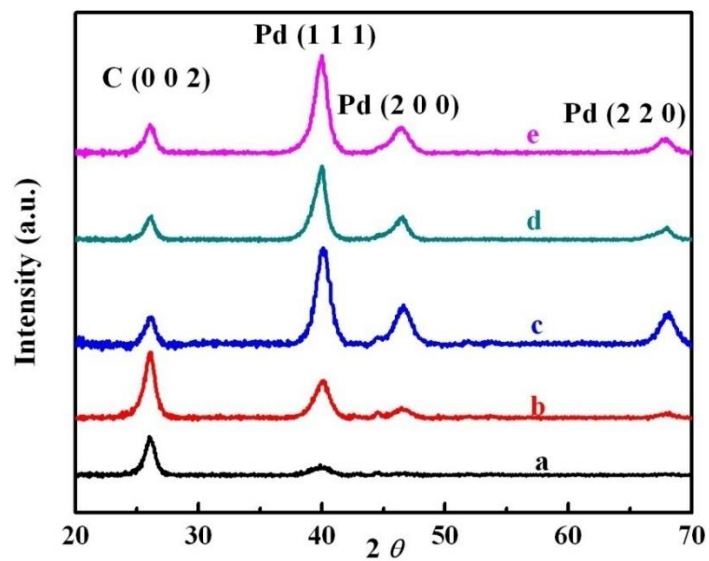
Figure 2.1. XRD patterns of (a) Pd/MWNTs-1:2, (b) Pd/MWNTs-1:1, (c) Pd/MWNTs-2:1, (d) Pd/MWNTs-3:1, and (e) Pd/MWNTs-4:1.

Finally, the Pd (111) plane is chosen to estimate the average crystallite size of the Pd NPs using Debye - Scherrer Equation (1)[57]

$$L = 0.89\lambda/(\beta\cos\theta_B) \tag{1}$$

where L is the particle size, λ is 1.5406 Å for the wavelength of Cu-Kα radiation, β is the full width at half-maximum (FWHM), and θ_B is the diffraction angle. The corresponding crystallite sizes of Pd/MWNTs-1:2, Pd/MWNTs-1:1, Pd/MWNTs-2:1, Pd/MWNTs-3:1 and Pd/MWNTs-4:1 are calculated to be 4.61, 5.53, 6.04, 6.67 and 6.33 nm, suggesting an increased particle size with increasing the Pd(acac)$_2$ precursor amount.

2.3.2. TEM Images

TEM is employed to further investigate the microstructure variation of Pd/MWNT-1:2, Pd/MWNTs-1:1, Pd/MWNTs-2:1 and Pd/MWNTs-4:1 in Figure 2.2(a-d), the top and bottom insets are the histogram and HRTEM of the corresponding nanocatalysts, respectively. For Pd/MWNTs-1:2, the Pd NPs with an ultra-small particle size of 3.45 nm are observed to be evenly distributed on the surface of tube wall due to the small amount of Pd(acac)$_2$ precursor, which is further confirmed by the bottom HRTEM. The average particle size is monotonously increased to 4.11, 6.02, and 6.62 nm for Pd/MWNTs-1:1, Pd/MWNTs-2:1 and Pd/MWNTs-3:1 as indicated by the histograms, consistent with the XRD results, suggesting that the increase of Pd(acac)$_2$ can directly result in an increased Pd particle size. For Pd/MWNTs-2:1, Figure 2.2(c), the tube wall surface is large-area covered by Pd NPs with a relatively sharp distribution, which probably accounts for the large electrochemically active surface area (*ECSA*). In contrast, an obvious agglomeration is observed for Pd/MWNTs-4:1 as indicated in Figure 2.2(d). Since the –COOH sites are constant on the tube wall surface, it is reasonable that they will be saturated by the growing
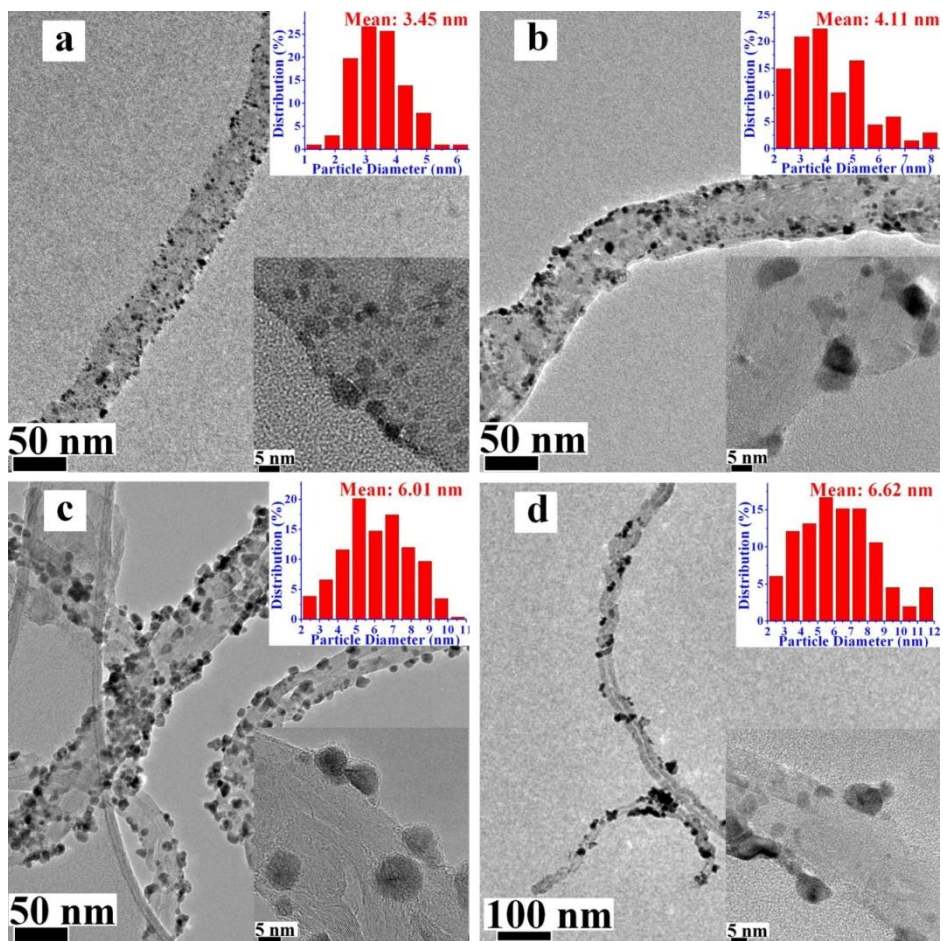
Figure 2.2. TEM microstructures of (a) Pd/MWNT-1:2, (b) Pd/MWNTs-1:1, (c) Pd/MWNTs-2:1, and (d) Pd/MWNTs-4:1. The insets of image (a-d) are particle-size histograms (top) and HRTEM images (bottom) of the corresponding nanocatalysts.

amount of Pd NPs and lead to the agglomeration and decreased deposition efficiency of Pd NPs.

2.3.3. TGA Analysis

Figure 2.3 shows the TGA curves of (a): as-received MWNTs-COOH, (b): Pd/MWNTs-1:2, (c): Pd/MWNTs-1:1, (d): Pd/MWNTs-2:1, (e): Pd/MWNTs-3:1 and (f): Pd/MWNTs-4:1 in air from 30 to 800 °C, inset is the enlarged picture in the range from 90 to 450 °C. All these Pd/MWNTs nanocatalysts exhibit similar thermal stability as subtle weight loss up to 200 °C due to the decomposition of remained acac on Pd surface,[58] slight weight up due to the oxidation of Pd from 250 to 400 °C, rapid weight loss due to the burning of MWNTs up to 650 °C and finally remain constant as PdO. In addition, it is clearly seen from the inset that the extents of the decomposition of remained acac and the following Pd oxidation of Pd NPs are consistent with the amount of Pd on the tube wall. The loading of Pd on MWNTs and corresponding conversion of Pd(acac)$_2$ are obtained from the TGA results and provided in Table 1. The loading of Pd increases from 13.12 to 43.67% with increasing the Pd(acac)$_2$ precursor amount from 0.05 to 0.4 g, indicating that the loading of Pd NPs on MWNTs can be directly increased by increasing the Pd(acac)$_2$ precursor amount. However, different varying trends of the conversion of Pd(acac)$_2$ is obtained in Table 2.1, i.e, relatively higher conversions of Pd(acac)$_2$ are achieved when the ratios of Pd(acac)$_2$ to MWNTs are as low as 1:2, 1:1, and 2:1 due to the comparatively more empty sites on the tube wall surface. However, further increase of precursor amount leads to an obvious decrease of Pd(acac)$_2$ conversion as indicated by Pd/MWNTs-3:1 (64.86%) and Pd/MWNTs-4:1 (54.89%). Since the number of defects is constant, it is reasonable that the carboxylic sites will become more and more saturated with the increased Pd NPs, thus causing an increasing hard

Table 2.1. The Pd loading and corresponding conversion of $Pd(acac)_2$ of different nanocatalysts.

Nanocatalysts	MWNTs (g)	$Pd(acac)_2$(g)	Pd loading (%)	$Pd(acac)_2$conversion (%)
Pd/MWNTs-1:2	0.1	0.05	13.12	85.61
Pd/MWNTs-1:1	0.1	0.1	19.64	75.25
Pd/MWNTs-2:1	0.1	0.2	33.57	76.21
Pd/MWNTs-3:1	0.1	0.3	40.74	64.86
Pd/MWNTs-4:1	0.1	0.4	43.67	54.89
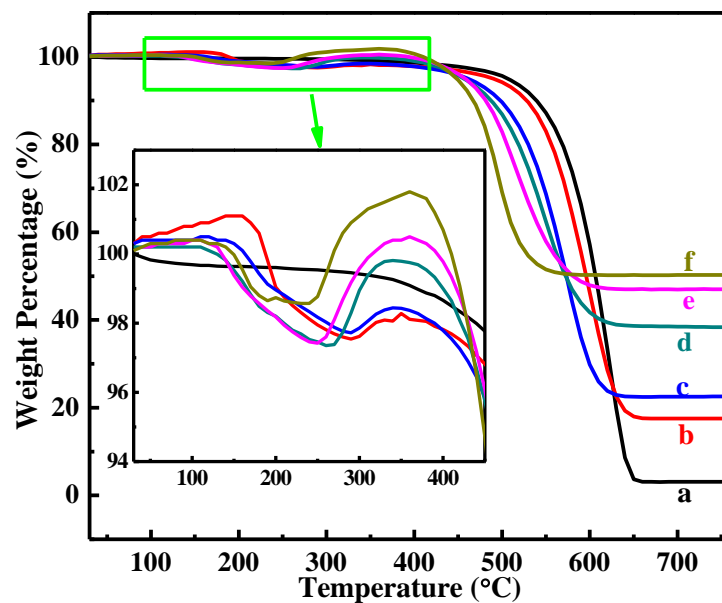
Figure 2.3. TGA curves of (a) as-received MWNTs-COOH, (b) Pd/MWNTs-1:2, (c) Pd/MWNTs-1:1, (d) Pd/MWNTs-2:1 (e) Pd/MWNTs-3:1 and (f) Pd/MWNTs-4:1. Inset is the enlarged part of the rectangle area.

deposition as confirmed by the TEM results. However, it is noticeable that the Pd/MWNTs-2:1 nanocatalyst achieves a considerable conversion as 76.21%.

2.3.4. Raman Spectroscopy

Raman spectroscopy, as a powerful technique to characterize the carbonaceous materials, could provide useful information in analyzing the surface structure and distinguishing the sp^2 and sp^3 hybridized forms of carbon. Figure 2.4(a-g) displays the Raman spectra of the as-received MWNTs-COOH, Pd/MWNTs-1:2, Pd/MWNTs-1:1, Pd/MWNTs-2:1, Pd/MWNTs-3:1, Pd/MWNTs-4:1 and bare Pd NPs. All the MWNTs-based samples are observed to exhibit characteristic D and G bands around ~ 1335 and 1580 cm^{-1}. The D band is a "dispersive" band that is ascribed to edges, other defects and disordered carbon,[59] whereas G band is related to the stretching mode of crystal graphite.[60] Due to the curvature of CNTs, in contrast to the perfect honeycomb lattice of graphite, the G band is splited into the G$^-$ and G$^+$ bands centered around 1576 and 1604 cm^{-1}, respectively.[61, 62] The intensity ratio of D and G bands (I_D/I_G) denoted as R is a measurement of the degree of disorder and the average size of the sp^2 domain,[63] the higher the R, the larger the degree of defects. It is clearly obtained that the R values of Pd/MWNTs-1:2 (1.420) and Pd/MWNTs-1:1 (1.395) are a little lower than that of the as-received MWNTs-COOH (1.520), which is probably due to the occupation of defects on MWNTs by the Pd NPs. However, a monotonous increase of R value is observed when further increasing the Pd loadings, i.e., Pd/MWNTs-2:1(1.738), Pd/MWNTs-3:1(1.853) and Pd/MWNTs-4:1(2.212), probably due to the incomplete decomposed acetylacetonate (acac) on the Pd surface. The bare Pd NPs also exhibit similar D and G band properties as indicated by bare Pd NPs, Figure 2.4(g). In addition, the increased particle size on the tube wall surface also causes more structural defects thus contributing to the increased R values.[64]
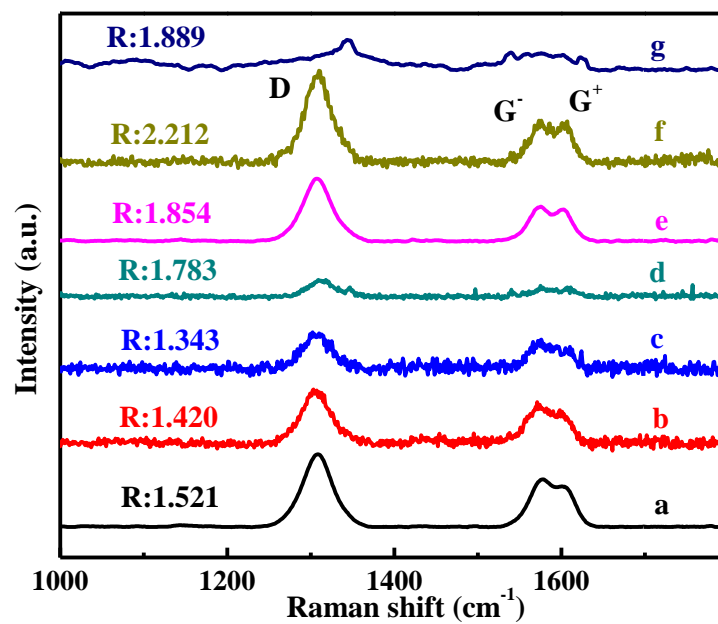
Figure 2.4. Raman spectra of (a) as-received MWNTs-COOH (b) Pd/MWNTs-1:2, (c) Pd/MWNTs-1:1, (d) Pd/MWNTs-2:1, (e) Pd/MWNTs-3:1, (f) Pd/MWNTs-4:1 and (g) bare Pd NPs.

2.3.5. XPS Characterization

In order to further identify the variations of atomic composition and carboxylic groups in the nanocatalysts with increasing the Pd loading, XPS is introduced to provide valuable insights into the surface of nanocatalysts. High resolution C 1s XPS spectra of the as-received MWNTs-COOH, Pd/MWNTs-1:2, Pd/MWNTs-1:1, Pd/MWNTs-2:1, Pd/MWNTs-3:1 and Pd/MWNTs-4:1 are shown in Figure 2.5(a-f). All the C 1s peaks can be smoothly deconvoluted into four fitting curves with peaks around 284.6, 286.6, 288.2 and 290.1 eV, which correspond to C-C, C-O, C=O, and O-C=O, respectively.[65] The unchanged presence of the four peaks in all the nanocatalysts clearly demonstrates that the synthesis process does not damage the structure of MWNTs, indicating the anchor role of carboxylic groups and the bonding interaction between Pd NPs and carboxylic groups. However, a monotonously decreased ratio of oxygen containing groups (COOH, C-O and C=O) to C-C group (the ratio denoted as S) is clearly observed due to the increased occupation of carboxylic groups with increasing the Pd loading. For nanocatalysts with low Pd loadings, i.e., Pd/MWNTs-1:2 and Pd/MWNTs-1:1, the S value is decreased dramatically from 0.66 to 0.35 and to 0.23 due to the evenly distributed small Pd NPs and resulted large defects occupation. However, the observed slight decreases of S values (0.18, 0.15 and 0.125) in Pd/MWNTs-2:1, Pd/MWNTs-3:1 and Pd/MWNTs-4:1 indicate a saturated occupation of defects, which is also consistent with the XRD results. The XPS spectra of the Pd 3d levels of all the nanocatalysts are also curve-fitted and shown in the inset of Figure 2.4, all the Pd 3d curves can be fitted with two spin-orbit split doublets corresponding to Pd $3d_{3/2}$ and Pd $3d_{5/2}$ components, which can be further fitted into four peaks corresponding to Pd(0)$3d_{5/2}$, Pd(0)$3d_{3/2}$, Pd(II)$3d_{5/2}$ and Pd(II)$3d_{3/2}$, respectively,[66] indicating the similar containments of Pd and Pd^{2+} in each nanocatalyst.

Figure 2.5. High resolution C 1s XPS spectrums of (a) as-received MWNTs-COOH, (b) Pd/MWNTs-1:2, (c) Pd/MWNTs-1:1, (d) Pd/MWNTs-2:1, (e) Pd/MWNTs-3:1 and (f) Pd/MWNTs-4:1.
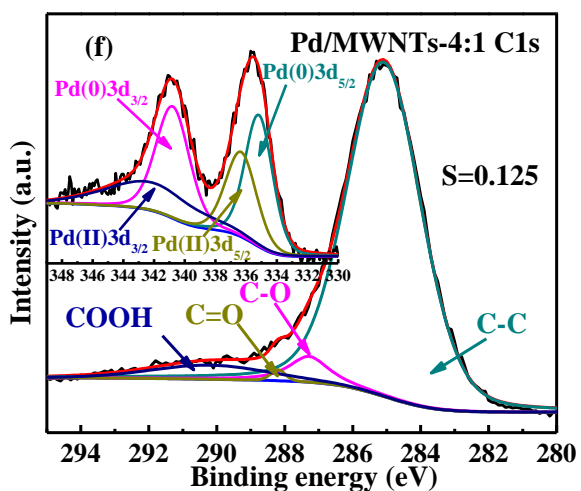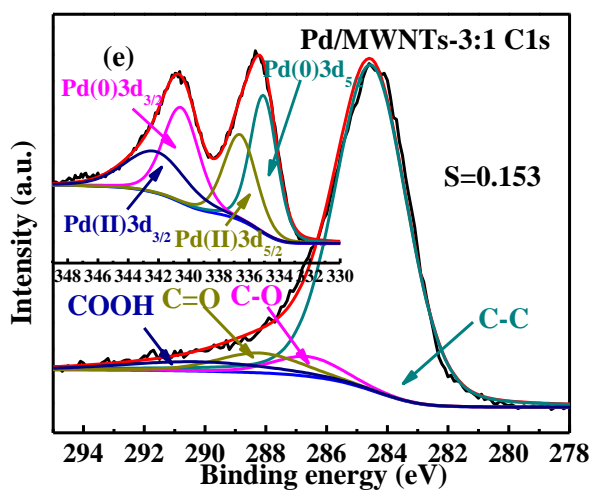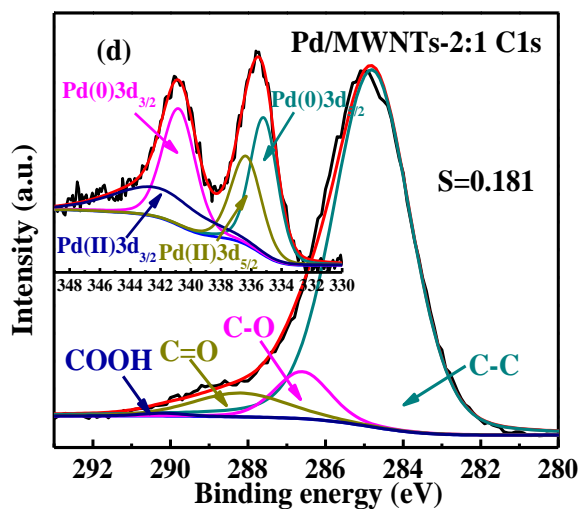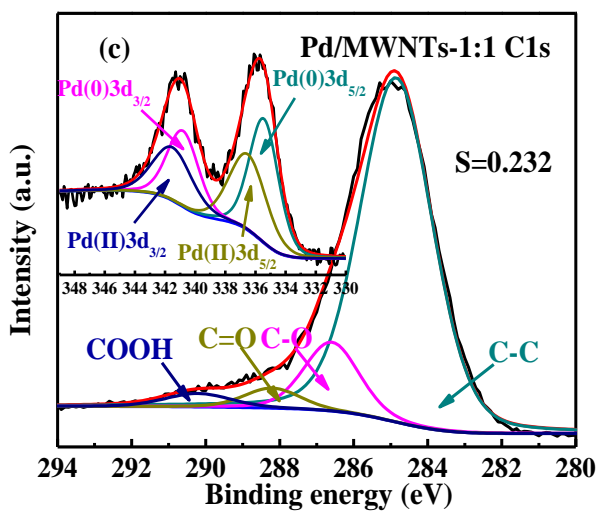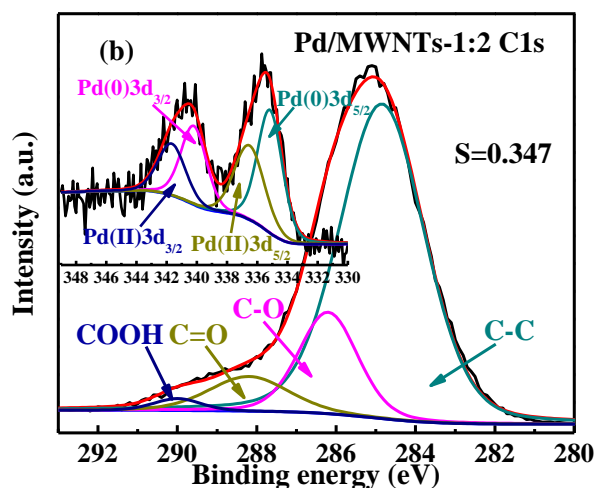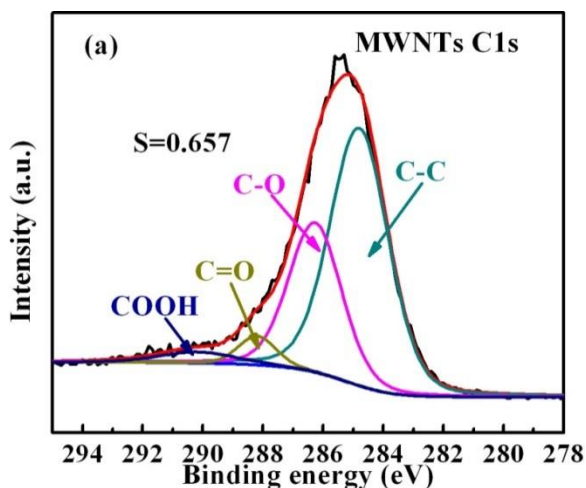
2.3.6. Electrocatalytic Activity toward EOR

Electrochemical Active Surface Area *(ECSA)* is an important index to provide information about the active sites in catalyst and to assess the conductive pathways available to transfer electrons from and to the catalyst surface.[67] *ECSA*, usually obtained from CV technique, is also an important technique to investigate the electro-catalytic activity. Figure 2.6(A&C) represents the CVs of a: Pd/MWNTs-1:2, b: Pd/MWNTs-1:1, c: Pd/MWNTs-2:1, d: Pd/MWNTs-3:1 and e: Pd/MWNTs-4:1 in 1.0 M KOH solution with current density normalized to catalyst mass and Pd mass, respectively. The typical peaks are well defined for all the nanocatalysts as peak I: hydrogen oxidation peak, peak II: oxidative desorption of H and adsorption of OH⁻, peak III: oxidation of Pd, peak IV: reduction of PdO, and Peak V: reductive adsorption/absorption of H.[68, 69] Integrating peak IV is usually used to estimate the *ECSA* value based on the columbic charge for the reduction of PdO using Equation (2).[70]

$$ECSA = Q / SL \qquad (2)$$

where "Q" is the charge associated with PdO stripping, "S" is the proportionality coefficient as 405 μC cm^{-2} that is used to relate charges with area under an assumption that a monolayer of PdO is covered on the surface, 'L' is the Pd loading in 'g', the estimated *ESCA* values are calculated from Figure 2.6(C) and shown in Table 2.2. The *ESCA* value is monotonously decreased with increasing the Pd loading. The highest value as 104.21 m^2/ g $_{Pd}$ is observed for Pd/MWNTs-1:2 probably due to the ultrafine particles with uniform distribution. However, with increasing the Pd amount on the tube wall surface, the Pd NPs continue growing with slight aggregation, thus limiting the usage of Pd NPs and causing a decreased *ECSA*. Finally, it is clearly observed that the *ECSA* values keep almost the same for Pd/MWNTs-3:1(48.89 m^2/g $_{Pd}$) and Pd/MWNTs-4:1(49.88 m^2/g $_{Pd}$) due to the limited defects, which decrease the utilization of Pd metal.
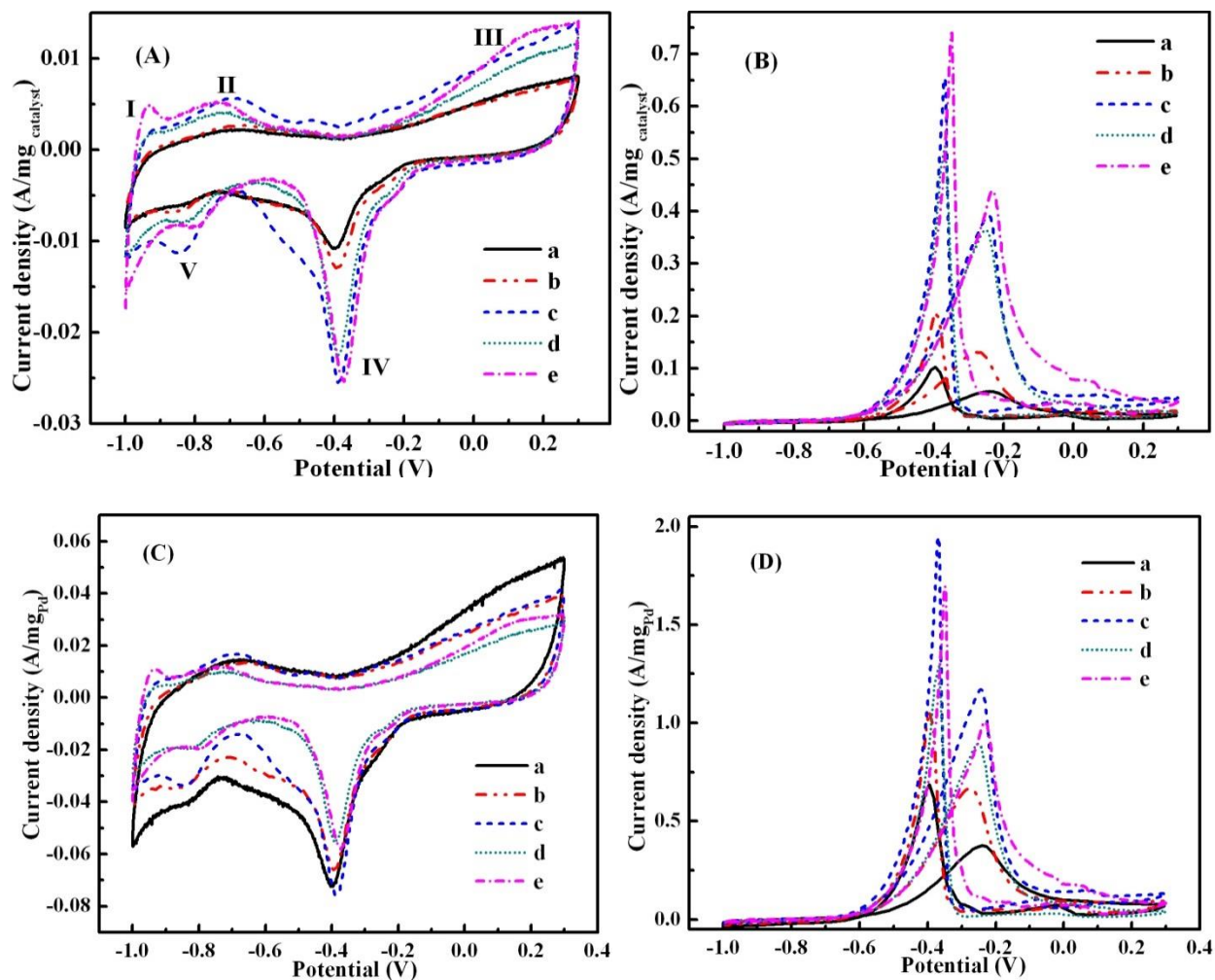
Figure 2.6. CVs of (a): Pd/MWNTs-1:2, (b): Pd/MWNTs-1:1, (c): Pd/MWNTs-2:1, (d): Pd/MWNTs-3:1 and (e): Pd/MWNTs-4:1 in (A): 1.0 M KOH solution, (B): 1.0 M KOH solution containing 1.0 M ethanol at 50 mV/s with current density normalized to catalyst mass, (C&D) are corresponding CVs with current density normalized to Pd mass.

Figure 2.6(B&D) represents the CVs in 1.0 M KOH containing 1.0 M ethanol solution with current density normalized to catalyst mass and Pd mass, respectively. Two characteristic peaks as anodic and cathodic peaks are all clearly observed, indicating that all the nanocatalysts exhibit catalytic-activity toward EOR. The anodic peaks centered around -0.25 V is a typical parameter to assess the electro-catalytic activity towards EOR. For the cathodic peaks starting at -0.4 V, some authors assigned the cathodic peaks to the removal of carbonaceous species that are not completely oxidized in the anodic scan.[71, 72] However, the intermediates generated in the forward scan probably diffuse into the bulk electrolyte and are fully oxidized at high potentials. In addition, the sharp increase also indicates that the peak is probably due to the oxidation of fresh ethanol immediately after the reduction of PdO.[73] The current peak density (j_p) values normalized to catalyst mass and Pd mass obtained from Figure 2.6(B&D) are shown in Table 2.2. For j_p normalized to catalyst mass, Pd/MWNTs-2:1, Pd/MWNTs-3:1, and Pd/MWNTs-4:1 are almost the same and larger than those of Pd/MWNTs-1:2 and Pd/MWNTs-1:1. The deficiency of active Pd sites in Pd/MWNTs-2:1 and Pd/MWNTs-1:1 mainly accounts for the poor catalytic activity. The catalytic activities are largely enhanced due to the increased active Pd sites as indicated by Pd/MWNTs-2:1, Pd/MWNTs-3:1 and Pd/MWNTs-4:1. However, as the deposition of Pd NPs becomes increasingly hard after the carboxylic sites are saturated, the catalytic properties are almost constant due to the roughly same Pd loading and unchanged *ECSA* value.

After normalizing the current peak density to Pd mass, the current densities of the anodic peaks are re-determined and provided in Table 2.2. The j_p value follows the order as Pd/MWNTs-2:1 > Pd/MWNTs-4:1 > Pd/MWNTs-3:1 > Pd/MWNTs-1:1 > Pd/MWNTs-1:2, revealing that Pd/MWNTs-2:1 exhibits the highest specific Pd catalytic activity, which makes it the best one with the consideration of the efficient precursor conversion. Finally, as the agglomeration of Pd NPs is

Table 2.2. Comparing CV results for different nanocatalysts.

Nanocatalysts	$ECSA$ (m^2/g $_{Pd}$)	j_p (A/$_{mg\ catalyst}$)	j_p(A/$_{mg\ Pd}$)
Pd/MWNTs-1:2	104.21	0.0591	0.3753
Pd/MWNTs-1:1	87.41	0.1311	0.6634
Pd/MWNTs-2:1	83.20	0.3895	1.1693
Pd/MWNTs-3:1	48.89	0.3648	0.8963
Pd/MWNTs-4:1	49.88	0.4379	1.0105

observed in the high Pd loading nanocatalysts, it is reasonable that the Pd specific activity is expected to decline due to the insufficient utilized Pd NPs as indicated by Pd/MWNTs-4:1.

In order to further probe the tolerance of these nanocatalysts toward CO poisoning species, chronoamperometric (CA) measurements were performed in 1.0 M KOH containing 1.0 M ethanol solution for a duration of 1000 s. Figure 2.7(A&B) shows the CA curves at -0.3 V with current density normalized to the catalyst mass and Pd mass, respectively, a: Pd/MWNTs-1:2, b: Pd/MWNTs-1:1, c: Pd/MWNTs-2:1, d: Pd/MWNTs-3:1 and e: Pd/MWNTs-4:1. All these CA curves exhibit similar results. All the polarization currents decay rapidly during the initial period and a pseudosteady state is achieved gradually. The decrease in current is caused by the Pd surface poisoning induced by the CO_{ads} species. Among all the nanocatalysts in this study, Pd/MWNTs-2:1 exhibits the lowest decay speed and is able to maintain the highest stable current due to the enough active Pd sites and the evenly particle distribution on the tube wall surface. The nanocatalysts with low loadings such as Pd/MWNTs-1:2 and Pd/MWNTs-1:1 exhibit poor stability due to the shortage of active Pd sites. However, after the deposition of Pd is saturated on the tube wall surface, no obvious tolerance stability improvement is observed for Pd/MWNTs-1:3 and Pd/MWNTs-1:4. In addition, a faster degradation is observed in Pd/MWNTs-1:4 than in Pd/MWNTs-2:1 after the normalization to Pd mass. It is demonstrated previously that Pd NPs are inclined to aggregate after the CA test.[74] Therefore, the clear agglomeration of Pd NPs observed in the TEM image of Pd/MWNTs-4:1 probably deteriorated the tolerance stability in CA tests due to the decreased active sites in the aggregated big NPs. Finally, it is worth mentioning that Pd/MWNTs-2:1 maintains the highest tolerance stability among all the nanocatalysts.

Electrochemical impedance spectroscopy (EIS) as a sensitive electrochemical technique can provide information about the impedance characteristics of the electro oxidation toward EOR.[75, 76]
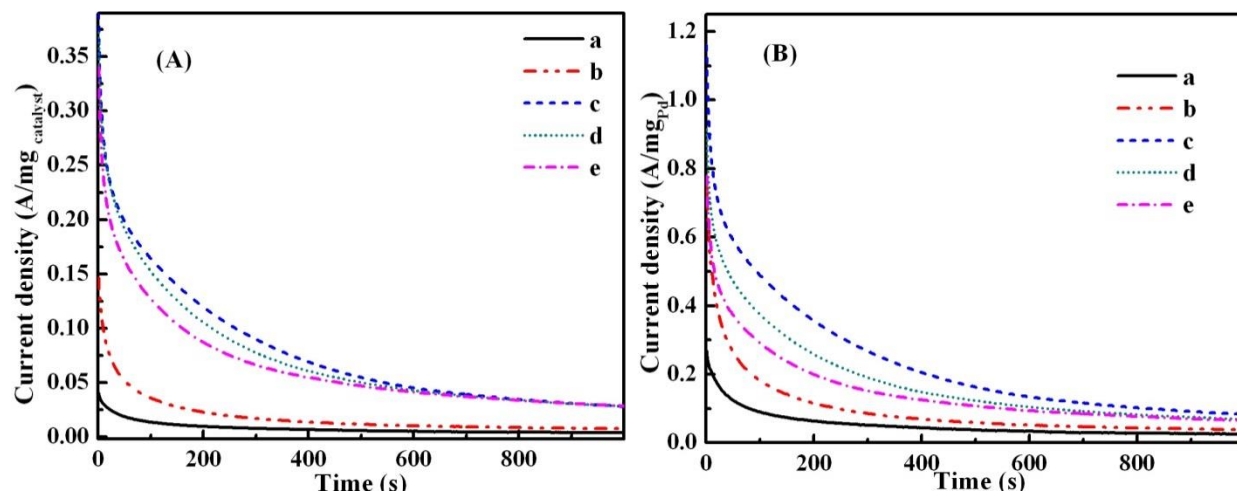
Figure 2.7. CA curves of (a): Pd/MWNTs-1:2, (b): Pd/MWNTs-1:1, (c): Pd/MWNTs-2:1, (d): Pd/MWNTs-3:1 and (e): Pd/MWNTs-4:1 in 1.0 M KOH containing 1.0 M ethanol solution for a duration of 1000 s at -0.3 V, (A) with current density normalized to catalyst mass, (B) with current density normalized to Pd mass.

Figure 2.8 presents the semicircular Nyquist plots of imaginary (Z"Ω) versus real (Z'Ω) components of impedance in 1.0 M KOH solution containing 1.0 M ethanol on these five nanocatalysts. The illustrations are shown in the lower potential region at -0.4 V with respect to SCE. The appearance of semicircular plots indicates kinetically controlled EOR reactions. The diameter of the primary semicircle is always used to measure the charge transfer resistance of the catalyst, which evaluates how fast the charge transfer during the oxidation process.[77] Therefore, a decreased diameter of the semicircular Nyquist plot means a decrease in the charge transfer resistance (R_{ct}) and an enhancement of charge transfer reaction kinetics. The R_{ct} values of the nanocatalysts are estimated by fitting the EIS curves using the software ZsimpWin based on an equivalent electric circuit as shown inset of Figure 2.8.[78] In this $R_s(R_{ct} CPE)$ circuit, R_s represents the uncompensated solution resistance, R_{ct} represents the charge-transfer resistance while the constant phase element (CPE) is related to a capacitor property, The parallel combination of the R_{ct} and CPE takes into account the thin electrode film as well as ethanol adsorption and oxidation. The values for all the parameters R_s, R_{ct}, CPE and their associated % error are summarized in Table 2.3. The R_s values are observed to be almost the same due to the same solution resistance, however, the R_{ct} of Pd/MWNTs-1:2 and Pd/MWNTs-1:1 decreases from 4149 to 1125 Ω due to the increased active Pd sites. In addition, the R_{ct} values of Pd/MWNTs-2:1, Pd/MWNTs-3:1, and Pd/MWNTs-4:1 are found to be almost the same and several times smaller than those of Pd/MWNTs-1:2 and Pd/MWNTs-1:1, suggesting that the electro-catalytic activities of Pd/MWNTs-2:1, Pd/MWNTs-3:1, and Pd/MWNTs-4:1 are largely enhanced with increasing the Pd loading, however, the loading are constant with further increasing the Pd(acac)$_2$ amount due to the saturation of the tube wall surface by Pd NPs.
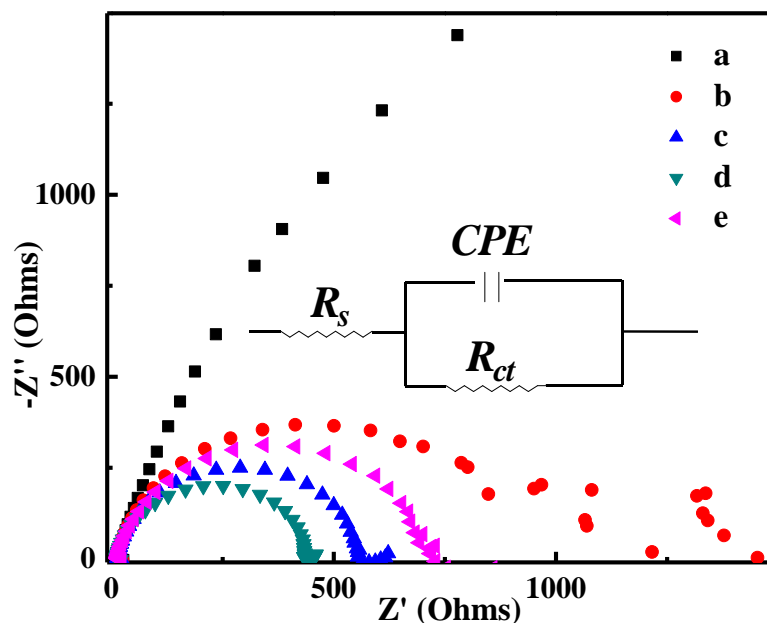
Figure 2.8. EIS spectra of (a): Pd/MWNTs-1:2, (b): Pd/MWNTs-1:1, (c): Pd/MWNTs-2:1, (d): Pd/MWNTs-3:1 and (e): Pd/MWNTs-4:1 in 1.0 M KOH containing 1.0 M ethanol at -0.4 V vs. SCE, inset is the equivalent circuit used to fit the impedance spectra.

Table 2.3. Impedance components for different electrodes by fitting the experimental data using Zsimp-Win software based on the equivalent circuit presented inset of Figure 2.8.

Electrode	R_s/Ω		R_{ct}/Ω		CPE	
	value	error%	value	error%	value	error%
Pd/MWNTs-1:2	17.37	5.248	4149	11.17	1.437E-5	5.141
Pd/MWNTs-1:1	15.18	4.503	1125	4.836	1.625E-5	4.982
Pd/MWNTs-2:1	15.39	2.556	540.9	2.817	2.538E-5	3.283
Pd/MWNTs-3:1	13.29	2.667	422.3	2.776	2.264E-7	3.4
Pd/MWNTs-4:1	14.93	2.966	693.6	3.171	1.994E-5	3.56

2.3.7. Kinetics Study

Slow linear sweep voltammetry (LSV) measurements for Pd/MWNTs-1:2, Pd/MWNTs-1:1, Pd/MWNTs-2:1 and Pd/MWNTs-4:1 were conducted in 1.0 M KOH solution containing 1.0 M ethanol at a scan rate of 50 mV/s at room temperature. For all the LSV curves, Figure 2.9(A), they can be divided into two regions. In the low potential region, the current densities are increased very slowly with increasing the polarization potential and all the four curves are almost overlapped. The adsorption of hydrogen and water in this region partially inhibits the ethanol adsorption, thus resulting in a slow current increase. However, in the relatively higher potential region, the polarization current is increased sharply with increasing the polarization potential and the j_p values of different nanocatalysts are increased with increasing the Pd loading. For Pd/MWNTs-2:1 and Pd/MWNTs-4:1 nanocatalysts, the j_p values are almost the same, consistent with the CV result. A limiting current is achieved at about -0.28 V, which is probably attributed to the blocking of active catalytic sites by the adsorbed CO_{ads} species.[68] Furthermore, the onset-potential of EOR starts at more negative on Pd/MWNTs-2:1 and Pd/MWNTs-4:1 than the low loading nanocatalysts such as Pd/MWNTs-1:2 and Pd/MWNTs-1:1, implying an easier oxidation of ethanol on high Pd loading nanocatalysts. Figure 2.9(B) displays the corresponding Tafel polarization plots for the EOR on the four nanocatalysts. Each plot can be fitted and divided into three linear regions (I, II, and III) according to the change of Tafel slops. The first fitted Tafel slopes appear in low potential range (< -0.45 V), the kinetics of the EOR in this potential region is probably dominated by the adsorption of hydroxyl on the Pd electrode.[79, 80] The second slopes are in the high potential range (-0.45 to -0.30 V), the Tafel slopes increase to higher ones, indicating a possible change of reaction mechanism or at least a transformation of rate-determining step as the kinetics control of the EOR is shifted from hydroxyl adsorption to oxide layer formation. [68, 81] The negative slopes observed in the range from -0.2 to 0.25 V are for the third slope. From the aspect of comparing reaction
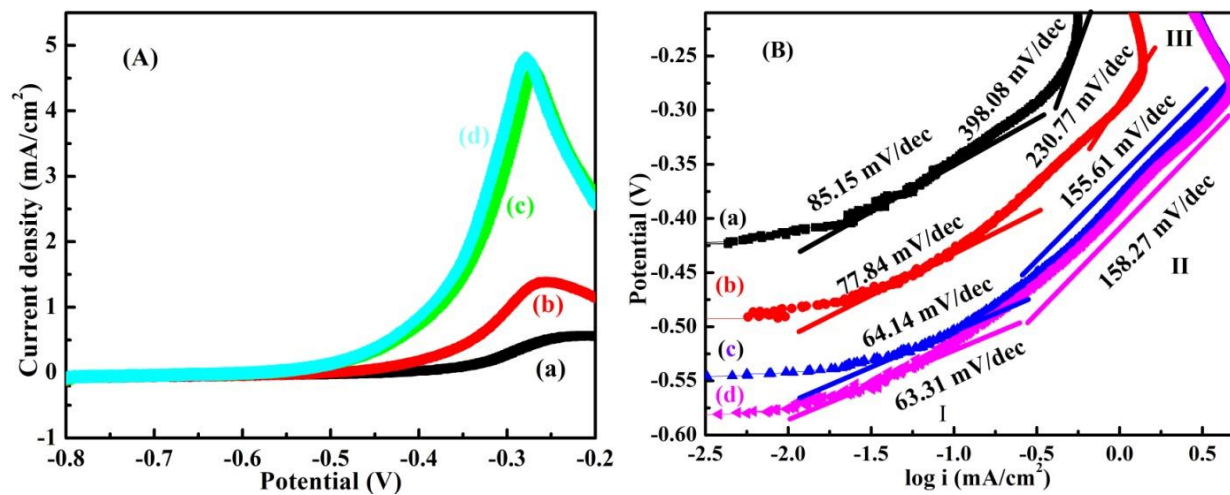
Figure 2.9. (A) Steady-state polarization plots and (B) corresponding Tafel plots for EOR on a: Pd/MWNTs-1:2, b: Pd/MWNTs-1:1,c: Pd/MWNTs-2:1 and d: Pd/MWNTs-4:1.

kinetics, it is clearly seen from Figure 2.9(B) that the slopes in region I&II decrease monotonously with increasing the Pd loadings, suggesting that the reaction kinetics are largely enhanced due to the increase of active Pd sites. However, the slopes of Pd/MWNTs-2:1 and Pd/MWNTs-4:1 are almost the same due to the saturation of MWNTs, indicating that the optimal reaction kinetics are achieved in relatively higher Pd loading catalysts.

2.4. Conclusions

In this work, Pd/MWNTs catalysts with different Pd loadings have been prepared by simply thermal decomposing different amounts of $Pd(acac)_2$ in the presence of amount-fixed MWNTs-COOH in a refluxing xylene solution. Increased Pd NPs size with increasing the $Pd(acac)_2$ precursor amount was clearly characterized by XRD and TEM. A clear agglomeration was observed in high Pd loading nanocatalysts due to the saturation of defects on the tube wall surface with an initial precursor ratio of $Pd(acac)_2$ to MWNTs-COOH as 4:1. The utilization status of the carboxylic groups was investigated by Raman spectroscopy and XPS spectra as the occupation of defects became more and more serious with increasing the Pd loading. The Pd loadings and corresponding conversions of $Pd(acac)_2$ were calculated from TGA results. Increased Pd loadings with decreased precursor conversions were observed with increasing the $Pd(acac)_2$ amount. The electrochemical performance toward EOR demonstrated that the precursor ratio as $Pd(acac)_2$ to MWNTs-COOH of 2:1 exhibited the highest specific Pd activity and tolerance stability. EIS, LSV and corresponding Tafel characterizations showed greatly declined charge transfer resistances and enhanced reaction kinetics with increasing the Pd loading. Combined investigations of the precursor conversion and catalytic activity imply that Pd/MWNTs-2:1 gave the best catalytic performance with economic consideration.

2.5. References

1. J. H. Byeon and Y.-W. Kim, *ACS Applied Materials & Interfaces*, 2011, **3**, 2912-2918.
2. C. K. Dyer, *Journal of Power Sources*, 2002, **106**, 31-34.
3. S. K. Kamarudin, F. Achmad and W. R. W. Daud, *International Journal of Hydrogen Energy*, 2009, **34**, 6902-6916.
4. M. M. O. Thotiyl, T. R. Kumar and S. Sampath, *The Journal of Physical Chemistry C*, 2010, **114**, 17934-17941.
5. C. W. Xu, H. Wang, P. K. Shen and S. P. Jiang, *Advanced Materials*, 2007, **19**, 4256-4259.
6. D. Y. Zhang, Z. F. Ma, G. Wang, K. Konstantinov, X. Yuan and H. K. Liu, *Electrochemical and solid-state letters*, 2006, **9**, A423-A426.
7. C. Y. Wang, *Chemical Reviews*, 2004, **104**, 4727-4766.
8. Y. Paik, S. S. Kim and O. H. Han, *Angewandte Chemie International Edition*, 2008, **47**, 94-96.
9. S. Song, W. Zhou, Z. Liang, R. Cai, G. Sun, Q. Xin, V. Stergiopoulos and P. Tsiakaras, *Applied Catalysis B: Environmental*, 2005, **55**, 65-72.
10. Z. J. Mellinger, T. G. Kelly and J. G. Chen, *ACS Catalysis*, 2012, **2**, 751-758.
11. F. Hu, X. Cui and W. Chen, *The Journal of Physical Chemistry C*, 2010, **114**, 20284-20289.
12. C. Xu, L. Cheng, P. Shen and Y. Liu, *Electrochemistry Communications*, 2007, **9**, 997-1001.
13. T. Teranishi and M. Miyake, *Chemistry of Materials*, 1998, **10**, 594-600.
14. M. T. Reetz, M. Winter and B. Tesche, *Chemical Communications*, 1997, DOI: 10.1039/A606490F, 147-148.
15. E. E. Drinkel, R. R. Campedelli, A. M. Manfredi, H. D. Fiedler and F. Nome, *The Journal of Organic Chemistry*, 2014, **79**, 2574-2579.
16. V. Mazumder and S. Sun, *Journal of the American Chemical Society*, 2009, **131**, 4588-4589.
17. M. Gurrath, T. Kuretzky, H. P. Boehm, L. B. Okhlopkova, A. S. Lisitsyn and V. A. Likholobov, *Carbon*, 2000, **38**, 1241-1255.
18. N. M. Kinnunen, M. Suvanto, M. A. Moreno, A. Savimäki, K. Kallinen, T. J. J. Kinnunen and T. A. Pakkanen, *Applied Catalysis A: General*, 2009, **370**, 78-87.
19. G. Hu, F. Nitze, H. R. Barzegar, T. Sharifi, A. Mikołajczuk, C.-W. Tai, A. Borodzinski and T. Wågberg, *Journal of Power Sources*, 2012, **209**, 236-242.
20. L.-S. Zhong, J.-S. Hu, Z.-M. Cui, L.-J. Wan and W.-G. Song, *Chemistry of Materials*, 2007, **19**, 4557-4562.
21. K. Mori, K. Yamaguchi, T. Hara, T. Mizugaki, K. Ebitani and K. Kaneda, *Journal of the American Chemical Society*, 2002, **124**, 11572-11573.
22. K. Ding, H. Jia, S. Wei and Z. Guo, *Industrial & Engineering Chemistry Research*, 2011, **50**, 7077-7082.
23. G. G. Wildgoose, C. E. Banks and R. G. Compton, *Small*, 2006, **2**, 182-193.
24. B. Yoon and C. M. Wai, *Journal of the American Chemical Society*, 2005, **127**, 17174-17175.
25. S. Y. Lee, M. Yamada and M. Miyake, *Carbon*, 2005, **43**, 2654-2663.
26. V. Georgakilas, D. Gournis, V. Tzitzios, L. Pasquato, D. M. Guldi and M. Prato, *Journal of Materials Chemistry*, 2007, **17**, 2679-2694.
27. L. Jiang and L. Gao, *Carbon*, 2003, **41**, 2923-2929.

28. B. Wu, Y. Kuang, X. Zhang and J. Chen, *Nano Today*, 2011, **6**, 75-90.
29. F. Wang, C. Li, L. D. Sun, C. H. Xu, J. Wang, J. C. Yu and C. H. Yan, *Angewandte Chemie International Edition*, 2012, **51**, 4872-4876.
30. G. R. Zhang, J. Wu and B.-Q. Xu, *The Journal of Physical Chemistry C*, 2012, **116**, 20839-20847.
31. J. Kong, M. G. Chapline and H. Dai, *Advanced Materials*, 2001, **13**, 1384-1386.
32. D. Bera, S. C. Kuiry, M. McCutchen, S. Seal, H. Heinrich and G. C. Slane, *Journal of applied physics*, 2004, **96**, 5152-5157.
33. D.-d. Zhou, L. Ding, H. Cui, H. An, J.-p. Zhai and Q. Li, *Chemical Engineering Journal*, 2012, **200**, 32-38.
34. X. R. Ye, Y. Lin and C. M. Wai, *Chemical Communications*, 2003, DOI: 10.1039/B211350C, 642-643.
35. X. R. Ye, Y. Lin, C. Wang, M. H. Engelhard, Y. Wang and C. M. Wai, *Journal of Materials Chemistry*, 2004, **14**, 908-913.
36. Y. Lin, X. Cui, C. Yen and C. M. Wai, *The Journal of Physical Chemistry B*, 2005, **109**, 14410-14415.
37. J. P. Tessonnier, L. Pesant, G. Ehret, M. J. Ledoux and C. Pham-Huu, *Applied Catalysis A: General*, 2005, **288**, 203-210.
38. S.-u. Rather, R. Zacharia, S. W. Hwang and K. S. Nahm, *Chemical physics letters*, 2007, **441**, 261-267.
39. K. P. de Jong, *Current Opinion in Solid State and Materials Science*, 1999, **4**, 55-62.
40. F. Yang, Y. Li, T. Liu, K. Xu, L. Zhang, C. Xu and J. Gao, *Chemical Engineering Journal*, 2013, **226**, 52-58.
41. X. Ji, C. E. Banks, A. F. Holloway, K. Jurkschat, C. A. Thorogood, G. G. Wildgoose and R. G. Compton, *Electroanalysis*, 2006, **18**, 2481-2485.
42. U. Schlecht, K. Balasubramanian, M. Burghard and K. Kern, *Applied surface science*, 2007, **253**, 8394-8397.
43. S. Mubeen, T. Zhang, B. Yoo, M. A. Deshusses and N. V. Myung, *The Journal of Physical Chemistry C*, 2007, **111**, 6321-6327.
44. A. D. Franklin, J. T. Smith, T. Sands, T. S. Fisher, K.-S. Choi and D. B. Janes, *The Journal of Physical Chemistry C*, 2007, **111**, 13756-13762.
45. T. M. Day, P. R. Unwin and J. V. Macpherson, *Nano Letters*, 2007, **7**, 51-57.
46. D. J. Guo and H. L. Li, *Electrochemistry Communications*, 2004, **6**, 999-1003.
47. H. C. Choi, M. Shim, S. Bangsaruntip and H. Dai, *Journal of the American Chemical Society*, 2002, **124**, 9058-9059.
48. W. Chen, J. Zhao, J. Y. Lee and Z. Liu, *Materials Chemistry and Physics*, 2005, **91**, 124-129.
49. L. Chen, K. Yang, H. Liu and X. Wang, *Carbon*, 2008, **46**, 2137-2139.
50. X. Chen, Y. Hou, H. Wang, Y. Cao and J. He, *The Journal of Physical Chemistry C*, 2008, **112**, 8172-8176.
51. M. Zhang, Z. Yan and J. Xie, *Electrochimica Acta*, 2012, **77**, 237-243.
52. L. Miao, V. R. Bhethanabotla, M. M. Ossowski and B. Joseph, *The Journal of Physical Chemistry B*, 2006, **110**, 22415-22425.
53. D. Morales Acosta, M. D. Morales Acosta, L. A. Godinez, L. Álvarez Contreras, S. M. Duron Torres, J. Ledesma García and L. G. Arriaga, *Journal of Power Sources*, 2011, **196**, 9270-9275.

54. F. Zhu, G. Ma, Z. Bai, R. Hang, B. Tang, Z. Zhang and X. Wang, *Journal of Power Sources*, 2013, **242**, 610-620.
55. G. A. Camara and T. Iwasita, *Journal of Electroanalytical Chemistry*, 2005, **578**, 315-321.
56. Z. Liang, T. Zhao, J. Xu and L. Zhu, *Electrochimica Acta*, 2009, **54**, 2203-2208.
57. A. Kashyout, A. B. A. Nassr, L. Giorgi, T. Maiyalagan and B. A. Youssef, *Int. J. Electrochem. Sci*, 2011, **6**, 379-393.
58. B. Pal and M. Sharon, *Thin Solid Films*, 2000, **379**, 83-88.
59. C. Furtado, U. Kim, H. Gutierrez, L. Pan, E. Dickey and P. C. Eklund, *Journal of the American Chemical Society*, 2004, **126**, 6095-6105.
60. U. J. Kim, C. A. Furtado, X. Liu, G. Chen and P. C. Eklund, *Journal of the American Chemical Society*, 2005, **127**, 15437-15445.
61. H. Telg, M. Fouquet, J. Maultzsch, Y. Wu, B. Chandra, J. Hone, T. F. Heinz and C. Thomsen, *physica status solidi (b)*, 2008, **245**, 2189-2192.
62. S. Piscanec, M. Lazzeri, J. Robertson, A. C. Ferrari and F. Mauri, *Physical Review B*, 2007, **75**, 035427.
63. R. N. Singh and R. Awasthi, *Catalysis Science & Technology*, 2011, **1**, 778-783.
64. Z. Guo, H. Qu, Y. Wang, Q. He, X. Zhang, G.-L. Zhao, H. A. Colorado, J. Yu, L. Sun, S. Bhana, X. Huang, D. P. Young, H. Wang, X. Wang, J. Guo, M. A. Khan, S. Wei and J. Zhu, *Journal of Materials Chemistry C*, 2014, DOI: 10.1039/C4TC01351D.
65. Y. Li, W. Zhou, H. Wang, L. Xie, Y. Liang, F. Wei, J.-C. Idrobo, S. J. Pennycook and H. Dai, *Nat Nano*, 2012, **7**, 394-400.
66. T. Pillo, R. Zimmermann, P. Steiner and S. Hüfner, *Journal of Physics: Condensed Matter*, 1997, **9**, 3987.
67. H. Huang and X. Wang, *Journal of Materials Chemistry*, 2012, **22**, 22533-22541.
68. Z. X. Liang, T. S. Zhao, J. B. Xu and L. D. Zhu, *Electrochimica Acta*, 2009, **54**, 2203-2208.
69. R. Awasthi and R. N. Singh, *Catalysis Science & Technology*, 2012, **2**, 2428-2432.
70. Z. S. Yang and J. J. Wu, *Fuel Cells*, 2012, **12**, 420-425.
71. F. P. Hu, Z. Wang, Y. Li, C. Li, X. Zhang and P. K. Shen, *Journal of Power Sources*, 2008, **177**, 61-66.
72. Y. H. Qin, H. H. Yang, X. S. Zhang, P. Li, X. G. Zhou, L. Niu and W. K. Yuan, *Carbon*, 2010, **48**, 3323-3329.
73. Z. Zhang, L. Xin, K. Sun and W. Li, *International Journal of Hydrogen Energy*, 2011, **36**, 12686-12697.
74. Y. W. Lee, S. B. Han and K. W. Park, *Electrochemistry Communications*, 2009, **11**, 1968-1971.
75. Q. He, W. Chen, S. Mukerjee, S. Chen and F. Laufek, *Journal of Power Sources*, 2009, **187**, 298-304.
76. Y. Bai, J. Wu, J. Xi, J. Wang, W. Zhu, L. Chen and X. Qiu, *Electrochemistry Communications*, 2005, **7**, 1087-1090.
77. J. J. Wang, G. P. Yin, J. Zhang, Z. B. Wang and Y. Z. Gao, *Electrochimica Acta*, 2007, **52**, 7042-7050.
78. Y. Lin, X. Cui, C. H. Yen and C. M. Wai, *Langmuir*, 2005, **21**, 11474-11479.
79. L. Jiang, A. Hsu, D. Chu and R. Chen, *International Journal of Hydrogen Energy*, 2010, **35**, 365-372.
80. S. Y. Shen, T. S. Zhao and J. B. Xu, *Electrochimica Acta*, 2010, **55**, 9179-9184.

81.   F. Miao, B. Tao and P. K. Chu, *Dalton Transactions*, 2012, **41**, 5055-5059.

Chapter 3 Ultrafine FePd Nanoalloys Decorated Multiwalled Cabon

Nanotubes toward Enhanced Ethanol Oxidation Reaction

This chapter is revised based on a paper first authored by myself.

Y. Wang, Q. He, J. Guo, J. Wang, Z. Luo, T. D. Shen, K. Ding, A. Khasanov, S. Wei and Z. Guo, Ultrafine FePd Nanoalloys Decorated Multiwalled Cabon Nanotubes toward Enhanced Ethanol Oxidation Reaction, *ACS Applied Materials & Interfaces*, 7(43), 23920-23931(2015)

My priority contribution to this paper include (i) development of the problem into a work, (ii) identification of the study area and objectives, (iii) design and conducting of the experiment, (iv) gathering and rendering literature, (v) processing and analysis the experimental data, (vi) pulling various contributions into a single paper. (vii) writing the paper.

Abstract

Ultrafine palladium iron (FePd) nanoalloys deposited on gamma γ-Fe_2O_3, FePd-Fe_2O_3, further anchored on carboxylic group functionalized multi-walled carbon nanotubes (MWNTs-COOH), FePd-Fe_2O_3/MWNTs, were successfully synthesized by a facile one-pot solution based method as thermal decomposing palladium acetylacetonate ($Pd(acac)_2$) and iron pentacarbonyl ($Fe(CO)_5$) in a refluxing dimethylformamide solution in the presence of MWNTs-COOH. A 3.65 fold increase of peak current density was observed in cyclic voltammetry (CV) for ethanol oxidation reaction (EOR) compared with that of Pd/MWNTs after normalizing to Pd mass. The greatly enhanced tolerance stability towards poisoning species and largely reduced charge resistances were also obtained in chronoamperometry (CA) and electrochemical impedance spectroscopy (EIS) due to the downward shifted d band center of FePd alloy, easily formed oxygen containing species on Fe_2O_3, stabilizing role of the MWNTs and the optimized ratio of Fe_2O_3 to MWNTs-COOH.

3.1. Introduction

Pd-based catalysts have attracted much attention during the last decades owing to their versatile roles in many catalytic reactions involving carbon-carbon formation,[1] hydrogenation of many organic compounds,[2-4] oxidation of hydrocarbons,[5] isomerization,[6] and decomposition of nitrogen monoxide.[7] Among the numerous applications, direct alcohol fuel cells (DAFCs) are greatly highlighted due to their merits such as zero pollution, high volumetric energy density, easy transportation, renewable, and relatively low operating temperature.[8-9] Among different alcohol fuels, ethanol is more competitive with less toxicity, sustainability and higher energy density.[10] For direct ethanol fuel cells (DEFCs), the anode catalyst Pd is more demanded than the more common platinum (Pt) catalysts due to its lower cost, greater tolerance to CO species, and higher electro-catalytic activity in alkaline medium.[11-13]

The strategies to further minimize catalyst cost and to achieve full utilization of Pd atoms include clean Pd surface, small particle size, formation of alloy with cheaper metals, or fixture on the substrates.[14-15] To prevent the aggregation of small particles arising from the increased surface energy inherent with the small sizes,[16] considerable efforts have been devoted to stabilize the particles by using surfactants, polymers or ligands.[17-18] However, the strongly bonded organic materials on the catalytic nanoparticles (NPs) surface will inevitably prevent the full access to the electrolyte surroundings, which largely limit their performances.[18-19] In this case, introducing proper supports as another alternative is found to be advantageous since they can not only make low loading catalysts possible but also endow additional properties to the catalysts. The Pd-based alloys can not only minimize the usage of Pd but also demonstrate enhanced electrocatalytic activities. The introduced doping metal can alter the d-band center of alloy, thus facilitate the desorption of fuel species and making more active sites available on the catalytic metal.[20] For

example, PdSn,[21] PdCo,[22] PdNi[23] and PdAu[24] bimetallic catalysts have shown much higher catalytic activity and stability toward electrooxidation of formic acid, ethanol and oxygen reduction reaction (ORR) than the commercial Pd/C catalysts. Among the Pd-based alloys, iron-palladium (FePd) alloys with different nanostructures such as sphere,[25] rod,[26] core-shell,[27] leaf,[28] and ultrathin wire[29] have received dramatic interest due to their excellent catalytic performances in ORR, methanol oxidation and dechlorination.

Transition metal oxides have also shown as effective promoters or appropriate supporting materials for Pd-based electrocatalysts.[30-33] Metal oxides can alter the electronic structure of Pd through interfacial bonding and/or accelerating electron transfer between metal and oxide.[34] Catalysts with Pd supported on different oxide/C such as CeO_2, Co_3O_4, Mn_3O_4, and NiO have displayed much higher catalytic activity and stability than Pd/C or Pt/C electrocatalysts under comparable experimental conditions.[35] Among numerous transition metal oxides, magnetite and maghemite are of scientific and technological importance due to their intrinsic magnetic features, and intrigued electronic properties.[36] [37]

However, simple magnetic iron oxides are easily aggregated due to the dipole-dipole interactions and wan der Waals forces.[38] The conductivity will also be largely limited due to the poor conductivity of iron oxides. To overcome these problems, another substrate is further needed to disperse iron oxide particles. Nowadays, carbon materials such as carbon nanotubes (CNTs) have attracted intense interests due to their excellent electronic properties, good physicochemical stability, and large specific surface area.[39] Carboxylic groups on MWNTs have demonstrated a unique function to anchor the magnetic NPs uniformly on the MWNTs-COOH,[15] and the MWNTs behaved as spacers in the final catalysts to facilitate a good electrolyte access. In summary, an optimal combination of catalytic metal alloys, metal oxides promoter and highly conductive carbon

substrate could incorporate all the specific advantages in the final catalysts and contribute to an excellent catalytic performance.

Herein, we report a facile one-pot solution-based method as in-situ thermal decomposition of $Pd(acac)_2$ and $Fe(CO)_5$ in a refluxing dimethylformamide (DMF) solution where ultrafine FePd alloy were first formed and deposited on the Fe_2O_3 NPs, which were formed and evenly distributed on the MWNTs surface. The formed nanocatalysts were termed as "FePd-Fe_2O_3/MWNTs". Different iron substrates as Fe_3C and γ-Fe_2O_3 were obtained with varying the $Fe(CO)_5$ precursor dosage. The Pd/MWNTs and Fe_3O_4/MWNTs were also obtained as control experiments. The compositions of these iron-containing specimens were determined by Mössbauer spectrometer and X-ray photoelectron spectroscopy (XPS). The crystalline structures and morphologies of Pd/MWNTs, Fe_3O_4/MWNTs, FePd-Fe_3C/MWNTs and FePd-Fe_2O_3/MWNTs were investigated by X-ray diffraction (XRD) and transmission electron microscopy (TEM). The variation of defects on the tube wall surface after the deposition of NPs and was characterized by Raman spectroscopy and XPS. The thermal properties and final loadings of the as-synthesized nanocomposites were determined by thermogravimetric analysis (TGA). The electrocatalytic performances of these catalysts were evaluated for ethanol oxidation reaction (EOR) using cyclic voltammetry (CV), chronoamperometry (CA) and electrochemical impedance spectroscopy (EIS).

3.2. Experimental

3.2.1. Materials

Palladium (II) acetylacetonate ($Pd(C_5H_7O_2)_2$, 99%, Mw = 304.64 g/mol), iron(0) pentacarbonyl ($Fe(CO)_5$, 99%, Mw = 195.90 g/mol), potassium hydroxide (KOH, BioXtra, $\geqslant$85% KOH basis), dimethylformamide (DMF, 99%) and ethanol (C_2H_5OH, $\geq$99.5%) were obtained from Sigma Aldrich. Carboxylic group functionalized multi-walled nanotubes (MWNTs-COOH)

(**Stock#:** 1272YJF, content of MWNTs: ≥ 95 wt%, content of -COOH: 0.47-0.51 wt%, outside diameter: 50-80 nm, inside diameter: 5-15 nm, length: 10-20 μm) were provided by Nanostructured & Amorphous Materials, Inc., USA. All the chemicals were used as-received without any further treatment.

3.2.2. Synthesis of Catalysts

A facile one-pot solution-based method was employed to synthesize Pd/MWNTs, Fe_3O_4/MWNTs and FePd-alloyed nanocatalysts. Briefly, 100.0 mg MWNTs-COOH was first dispersed in 60 mL DMF solution undergoing 1h sonication, the solution was then transferred to a 250-mL 3-neck flask and heated to reflux (~160 °C) in ~ 20 min. For the synthesis of FePd-based nanocatalysts, 202.0 mg $Pd(acac)_2$ in 20 mL DMF was added to the refluxing MWNTs-COOH/DMF solution. $Fe(CO)_5$ (130.2, 437.0, and 875.0 mg) was following added to the solution after boiling again in ~ 5 min, the products were donated as FePd-Fe_3C/MWNTs, FePd-Fe_2O_3(3:5)/MWNTs and FePd-Fe_2O_3(3:10)/MWNTs, respectively. For the control synthesis of Pd/MWNTs and Fe_3O_4/MWNTs, only 202.0 mg $Pd(acac)_2$ or 875.0 mg $Fe(CO)_5$ was added to the refluxing MWNTs-COOH/DMF solution. All the solutions were maintained refluxing for additional 3 hours to complete the whole reaction. Finally, after cooling down to room temperature, the solid iron containing products were removed from the suspension using a permanent magnet while Pd/MWNTs were filtered under vacuum. All the final products (FePd-Fe_3C/MWNTs, FePd-Fe_2O_3(3:5)/MWNTs, FePd-Fe_2O_3(3:10)/MWNTs, Pd/MWNTs and Fe_3O_4/MWNTs) were rinsed with acetone 3 times and collected after vacuum drying at 60 °C for 24 hours.

3.2.3. Preparation of Working Electrode

The working glassy carbon electrode with a diameter of 3 mm was successively polished with 1.0 and 0.05 μm alumina powders on a microcloth wetted with doubly distilled water to produce

an electrode with a mirror-like surface. For the preparation of a catalyst coated electrode, 1.0 mg catalyst was added to 1.0 mL ethanol solution of nafion (the content of nafion is 0.1 wt%), the mixture was then treated for 30 min with ultrasonication to form a uniform suspension. The obtained suspension (5 μL) was dropped on the surface of well-treated glassy carbon electrode. Finally, the resultant modified glassy carbon electrode was dried naturally at room temperature.

3.2.4. Characterizations

The Mössbauer spectrometer was set to produce a high precision Doppler velocity modulation of the source γ radiation. The effects of the Doppler velocity modulation on the absorption of γ radiation were recorded synchronously in the 1024 channels of the multichannel analyzer. The result was 1024 numbers representing registered gamma quanta (representing a singular quantum) passing through the absorber under the condition of different Doppler velocity. A separate calibration procedure was used to establish the exact correspondence channel-velocity (Spectrometer calibration was performed by measuring a standard α-Fe absorber, which produces a well-known six line spectrum. The whole velocity range was calibrated using these six velocity points). The shape of absorption spectrum was fitted to a theoretical model line shape, which was a superposition of singlets, doublets and sextets (^{57}Fe case) of a Lorentzian form. The result was investigated by chi 2 criterion and the theoretical line shape was tailored to fit experimental spectrum by the adjustment of spectral parameters like isomer shift, quadrupole splitting, hyperfine magnetic field and etc.

The powder X-ray diffraction (XRD) analysis of the samples was carried out with a Bruker AXS D8 Discover diffractometer with GADDS (General Area Detector Diffraction System) operating with a Cu-Ka radiation source filtered with a graphite monochromator ($\lambda = 1.5406$ Å). The 2θ angular region between 10 and 80 ° was explored at a scan rate of 1 ° min^{-1}.

A transmission electron microscope (TEM) was used to characterize the morphology of the as-prepared nanocomposites in a JEOL 2010F microscope at a working voltage of 200 kV. The samples were prepared by drying a drop of ethanol suspension on a 400-mesh carbon-coated copper grid (Electron Microscopy Sciences).

Raman spectra were obtained using a Horiba Jobin-Yvon LabRam Raman confocal microscope with 785 nm laser excitation at a 1.5 cm^{-1} resolution at room temperature.

Thermogravimetric analysis (TGA) was conducted using a TA instruments Q-500 at a heating rate of 10 ˚C min^{-1} and an air flow rate of 60 mL min^{-1} from 25 to 700 ˚C.

X-ray photoelectron spectroscopy (XPS) measurements were performed on a Kratos AXIS 165 XPS/AES instrument. The samples were scanned with a monochromatic Al X-ray source at the anode of 10 kV and beam current of 15 mA. The peaks were deconvoluted into the components on a Shirley background

3.2.5. Electrochemical Evaluations

The electrochemical experiments were conducted in a conventional three-electrode cell. The as-prepared glassy carbon electrode deposited with catalyst was used as the working electrode, while saturated calomel electrode (SCE) (0.241 V vs. SHE) connected to the cell through a Luggin capillary served as reference electrode. All the potentials were referred to the SCE. All the electrochemical measurements were performed on an electrochemical working station VersaSTAT 4 potentiostat (Princeton Applied Research). Stable cycle voltammogram (CV) curves were recorded after potential sweeping for several cycles until the CV curve became stable in the potential region from −1.0 to 0.3 V. Chronoamperometry (CA) toward EOR was performed at -0.3 V in 1.0 M KOH solution containing 1.0 M ethanol for a duration of 1000 s. The

electrochemical impedance spectroscopy (EIS) was carried out in the frequency range from 100 000 to 0.1 Hz with a 10 mV amplitude at -0.3 V.

3.3. Results and Discussion

3.3.1. Mössbauer Spectra Analysis

Room temperature ^{57}Fe Mössbauer spectra as a powerful technique determining iron compounds were first employed to investigate the chemical environment of the as-synthesized nanocatalysts to determine the composition.[40] Figure 3.1 shows the spectral curves and the detailed data are listed in Table 3.1. For the FePd-Fe$_3$C/MWNTs, Figure 3.1(a), only one component as Fe$_3$C is obtained after curve fitting, which is evidenced by: isomer shift (IS) of 0.15 mm/s and the corresponding quadrupole splitting (QS) of 0.54 mm/s. Two components as Fe^{3+} and Fe$_3$C are obtained after curve fitting of FePd-Fe$_2$O$_3$(3:10)/MWNTs, Figure 3.1(b), The main component Fe^{3+}(95%) is located at IS (0.33 mm/s), hyperfine filed (HI) (490 kOe); IS (0.35 mm/s), HI (466 kOe) and IS (0.35 mm/s), HI (417 kOe), indicating the Fe^{3+} is in the frustrated oxygen sites of γ-Fe$_2$O$_3$ where the iron ions in octahedral-sites have different number with the nearest occupied octahedral-sites. The second component as Fe$_3$C (5%) is located at IS of 0.15 mm/s, QS of 0.60 mm/s. For curve fitting of Fe$_3$O$_4$/MWNTs, Figure 3.1(c), Fe$_3$O$_4$ is confirmed as Fe^{3+} (61%) in tetrahedral sites of Fe$_3$O$_4$ (IS, 0.32 mm/s, HI, 492kOe) and Fe$^{2.5+}$ in octahedral sites of Fe$_3$O$_4$ (IS, 0.63 mm/s, 454 kOe and IS, 0.50 mm/s, 450 kOe). Similar to FePd-Fe$_2$O$_3$(3:10)/MWNTs, the curve fitting of FePd-Fe$_2$O$_3$(3:5)/MWNTs indicates two components as 9% Fe$_3$C and 91% Fe^{3+}, Figure 3.1(d), the Fe^{3+} in the frustrated oxygen sites is demonstrated by IS of 0.35 mm/s, HI of 482 kOe (47%), IS of 0.35 mm/s, HI of 456 kOe (29%) and IS of 0.35 mm/s, 414 kOe (16%). In addition, Fe^{3+} (3%) in the distorted oxygen octahedral is demonstrated by IS of 0.35 mm/s, QS 0.53 mm/s. Finally, The 9% Fe$_3$C is located at IS of 0.1 mm/s with QS of 0.53 mm/s. It is noticed

Table 3.1. Room temperature mössbauer spectral data of the measured samples. (a) FePd-Fe$_3$C/MWNTs, (b) FePd-Fe$_2$O$_3$(3:10)/MWNTs, (c) Fe$_3$O$_4$/MWNTs and (d) FePd-Fe$_2$O$_3$(3:5)/MWNTs.

Sample code	Composition		
	Fe$_3$C	Fe$^{2.5+}$	Fe^{3+}
a	100%	/	/
b	5%	/	95%
c	/	39%	61%
d	9%	/	91%
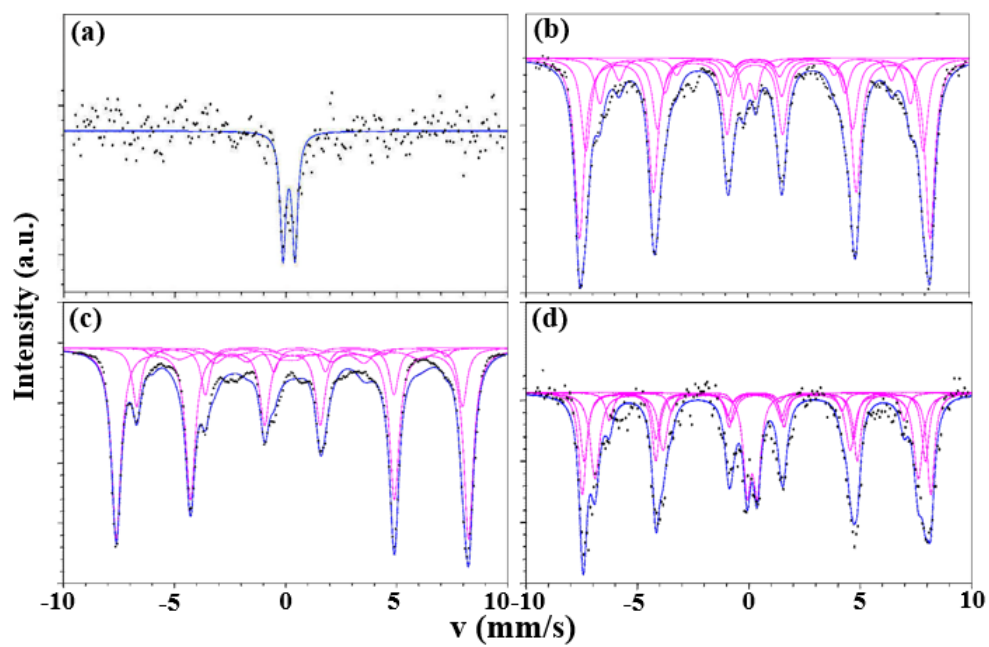
Figure 3.1. Mössbauer spectra of (a) FePd-Fe$_3$C/MWNTs, (b) FePd-Fe$_2$O$_3$(3:10)/MWNTs, (c) Fe$_3$O$_4$/MWNTs and (d) FePd-Fe$_2$O$_3$(3:5)/MWNTs.

that different precursor combinations have produced different iron components, Fe_3O_4 for simple decomposing $Fe(CO)_5$ in the DMF solution, Fe_3C with relatively lower $Fe(CO)_5$ precursor dosage, and γ-Fe_2O_3 for high $Fe(CO)_5$ dosage in the presence of $Pd(acac)_2$.

3.3.2. X-ray Diffraction

Figure 3.2 shows the XRD patterns of Pd/MWNTs, FePd-Fe_3C/MWNTs, FePd-Fe_2O_3(3:5)/MWNTs, FePd-Fe_2O_3(3:10)/MWNTs and Fe_3O_4/MWNTs, respectively. The standard diffraction patterns of γ-Fe_2O_3 (PDF#39-1346), Fe_3O_4 (PDF#65-3107) and Pd (PDF#88-2335) are also provided at the bottom of Figure 3.2. For Pd/MWNTs, four main diffraction peaks as C (0 0 2) centering at around 25.97° (PDF#26-1077), Pd (1 1 1), (2 0 0) and (2 2 0) centering at around 40.01, 46.54 and 67.65°, (PDF#88-2335), are clearly observed suggesting the successful deposition of Pd on MWNTs, Figure 3.2(a). For Fe_3O_4/MWNTs, Figure 3.2(e), partial characteristic peaks centering at 30.24, 35.63, 43.28, 53.73, 57.27, 62.93 and 74.47° are consistent with the (220) (311) (400) (422) (511) (440) and (533) planes of Fe_3O_4 (PDF#65-3107), respectively, indicating the successful deposition of Fe_3O_4 on MWNTs. However, since the standard patterns of γ-Fe_2O_3 (PDF#39-1346) and Fe_3O_4 (PDF#65-3107) are similar, Mossbauer spectra as a reliable technique evaluating the state of the synthesized iron oxides are referred as the final standard. For FePd-Fe_3C/MWNTs, FePd-Fe_2O_3(3:5)/MWNTs, and FePd-Fe_2O_3(3:10)/MWNTs, Figure 3.2(c-d), besides the main diffraction peaks of MWNTs, Fe_3C and γ-Fe_2O_3, one characteristic peak corresponding to the (111) plane of FePd (PDF#65-3253) is clearly observed, which is confirmed from the positive shift from Pd (111) (39.79°) to FePd (111) (40.47°).[41] In addition, the peak intensity of FePd (111) and C (002) is observed to decrease with increasing the $Fe(CO)_5$ precursor dosage due to the produced dominant iron oxide, the average crystallite size of Fe_2O_3 and Pd NPs can be estimated using Debye - Scherrer Equation (1).
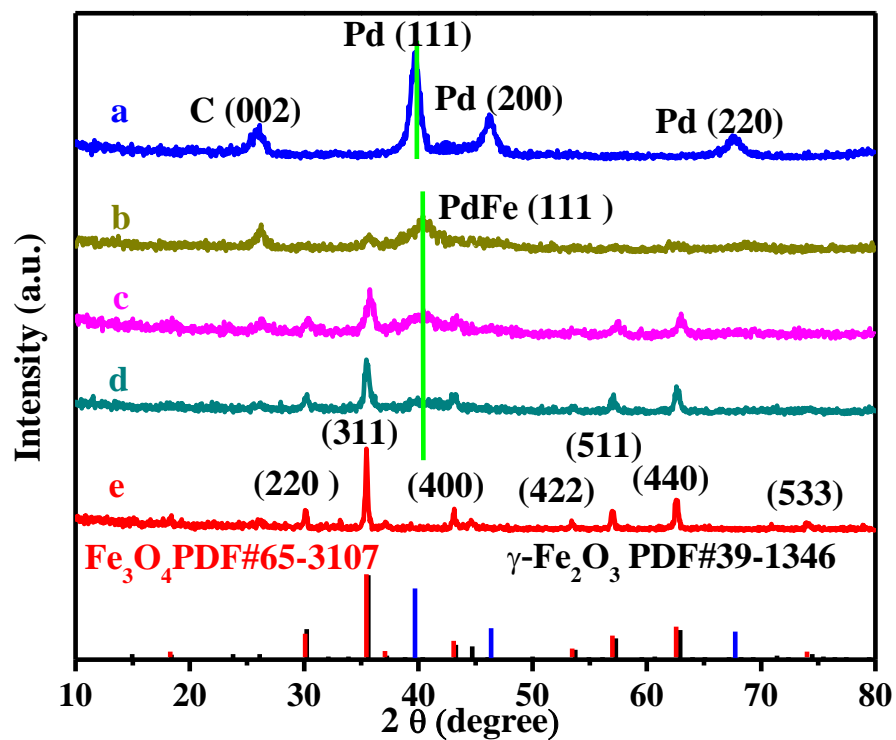
Figure 3.2. XRD patterns of (a) Pd/MWNTs, (b) FePd-Fe$_3$C/MWNTs, (c) FePd-Fe$_2$O$_3$(3:5)/MWNTs, (d) FePd-Fe$_2$O$_3$(3:10)/MWNTs and (e) Fe$_3$O$_4$/MWNTs, standard cards of Fe$_3$O$_4$, γ-Fe$_2$O$_3$ and Pd are shown at the bottom (red for Fe$_3$O$_4$, blue for γ-Fe$_2$O$_3$ and black for Pd).

$$L = 0.89\lambda/(\beta\cos\theta_B) \qquad (1)$$

where L is the particle size, λ is 1.5406 Å for the wavelength of Cu-Ka radiation, β is the full width at half-maximum (FWHM), and θ_B is the diffraction angle. The FWHM was calculated from the diffraction peak of the (311) plane of γ-Fe_2O_3 or Fe_3O_4 and (111) plane of Pd or FePd, the corresponding crystallite sizes of Fe_3O_4, γ-Fe_2O_3, Pd and FePd NPs in Pd/MWNTs, FePd-Fe_3C/MWNTs, FePd-Fe_2O_3(3:5)/MWNTs, FePd-Fe_2O_3(3:10)/MWNTs and Fe_3O_4/MWNTs are calculated and shown in Table 3.2. The size of iron oxide particle is observed to increase with increasing the $Fe(CO)_5$ precursor dosage. In contrast, the Pd/FePd particle size is also observed to decrease with increasing the $Fe(CO)_5$ dosage, which is probably due to the increasing $Fe(CO)_5$ amount resulted larger Fe_2O_3 particle.

3.3.3. Raman Spectroscopy

Raman spectroscopy is a useful technique to characterize carbonaceous materials, especially for analyzing the surface structure and distinguishing sp^2 and sp^3 hybridized forms of carbon. Figure 3.3(a-f) shows the Raman spectra of the as-received MWNTs-COOH, FePd-Fe_2O_3(3:10)/MWNTs, Fe_3O_4/MWNTs Pd/MWNTs, FePd-Fe_2O_3(3:5)/MWNTs and FePd-Fe_3C/MWNTs, respectively. All the samples exhibit the characteristic D, and G bands around ~ 1335 and 1580 cm^{-1}. The D band is a "dispersive" band, which is ascribed to the edges, other defects and disordered carbon, whereas G band is related to the stretching mode of crystal graphite. The intensity ratio of D to G bands (I_D/I_G) denoted as R is a measurement of the degree of disorder and average size of the sp^2 domain,[42] the higher the R, the larger the degree of defects. The calculated R values from Figure 3.3 of FePd-Fe_2O_3(3:10)/MWNTs (1.7656), Fe_3O_4/MWNTs (1.7570), Pd/MWNTs (1.7483), FePd-Fe_2O_3(3:5)/MWNTs (1.7810) and FePd-Fe_3C(2:1)/MWNTs (1.6202) are all higher than that of the as-received MWNTs-COOH (1.5239). This similar

Table 3.2. Particle size of deposited particles in different nanocomposites

Nanocatalysts	Fe_3O_4 or Fe_2O_3 size (nm)	Pd or FePd size (nm)
Fe_3O_4/MWNTs	31.4	/
Pd/MWNTs	/	8.5
FePd-Fe_2O_3(3:10)/MWNTs	15.6	2.5
FePd-Fe_2O_3(3:5)/MWNTs	10.6	4.3
FePd-Fe_3C/MWNTs	/	3.8
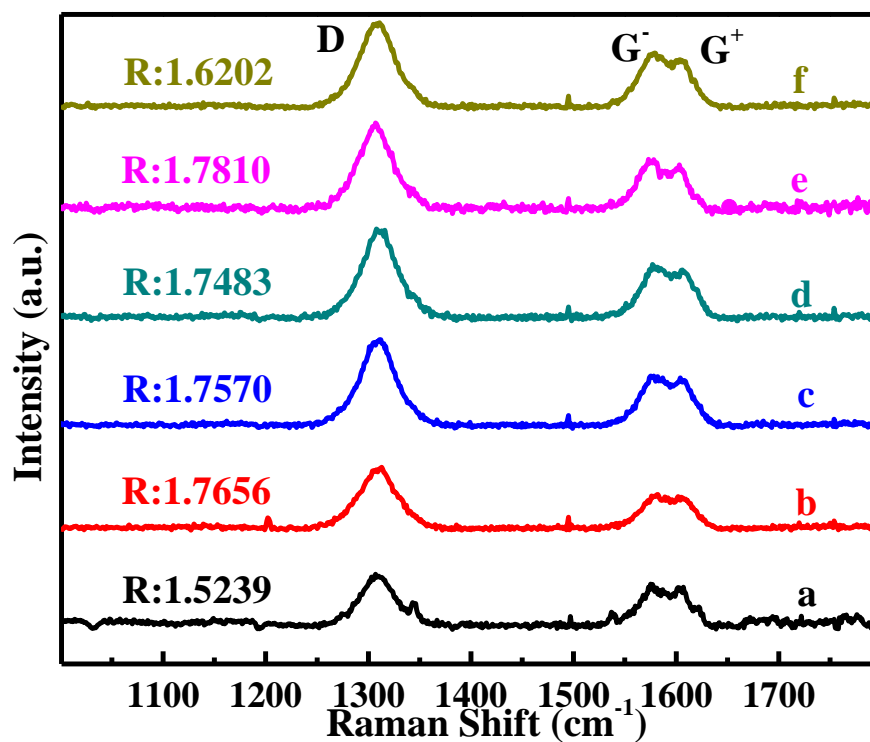
Figure 3.3. Raman spectra of **(a)** MWNTs-COOH, **(b)** FePd-Fe$_2$O$_3$(3:10)/MWNTs, **(c)** Fe$_3$O$_4$/MWNTs, **(d)** Pd/MWNTs, **(e)** FePd-Fe$_2$O$_3$(3:5)/MWNTs, and **(f)** FePd-Fe$_3$C/MWNTs.

phenomenon has also been observed in the GO and CNFs,[43-44] indicating a possible chemical interactions or bonds between the NPs and MWNTs.

3.3.4. TGA Analysis

TGA analysis is considered as a useful tool to determine the thermal stability and metal loading of carbon supported catalysts. Figure 3.4(a-e) shows the TGA curves of Fe_3O_4/MWNTs, Pd/MWNTs, FePd-Fe_2O_3(3:5)/MWNTs, FePd-Fe_2O_3(3:10)/MWNTs, and FePd-Fe_3C/MWNTs. For Fe_3O_4/MWNTs, Figure 3.4(a), a slight weight-up begins at 150 °C is observed due to the oxidation of Fe_3O_4, which is consistent with the Mossbauer result and different from the other four nanocomposites, Figure 3.4(b-e). Slight weight-losses are first observed for the Pd containing nanocatalysts due to the continuous decomposition of remained acetylacetonate (acac) on the Pd surface.[15] However, a following weigh increase is observed due to the oxidation of metal Pd or FePd. A common fast weight decrease is observed for all these five nanocatalysts as the temperature reaches 500 °C due to the burning of MWNTs. The final residue percentages of Fe_3O_4/MWNTs, Pd/MWNTs, FePd-Fe_2O_3(3:5)/MWNTs, FePd-Fe_2O_3(3:10)/MWNTs, and FePd-Fe_3C/MWNTs are determined to be 78.80, 41.42, 74.92, 79.54 and 60.55 %. The loading of Pd in Pd/MWNTs is determined to be 37.85 % from the TGA result. For Fe_3O_4/MWNTs, FePd-Fe_2O_3(3:10)/MWNTs, FePd-Fe_2O_3(3:5)/MWNTs and FePd-Fe_3C/MWNTs, the varying trend of the final residue is in good accordance with the iron precursor dosage. However, the final residue of 80 % indicates a saturation of MWNTs when further increasing the $Fe(CO)_5$ dosage. Energy-dispersive X-ray spectroscopy (EDS) is introduced to determine the Pd loading, Figure A3.11. The element Pd, Fe, C and O are clearly observed, suggesting the successful synthesis of FePd-Fe_2O_3/MWNTs or FePd-Fe_3C/MWNTs nanocatalysts. The Pd loading is determined to be 13.12,
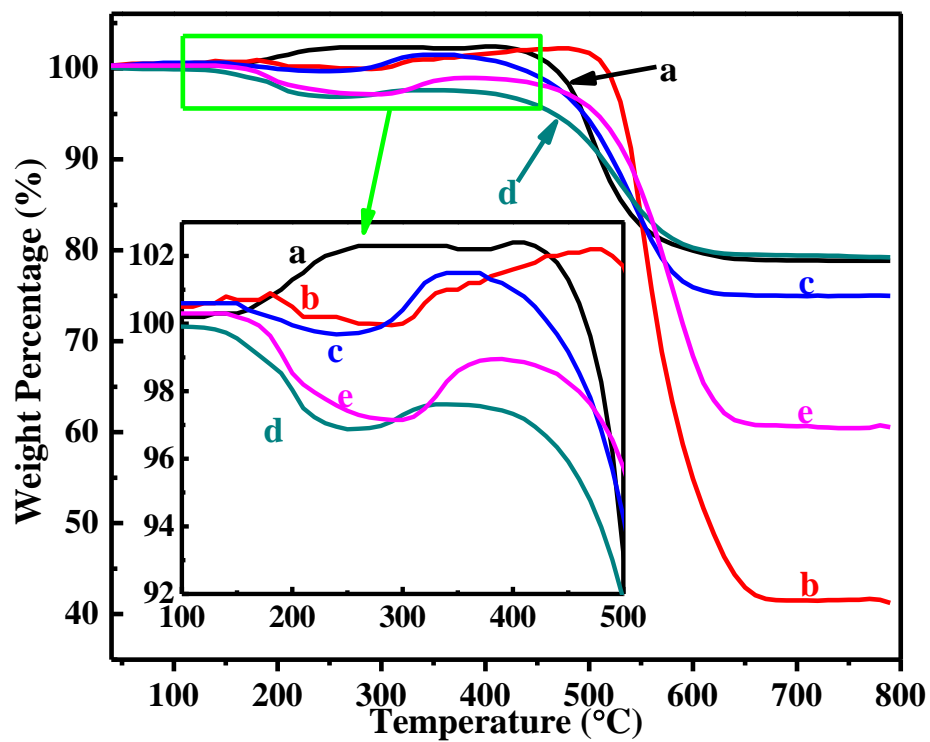
Figure 3.4. TGA curves of (a) Fe_3O_4/MWNTs, (b) Pd/MWNTs, (c) FePd-Fe_2O_3(3:5)/MWNTs, (d) FePd-Fe_2O_3(3:10)/MWNTs and (e) FePd-Fe_3C/MWNTs, inset is the enlarged part of the rectangle area.

20.66, and 30.03 % for the FePd-Fe$_2$O$_3$(3:10)/MWNTs, FePd-Fe$_2$O$_3$(3:5)/MWNTs and FePd-Fe$_3$C/MWNTs nanocatalysts.

3.3.5. TEM Characterizations

Figure 3.5 shows TEM microstructures of the Pd/MWNTs, Fe$_3$O$_4$/MWNTs and Pd-Fe$_3$C/MWNTs with corresponding HRTEM images and selected area electron diffraction (SAED) patterns. For Pd/MWNTs, the Pd NPs are observed to be uniformly decorated on the tube wall surface with an average particle size of ~15 nm Figure 3.5(a). Clear lattice space of 2.38 and 2.28 Å are observed belonging to the (111) plane, and kinetically forbidden reflections of Pd 1/3(422) of face-centered cubic (fcc) Pd, Figure 3.5(b), respectively.[45] In addition, four planes assigned to Pd (111), (220), (200) and (311) are also clearly noticed in the SAED pattern, Figure 3.5(c). Both the distinguished lattice fringes and the marked SAED facets indicate a successful synthesis of Pd/MWNTs, which is also consistent with the XRD result. For Fe$_3$O$_4$/MWNTs, Figure 3.5(d), the Fe$_3$O$_4$ NPs with an average diameter of 30 nm are clearly observed anchoring on the tube wall surface, demonstrating the facile synthesis of Fe$_3$O$_4$/MWNTs. A lattice fringe of 4.67 Å belonging to the (111) plane of fcc Fe$_3$O$_4$ is clearly observed in the HRTEM image, Figure 3.5(e). For the SAED pattern shown in Figure 3.5(f), the planes of (111), (220), (311), (400), (422), (440), (533) and (511) of Fe$_3$O$_4$ are well distinguished, indicating the existence of Fe$_3$O$_4$, consistent with the Mossbauer spectra. For Pd-Fe$_3$C/MWNTs, the formed NPs are observed randomly distributed on the MWNTs with serious agglomeration, Figure 3.5(g). Irregular NPs covered on the tube wall surface and the clear lattice spaces of 2.21, 2.25, and 2.02 Å belonging to FePd (111), Fe$_3$C (002) and Fe$_3$C (220), are observed, Figure 3.5(h). For the SAED pattern, Figure 3.5(i), apart from the Fe$_3$C planes of (210), (102), (301), (040), (211), and (222), the (111) plane of FePd is also obtained, indicating the formation of FePd alloy and consistent with the XRD result.[46-49]
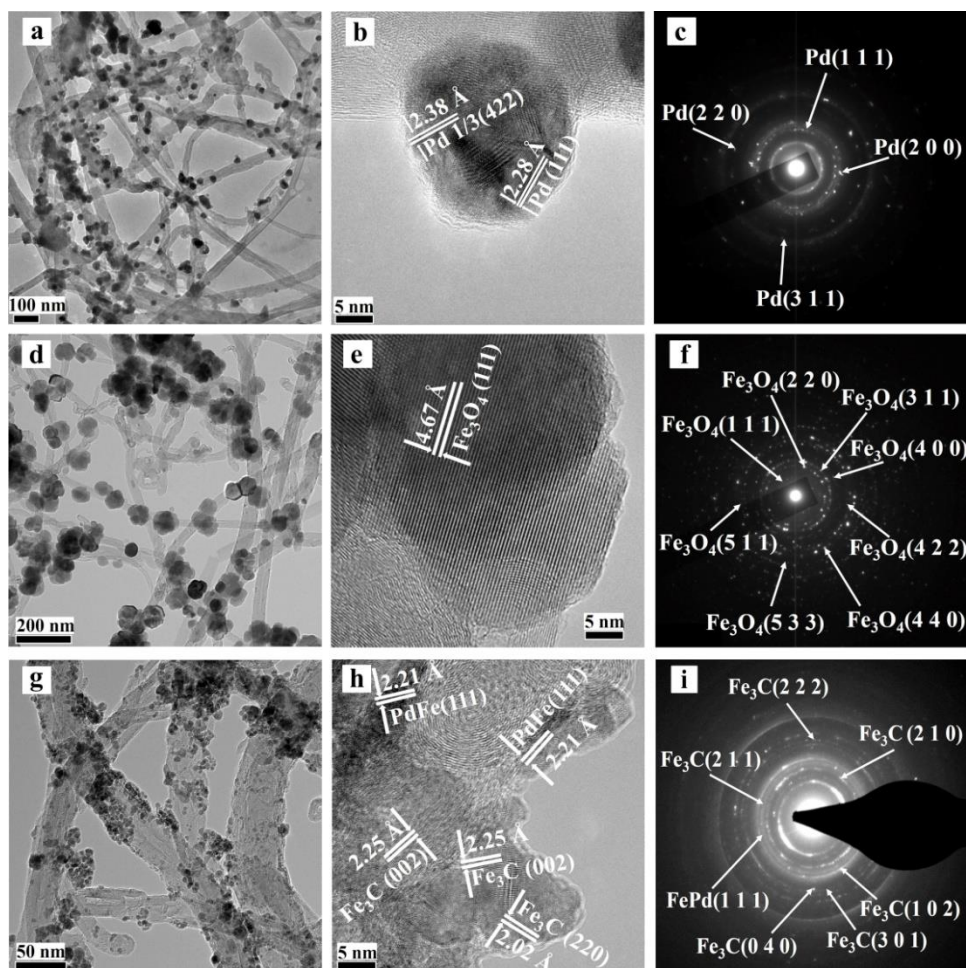
Figure 3.5. TEM image (a, d, g) and corresponding HRTEM image (b, e h) with clear lattice fringe as well as SAED pattern (c, f, i) with marked facet of (a-c) Pd/MWNTs, (d-f) Fe₃O₄/MWNTs and (g-i) Pd-Fe₃C/MWNTs.

Figure 3.6(a) shows the TEM image of FePd-Fe$_2$O$_3$(3:10)/MWNTs, relatively larger Fe$_2$O$_3$ NPs are observed to disperse on the tube wall surface with a slight agglomeration. However, ultrafine NPs are observed further deposited on the surface of Fe$_2$O$_3$ NPs at a closer look. The morphology of ultrafine NPs is further confirmed by the HRTEM image, Figure 3.6(b), the small FePd particles are uniformly distributed on the surface of Fe$_2$O$_3$ NPs. Clear Lattice fringes of 2.21 and 2.71 Å belonging to FePd (111) and FePd (110) are observed, indicating the formation of FePd alloy. Pure Pd NPs are also obtained on the tube wall surface or Fe$_2$O$_3$ surface as indicated by the Pd (111) plane. SAED pattern further discloses the crystallization, both FePd (110, 220 and 200) and γ-Fe$_2$O$_3$ (311, 511 and 440) are observed Figure 3.6(c), indicating the existence of γ-Fe$_2$O$_3$ and FePd alloy as confirmed by the XRD results.

Energy-filtered TEM (EFTEM) was also performed to provide a 2-dimensional (2-D) elemental distribution. In the EFTEM image, a brighter area always represents a higher concentration of the corresponding element in this area.[50] Figure 3.6(d-g) shows the element maps of (a) C + Fe, (b) C + Fe + Pd, (c) C + Fe + O, and (d) C + Fe + Pd +O, respectively, where red stands for oxygen, blue for carbon, green for iron, and pink for palladium. The irons are observed evenly distributed on the surface of MWNTs (whereas the lacy grid is also made of carbon), Figure 3.6(d). Compared with Figure 3.6(d), bright pink dots representing the Pd elements are clearly seen on the surface of large green particles, Figure 3.6(e). Figure 3.6(f) displays a uniform coverage of red oxygen on the basis of Figure 3.5(a), confirming the formation of iron oxides. Finally, the summation of C, Fe O and Pd distributions is shown in Figure 3.6(g), the pink Pd dotes are evenly distributed on the green Fe, which are further anchored on the blue nanotubes together with a coverage of red O. All these results suggest the containments of Pd, Fe O and C elements
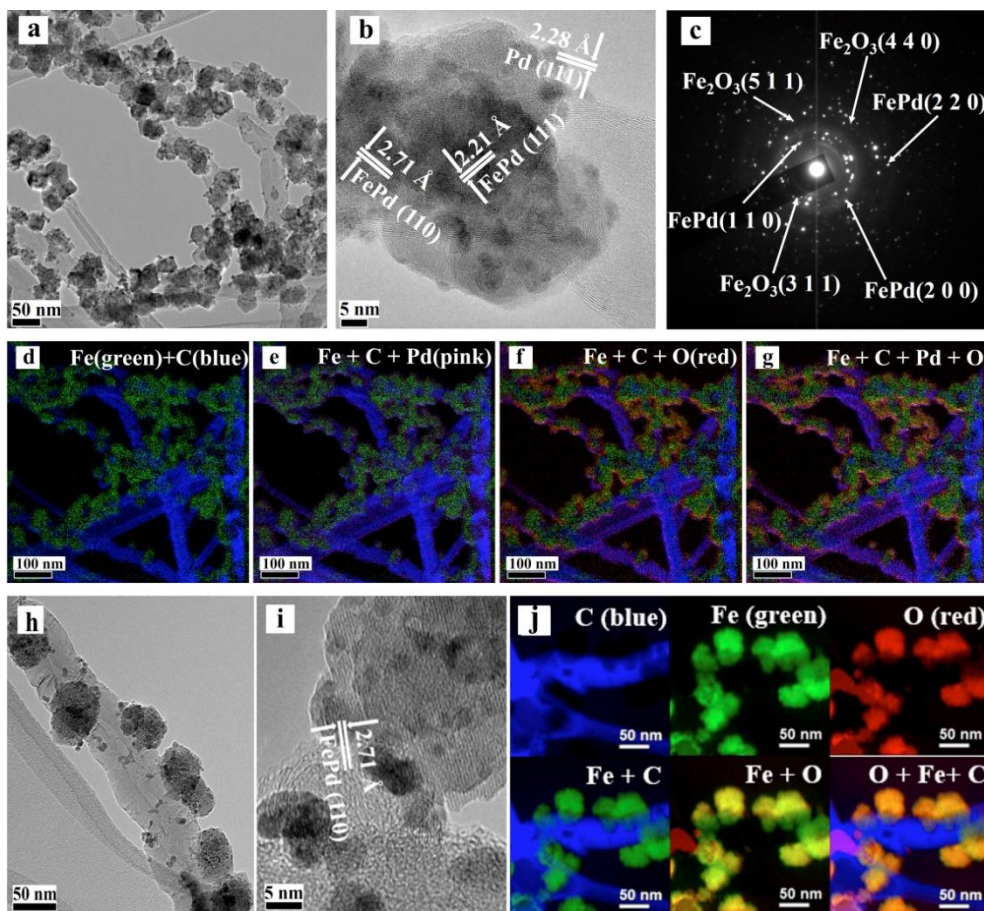
Figure 3.6. (a-c) TEM, SAED pattern and HRTEM image of FePd-Fe₂O₃(3:10)/MWNTs, (d-g) corresponding EFTEM maps as (d) Fe + C, (e) Fe + C + Pd, (f) Fe + C + O and (g) Fe + C + Pd + O of FePd-Fe₂O₃(3:10)/MWNTs, (h&i) TEM and HRTEM images of FePd-Fe₂O₃(3:5)/MWNTs and (j) mapping result of corresponding elements of FePd-Fe₂O₃(3:5)/MWNTs.

and further confirm the distribution of the Pd NPs on the Fe_2O_3 NPs, the Fe_2O_3 NPs on MWNTs. Similarly, Figure 3.6(h-j) shows the TEM, HRTEM images and corresponding C, O and Fe mappings of FePd-Fe_2O_3(3:5)/MWNTs nanocatalysts, similar structure is observed that the ultrafine NPs are firstly deposited on the Fe_2O_3 NPs, which are further dispersed on the tube wall surface. However, the relatively sparse dispersion of Fe_2O_3 NPs compared with that in FePd-Fe_2O_3(3:10)/MWNTs is probably due to the lower $Fe(CO)_5$ precursor dosage. Finally, similar distributions of C, O and Fe elements are also observed in Figure 3.6(j), which are consistent with that of FePd-Fe_2O_3(3:10)/MWNTs.

3.3.6. XPS Analysis

XPS is a powerful tool to provide valuable insights into the surface of solid samples and to identify the atomic composition of the solid surface, the valence state of elements can also be determined based on the specific binding energy measured from a particular type of photoelectron. Figure. 3.7(A) is the wide scan survey of FePd-Fe_2O_3(3:5)/MWNTs over a range of 0-1000 eV. Five main spectra peaks centering at ca. 85.46, 279.14, 330.15, 527.84 and 711.67 eV are clearly observed corresponding to Fe 3p, C 1s, Pd 3d, O 1s, and Fe 2p emissions, indicating the successful synthesis of FePd-Fe_2O_3(3:5)/MWNTs.[51-52] In contrast, for the wide scan survey of Pd/MWNTs, only three characteristic peaks as O 1s, Pd 3d, and C1s are observed, Figure 3.7(E), further demonstrating the successful synthesis of Pd/MWNTs and the introduction of Fe in the FePd-Fe_2O_3/MWNTs nanocatalysts as confirmed by the wide scan survey of FePd-Fe_2O_3(3:5)/MWNTs, Figure 3.7(A). For the high-resolution scan survey of FePd-Fe_2O_3(3:5)/MWNTs, Figure 3.7(B) is the curve fitting of C 1s, four peaks as C-C, C-O, C=O and O-C=O are smoothly deconvoluted, demonstrating that the structure of functionalized MWNTs has not been destroyed during the
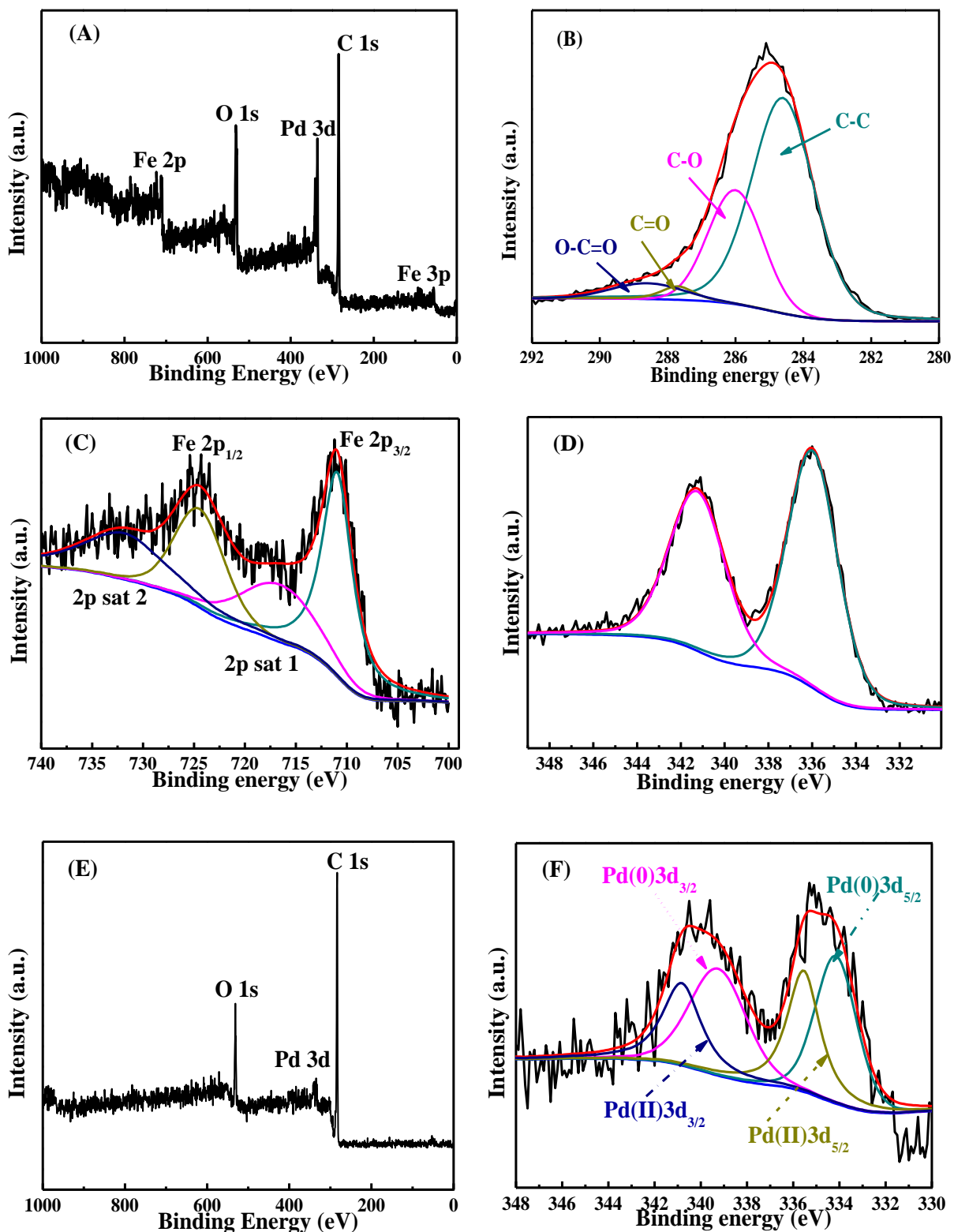
Figure 3.7. (A) Wide-scan survey of FePd-Fe₂O₃(3:5)/MWNTs, curve fitted elements in FePd-Fe₂O₃(3:5)/MWNTs as (B) C 1s, (C) Fe 2p, and (D) Pd 3d, (E&F) wide-scan survey and curve fitting spectra of Pd/MWNTs and Pd 3d.

73

synthesis process. For the deconvolution of Fe 2p, Figure. 3.7(C), the centers of electron-binding energy of Fe $2p_{3/2}$ and Fe $2p_{1/2}$ are 710.72 and 724.15 eV, respectively. The shakeup satellite structures at the higher binding energy sides of the main peaks are the fingerprints of the electronic structure of r-Fe_2O_3, which are in good agreement with the previously reported spectra of γ-Fe_2O_3.[53-55] For the curve fitting of Pd 3d in FePd-Fe_2O_3(3:5)/MWNTs, Figure. 3.7(D), great differences are observed compared with that of Pd/MWNTs, Figure 3.7(F). The XPS spectrum of the Pd 3d in Pd/MWNTs is curve-fitted with four peaks, i.e., 334.71 and 340.30 eV correspond to the orbits of Pd $3d_{5/2}$ and Pd $3d_{3/2}$ of metal Pd and the peaks located at 336.59 and 342.36 eV are assigned to the Pd $3d_{5/2}$ and Pd $3d_{3/2}$ orbits of Pd(2+).[56] However, for FePd-Fe_2O_3(3:5)/MWNTs, only two peaks centering around 335.89 and 341.52 are deconvoluted to metal Pd $3d_{5/2}$ and Pd $3d_{3/2}$, Figure 3.7(D). The peaks of metal Pd $3d_{5/2}$ and Pd$3d_{3/2}$ both are observed to shift to higher values compared with that of Pd/MWNTs, confirming the 'FePd' alloy-like formation.[41] This shift of binding energy is probably due to the modification of electronic structure of Pd as the electron will transfer from Fe to Pd due to the electronegativity of Fe. The d band of Pd will also be altered due to the intra-atomic or inter-atomic charge transfers between Fe and Pd after they are alloyed together.[41, 57-59] This electron transfer will probably contribute to the enhanced tolerance stability of CO species, which can greatly facilitate EOR.[60] This strong evident about the formation of FePd alloy is also consistent with the aforementioned XRD and TEM results. For Fe_3O_4/MWNTs, FePd-Fe_2O_3(3:10)/MWNTs and FePd-Fe_3C/MWNTs, the high-resolution scan surveys of Fe 2p are provided in Figure A3.12(A) and compared with that of FePd-Fe_2O_3(3:5)/MWNTs, typical features of different iron oxides are clearly observed, consistent with the Mössbauer spectra. In addition, similar Pd 3d peak phenomena are also observed in FePd-Fe_2O_3(3:10)/MWNTs and FePd-Fe_3C/MWNTs, Figure A3.12(B), indicating the formation of FePd alloy.

3.3.7. Electroactivity Evaluation

Cyclic voltammetry (CV) is a useful and convenient technique for estimating the electrochemically active surface area (*ECSA*) of Pd-based catalysts. The *ECSA* can not only provide important information about the active sites of catalysts, but also evaluate the access of conductive paths to transfer electrons to and from the electrode surface.[61] Figure 3.8(A&C) present the CVs of Fe_3O_4/MWNTs, Pd/MWNTs, FePd-Fe_2O_3(3:10)/MWNTs, FePd-Fe_3C/MWNTs and FePd-Fe_2O_3(3:5)/MWNTs in 1.0 M KOH solution at a scan rate of 50 mV/s with current density normalized to catalyst area and Pd mass, respectively. For Fe_3O_4/MWNTs, Figure 3.8A(a), negligible peaks are observed due to its non-activity compared with that of Pd-containing nanocatalysts, which are all characterized with flat anodic peak (E= 0.3 V) and strong cathodic peak (E= -0.4 V) representing the formation and reduction of palladium oxide (PdO), respectively. Furthermore, the FePd-Fe_3C/MWNTs, FePd-Fe_2O_3(3:10)/MWNTs and FePd-Fe_2O_3(3:5)/MWNTs (Figure 3.8A(c-e)) are observed to exhibit remarkable higher specific current magnitudes and wider potential reduction ranges than that of Pd/MWNTs during the reduction of PdO, Figure 3.8(C). The *ECSA* of Pd-based nanocatalysts for EOR in alkaline medium is usually measured based on the columbic charge for the reduction of PdO during the negative scan and using Equation (2).[62]

$$ECSA = Q / SL \qquad (2)$$

where '*S*' is the proportionality constant used to relate charges with area under an assumption that a monolayer of PdO is covered on the surface, the charge produced by the reduction of the monolayer PdO is 405 μC cm^{-2}. '*L*' is the catalyst loading in 'g'. The calculated *ECSA* values for Pd/MWNTs, FePd-Fe_2O_3(3:10)/MWNTs, FePd-Fe_3C/MWNTs and FePd-Fe_2O_3(3:5)/MWNTs are shown in Table 3.3. The *ECSA* value of Pd/MWNTs is greatly increased after introducing Fe. In
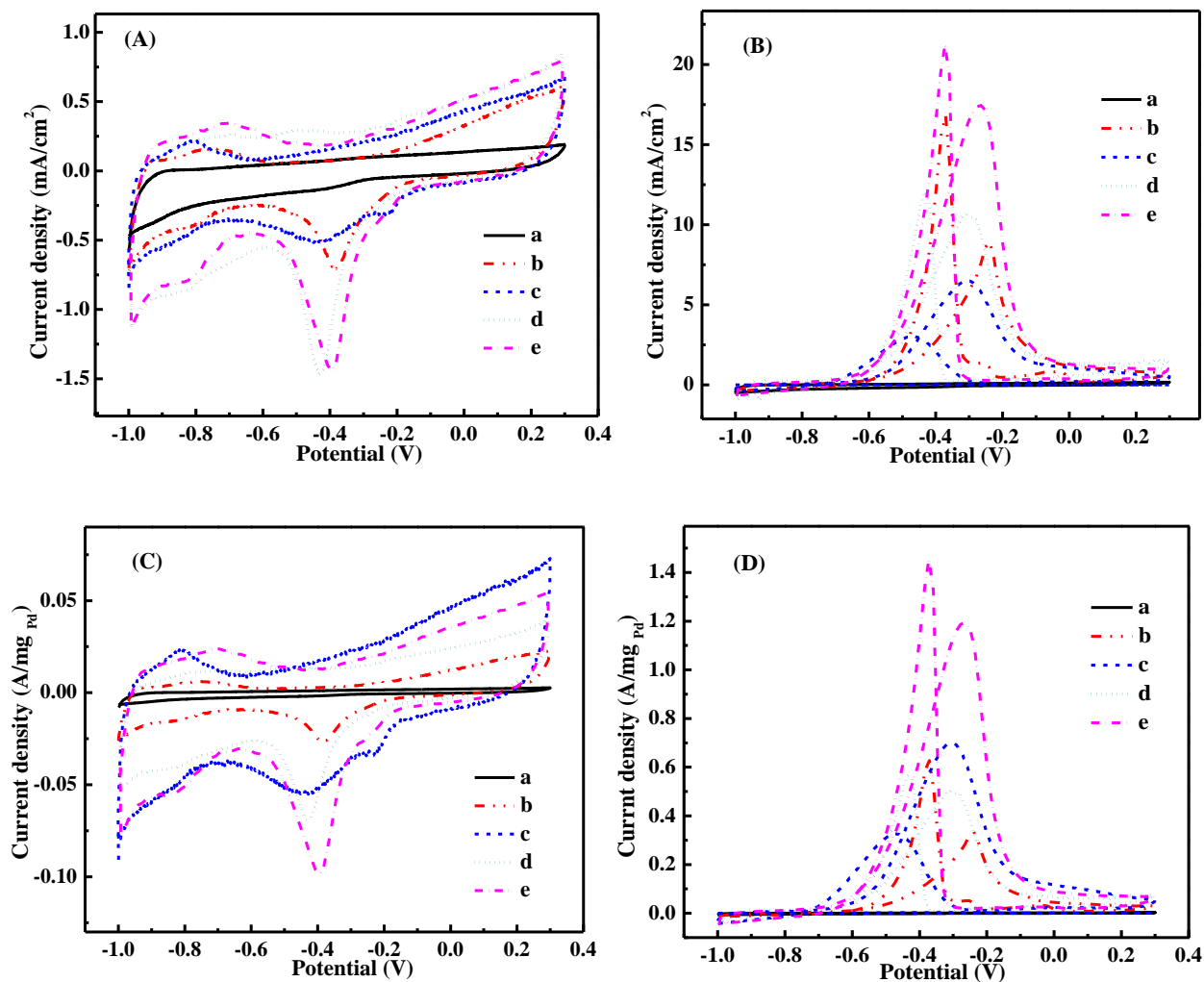
Figure 3.8. Cyclic voltammetry (CV) of (a) Fe₃O₄/MWNTs, (b) Pd/MWNTs, (c) FePd-Fe₂O₃(3:10)/MWNTs, (d) FePd-Fe₃C/MWNTs and (e) FePd-Fe₂O₃(3:5)/MWNTs in (A) 1.0 M KOH (B) 1.0 M KOH solution containing 1.0 M ethanol with current density normalized to catalyst mass at a scan rate of 50 mV/s. (C&D) same CVs as (A&B) with current density normalized to Pd mass.

Table 3.3. CV results for different nanocatalysts.

nanocatalysts	$ECSA$ (m^2 g^{-1})	j_p (mA/cm^2)	j_p (A/mg $_{Pd}$)
Pd/MWNTs	25.35	9.026	0.326
FePd-Fe$_2$O$_3$(3:10)/MWNTs	115.3	6.485	0.698
FePd-Fe$_2$O$_3$(2:1)/MWNTs	64.09	10.76	0.501
FePd-Fe$_2$O$_3$(3:5)/MWNTs	120.4	17.52	1.191

addition, the *ECSA* value of Pd-Fe$_3$C/MWNTs is also increased when continue increasing the Fe(CO)$_5$ precursor dosage. However, the *ECSA* values keep almost constant when further increasing Fe(CO)$_5$ as indicated by FePd-Fe$_2$O$_3$(3:5)/MWNTs (120.4 m^2 g^{-1}) and FePd-Fe$_2$O$_3$(3:10)/MWNTs (115.3 m^2 g^{-1}) due to the fully utilized Pd element. The highest *ESCA* value of (120.4 m^2 g^{-1}) is achieved in FePd-Fe$_2$O$_3$(3:5)/MWNTs probably due to the optimal ratio of MWNTs and Fe$_2$O$_3$ NPs and the increased active sites after introducing FePd alloy and Fe$_2$O$_3$ substrate. Finally, detectable positive shifts of the PdO on-set reduction peaks are clearly seen after the introduction of Fe, demonstrating easier reductions of PdO after modified with Fe due to the electronegativity of Fe.[63]

The electrocatalytic activities of these five nanocatalysts towards EOR were studied in a mixture of 1.0 M KOH aqueous solution containing 1.0 M ethanol at a scan rate of 50 mV s^{-1} from -1.0 to 0.3 V, Figure 3.8(B). The corresponding CVs with current density normalized to Pd mass are also shown in Figure 3.8(D). For Fe$_3$O$_4$/MWNTs, no oxidation peak of EOR is observed, Figure 3.8D(a), due to the non-activity of Fe$_3$O$_4$/MWNTs. For Pd containing nanocatalysts, Figure 3.8(D)b-e, typical voltammetric characteristics of electrooxidation of ethanol are clearly seen, such as EOR oxidation peak during the forward scan at around ~ -0.25 V and another shape anodic peak during the reverse scan associated with the oxidation of fresh ethanol after the reduction of PdO at ~ -0.43 V. The mass peak current density (j_p) and onset potential in the forward scan are main parameters to evaluate their eletrocatalytic activities for EOR. The electrocatalytic activities are observed to follow the order: FePd-Fe$_2$O$_3$(3:5)/MWNTs > FePd-Fe$_3$C/MWNTs > Pd/MWNTs > FePd-Fe$_2$O$_3$(3:10)/MWNTs based on catalyst area. However, the order changes to FePd-Fe$_2$O$_3$(3:5)/MWNTs > FePd-Fe$_2$O$_3$(3:10)/MWNTs > FePd-Fe$_3$C/MWNTs > Pd/MWNTs after normalizing to Pd mass, suggesting that the catalytic activity of Pd can be greatly enhanced after

the introduction of Fe. In addition, the onset potential also follows the same trend as j_p, suggesting an easier EOR after the introduction of Fe. Finally, the j_p of FePd-Fe$_2$O$_3$(3:5)/MWNTs (1.2 A/mg $_{Pd}$) is observed to largely outweigh others and the onset potential is also the lowest one among all the nanocatalysts, both indicating the highest activity of FePd-Fe$_2$O$_3$(3:5)/MWNTs as confirmed by the *ECSA* analysis.

3.3.8. Tolerance Stability

In order to further probe the long-term tolerance of these nanocatalysts toward intermediate carbonaceous species, chronoamperometric (CA) measurements were performed at -0.3 V for a duration of 1000 s in 1.0 M KOH solution containing 1.0 M ethanol. Figure 3.9(A&B) shows the CA curves after normalizing the current to catalyst area and Pd mass, respectively. All the polarization currents decay rapidly during the initial period, implying the poisoning of nanocatalysts by the intermediate carbonaceous species. Gradually, the current is decayed and a pseudosteady state is achieved. Among all the nanocatalysts in Figure 3.9(B), Pd/MWNTs (Figure 3.9(B)a) exhibit a fast decay rate and achieve the lowest extreme current, demonstrating a poor tolerance stability towards poisoning species. However, for FePd-Fe$_2$O$_3$/MWNTs catalysts, an enhanced stability is observed after the normalization to Pd mass, which is probably due to the formed FePd alloy and the positive effects of Fe$_2$O$_3$ and MWNTs substrates. In addition, the FePd-Fe$_2$O$_3$(3:5)/MWNTs are observed to display the slowest decay rate and are able to maintain the highest stable current density for the whole duration of time, indicating the best tolerance stability of FePd-Fe$_2$O$_3$(3:5)/MWNTs toward poisoning species.

3.3.9. Reaction Kinetics Evaluation

Electrochemical impedance spectroscopy (EIS) has been demonstrated to be a sensitive electrochemical technique for the study of the electrooxidation kinetics toward EOR. In this study,
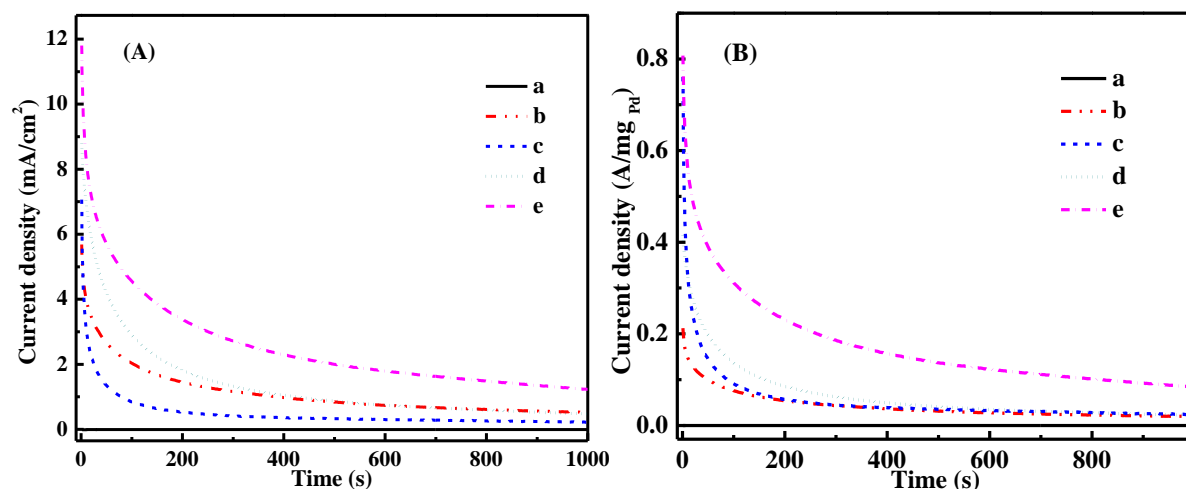
Figure 3.9. (A) Chronoamperometry (CA) curves of EOR on (a) Fe_3O_4/MWNTs, (b) Pd/MWNTs, (c) FePd-Fe_2O_3(3:10)/MWNTs, (d) FePd-Fe_3C/MWNTs and (e) FePd-Fe_2O_3(3:5)/MWNTs at -0.3 V (vs. SCE) with catalyst mass-based current density, (B) CAs with the current density normalized to Pd mass.

semicircular Nyquist plots of imaginary ($Z''(\Omega)$) versus real ($Z'(\Omega)$) components of impedance are shown in Figure 3.10, the illustrations are obtained with the potential fixing at -0.4 V with respect to SCE. For Fe_3O_4/MWNTs, Figure 3.10(a), the observed nearly straight line indicates a huge transfer resistance and further demonstrates the non-catalytic activity of Fe_3O_4/MWNTs. For Pd/MWNTs, FePd-Fe_2O_3(3:10)/MWNTs, FePd-Fe_3C/MWNTs and FePd-Fe_2O_3(3:5)/MWNTs, Figure 3.10(b-e), typical characteristics of EIS plots are observed as a semicircle in the high frequency region and a tail followed in the low frequency region. The diameter of the primary semicircle can be used to measure the charge transfer resistance (R_{ct}) of the catalyst, which has a physical meaning to evaluate how fast the rate of charge transfer is during the oxidation process.[64] Therefore, a decrease in the diameter of the semicircular Nyquist plot signifies a decrease in R_{ct} and an enhancement of charge transfer reaction kinetics. The R_{ct} values of the nanocatalysts are estimated by fitting the EIS curves with the software ZsimpWin based on an equivalent electric circuit as shown in the inset of Figure 3.10. In this R_s (R_{ct} CPE) circuit, R_s represents the uncompensated solution resistance, R_{ct} represents the charge-transfer resistance while the meaning of constant phase element (CPE) is a parameter related to the capacitor property. The parallel combination of R_{ct} and CPE takes into account the non-equilibrium charge transfer through the thin electrode film and the whole ethanol adsorption and oxidation process. The parallel combination (R_{ct} CPE) leads to a depressed semicircle in the corresponding Nyquist impedance plot. The values for all the parameters R_s, R_{ct}, CPE and their associated % error are summarized in Table 3.4. The R_s values are observed to be almost the same, Table 3.4, due to the same solution resistance. However, the R_{ct} values of FePd-Fe_2O_3/MWNTs nanocatalysts are much smaller than that of Pd/MWNTs, implying greatly enhanced R_{ct} values due to the formation of FePd alloy and the Fe_2O_3 substrate. For details, the R_{ct} value of FePd-Fe_2O_3(3:10)/MWNTs is observed to be ten
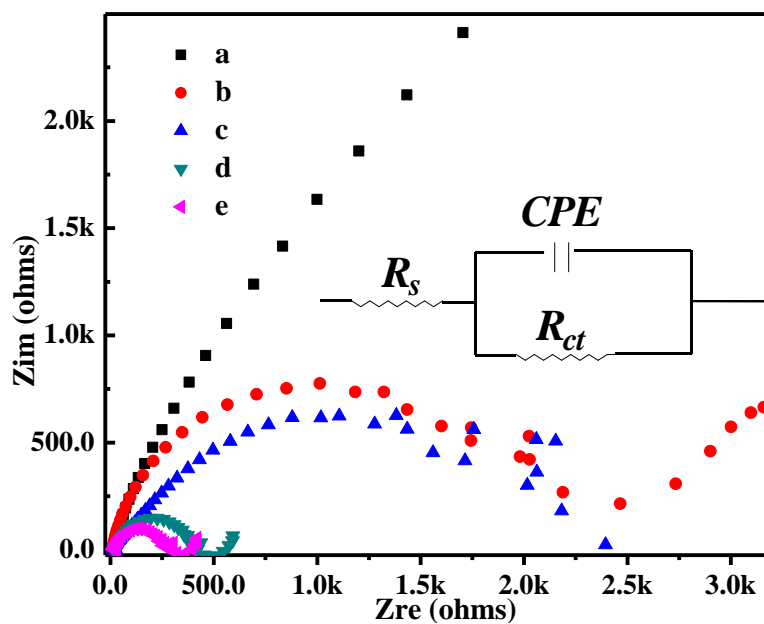
Figure 3.10. EIS spectra of (a) Fe$_3$O$_4$/MWNTs, (b) Pd/MWNTs, (c) FePd-Fe$_3$O$_4$(3:10)/MWNTs, (d) FePd-Fe$_3$C/MWNTs and (e) FePd-Fe$_2$O$_3$(3:5)/MWNTs in 1.0 M KOH solution containing 1.0 M ethanol at -0.4 V vs. SCE, inset is the equivalent circuit used to fit the impedance spectra.

Table 3.4. Impedance components for different electrodes by fitting the experimental data using Zsimp-Win software based on the equivalent circuit presented inset of Figure 3.10.

electrode	R_s / Ω		R_{ct} / Ω		CPE	
	value	error %	value	error %	value	error %
Fe$_3$O$_4$/MWNTs	15.14	5.139	2333	5.757	1.374E-5	5.14
Pd/MWNTs	19.61	11.42	1.859E4	12.08	3.209E-6	8.506
FePd-Fe$_2$O$_3$(3:10)/MWNTs	24.63	10.82	2010	9.599	3.83E-6	10.66
FePd-Fe$_3$C/MWNTs	26.4	5.031	405.2	5.681	2.207E-5	7.824
FePd-Fe$_2$O$_3$(3:5)/MWNTs	19.86	4.096	281.5	4.786	3.606E-5	6.6

times smaller than that of Pd/MWNTs, which suggests a big enhancement of the activity due to the formed FePd and Fe_2O_3. However, the R_{ct} value further decreases with decreasing the $Fe(CO)_5$ precursor dosage as indicated by FePd-Fe_3C/MWNTs and FePd-Fe_2O_3(3:5)/MWNTs due to the improved conductivity by decreasing Fe amount. The lowest R_{ct} value of FePd-Fe_2O_3(3:5)/MWNTs is a strong evidence for the highest reaction rate and is also consistent with the CV and CA results, implying an optimal combination of catalytic FePd with Fe_2O_3 and MWNTs substrates in FePd-Fe_2O_3(3:5)/MWNTs.

3.4. Mechanism Discussions

3.4.1. Synthesis Mechanism

The formation process is schematically shown in Scheme 3.1, the decomposition of $Fe(CO)_5$ and $Pd(acac)_2$ has been reported previously with the production of Fe and Pd atoms.[65] [66] The alloying process of FePd will proceed when they meet together in the high temperature environment, simultaneously, excessive Fe atoms will anchor on the tube wall surface through interacting with C=O part and the Fe_2O_3 molecules are finally obtained in the ambient atmosphere. The Fe_2O_3 molecules continue to deposit around the Fe_2O_3 nuclei and finally form the Fe_2O_3 NPs. In addition, the formed FePd NPs intend to deposit on the Fe_2O_3 surface due to the relatively lower bonding energy with Fe_2O_3 compared with that of MWNTs. However, Fe_3C is obtained as the decomposed Fe atoms react with C due to the relatively small amount of $Fe(CO)_5$ precursor dosage.

3.4.2. Improved Catalytic Mechanism Discussion

The alloying effect of Pd with Fe is similar to the well-known bifunctional mechanism of Pt-Ru. Since the electronegativity of Fe (1.83) is much lower than Pd (2.20),[67] the alloying of Fe can modify the Pd electronic properties as the electrons will transfer from Fe to Pd and contribute to the d-band hybridization of Pd and Fe. The downward shift of d band center relative to the Fermi
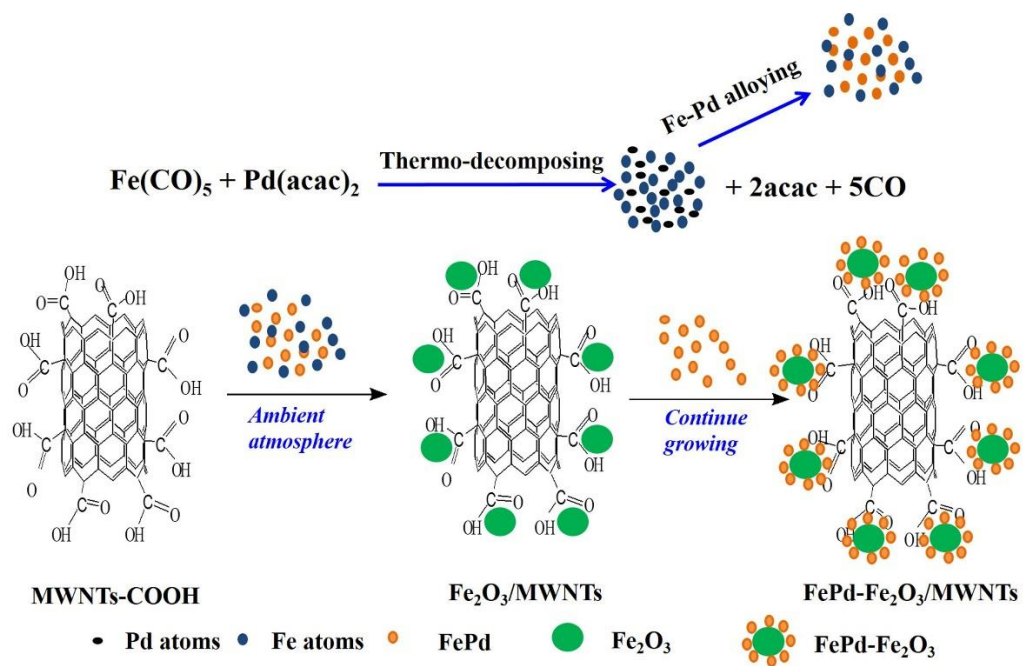
Scheme 3.1. A schematic representation for the synthesis of FePd-Fe₂O₃/MWNTs nanocatalysts.

level would increase the surface reactivity, thus enhancing the adsorption of OH_{ads} species on the Pd surface and greatly facilitate the process of EOR. In addition, compared to fcc Pd, the slight shift of diffraction peaks of the FePd phase indicates a lattice contraction of Pd-Pd bond distance, and this strain effect can greatly lower the carbonaceous accumulation thus making the electrode more tolerant towards CO poisoning as confirmed by the CA test.[68] Furthermore, the effect of Fe_2O_3 should also be taken into consideration. Numerous reports have emphasized that the activity and stability of electrocatalysts for alcohol oxidation in alkaline media have been improved by combining catalytic Pd with metal oxides, for example, NiO, CeO_2, Co_3O_4, and Mn_3O_4. It has been proposed that the oxygen-containing species could form more easily on the surface of metal oxides during the alcohol oxidation reaction.[69] The buffer effect can lead to the subsequent reaction of Pd with CO-like intermediate species more easily, the produced CO_2 or other dissolvable products will also release the active sites for further electrochemical reaction, thus enhancing the oxidation efficiency.[70] Therefore, it is reasonable that the Fe_2O_3 substrate will have a positive effect on the electrocatalytic FePd NPs. However, excess amount of Fe_2O_3 amount can largely decrease the electrocatalytic activity due to its poor conductivity, which has been demonstrated by the decreased j_p value and deteriorated tolerance stability in FePd-Fe_2O_3(3:10)/MWNTs. Therefore, there is an appropriate amount of Fe_2O_3 for the greatest enhancement of the electrocatalytic activity of the present FePd NPs. In summary, the highest electrocatalytic activity of FePd-Fe_2O_3(3:5)/MWNTs toward EOR is due to the optimal combination of promoter Fe_2O_3 with MWNTs substrate and the enhanced FePd surface reactivity.

3.5. Conclusions

Highly catalytic active and magnetic FePd-Fe_2O_3/MWNTs nanocatalysts as ultrafine FePd alloy NPs deposited on Fe_2O_3 NPs were further evenly distributed on MWNTs have been

successfully prepared by simple thermal decomposing $Pd(acac)_2$ and $Fe(CO)_5$ in a refluxing dimethylformamide (DMF) solution in the presence of MWNTs-COOH. The formation of FePd alloy is confirmed by the crystalline structures and composition investigation through XRD and XPS spectra. A unique structure as FePd NPs first deposited on Fe_2O_3 NPs which were further uniformly dispersed on MWNTs was disclosed by TEM. Electro-characterizations as CV, CA and EIS demonstrated an enhanced catalytic performance of FePd-Fe_2O_3/MWNTs nanocatlysts towards EOR compared with Pd/MWNTs. Modified electronic properties of Pd by Fe, easily proceeded poisoning species on Fe_2O_3 and the optimal combination of promoter Fe_2O_3 and MWNTs substrate are mainly account for the greatly enhanced activity. This simple method is of great significance for the facile preparation of magnetic Pd catalysts with excellent catalytic activity.

3.6. References

1. J. Liu, X. Peng, W. Sun, Y. Zhao and C. Xia, *Organic Letters*, 2008, **10**, 3933-3936.
2. F. J. Urbano and J. M. Marinas, *Journal of Molecular Catalysis A: Chemical*, 2001, **173**, 329-345.
3. D. Guin, B. Baruwati and S. V. Manorama, *Organic Letters*, 2007, **9**, 1419-1421.
4. X. Pan, Z. Fan, W. Chen, Y. Ding, H. Luo and X. Bao, *Nature materials*, 2007, **6**, 507-511.
5. G. Postole, B. Bonnetot, A. Gervasini, C. Guimon, A. Auroux, N. I. Ionescu and M. Caldararu, *Applied Catalysis A: General*, 2007, **316**, 250-258.
6. M. Skotak, Z. Karpiński, W. Juszczyk, J. Pielaszek, L. Kępiński, D. V. Kazachkin, V. I. Kovalchuk and J. L. d'Itri, *Journal of Catalysis*, 2004, **227**, 11-25.
7. M. Haneda, Y. Kintaichi, I. Nakamura, T. Fujitani and H. Hamada, *Journal of Catalysis*, 2003, **218**, 405-410.
8. Y. S. Li, T. S. Zhao and Z. X. Liang, *Journal of Power Sources*, 2009, **187**, 387-392.
9. F. Vigier, C. Coutanceau, A. Perrard, E. M. Belgsir and C. Lamy, *Journal of Applied Electrochemistry*, 2004, **34**, 439-446.
10. C. W. Xu, H. Wang, P. K. Shen and S. P. Jiang, *Advanced Materials*, 2007, **19**, 4256-4259.
11. H. Meng, S. Sun, J.-P. Masse and J.-P. Dodelet, *Chemistry of Materials*, 2008, **20**, 6998-7002.
12. F. Hu, X. Cui and W. Chen, *The Journal of Physical Chemistry C*, 2010, **114**, 20284-20289.
13. C. Xu, L. Cheng, P. Shen and Y. Liu, *Electrochemistry Communications*, 2007, **9**, 997-1001.
14. C. Zhu, S. Guo and S. Dong, *Advanced Materials*, 2012, **24**, 2326-2331.
15. Y. Wang, Q. He, J. Guo, H. Wei, K. Ding, H. Lin, S. Bhana, X. Huang, Z. Luo, T. D. Shen, S. Wei and Z. Guo, *ChemElectroChem*, 2015, DOI: 10.1002/celc.201402378, n/a-n/a.
16. X. Chen, G. Wu, J. Chen, X. Chen, Z. Xie and X. Wang, *Journal of the American Chemical Society*, 2011, **133**, 3693-3695.
17. S. U. Son, Y. Jang, K. Y. Yoon, E. Kang and T. Hyeon, *Nano Letters*, 2004, **4**, 1147-1151.
18. V. Mazumder and S. Sun, *Journal of the American Chemical Society*, 2009, **131**, 4588-4589.
19. N. R. Jana, Z. L. Wang and T. Pal, *Langmuir*, 2000, **16**, 2457-2463.
20. J. L. Fernández, D. A. Walsh and A. J. Bard, *Journal of the American Chemical Society*, 2004, **127**, 357-365.
21. Z. Zhang, J. Ge, L. Ma, J. Liao, T. Lu and W. Xing, *Fuel Cells*, 2009, **9**, 114-120.
22. W. Wang, D. Zheng, C. Du, Z. Zou, X. Zhang, B. Xia, H. Yang and D. L. Akins, *Journal of Power Sources*, 2007, **167**, 243-249.
23. L. Chen, H. Guo, T. Fujita, A. Hirata, W. Zhang, A. Inoue and M. Chen, *Advanced Functional Materials*, 2011, **21**, 4364-4370.
24. F. Cheng, X. Dai, H. Wang, S. P. Jiang, M. Zhang and C. Xu, *Electrochimica Acta*, 2010, **55**, 2295-2298.
25. J. Yang, W. Zhou, C. H. Cheng, J. Y. Lee and Z. Liu, *ACS Applied Materials & Interfaces*, 2009, **2**, 119-126.
26. W. Li and P. Haldar, *Electrochemistry Communications*, 2009, **11**, 1195-1198.
27. W. Wang, R. Wang, S. Ji, H. Feng, H. Wang and Z. Lei, *Journal of Power Sources*, 2010, **195**, 3498-3503.

28. Z. Zhang, K. L. More, K. Sun, Z. Wu and W. Li, *Chemistry of Materials*, 2011, **23**, 1570-1577.
29. S. Guo, S. Zhang, X. Sun and S. Sun, *Journal of the American Chemical Society*, 2011, **133**, 15354-15357.
30. A. Kolmakov, D. O. Klenov, Y. Lilach, S. Stemmer and M. Moskovits, *Nano Letters*, 2005, **5**, 667-673.
31. M. Ye, J. Gong, Y. Lai, C. Lin and Z. Lin, *Journal of the American Chemical Society*, 2012, **134**, 15720-15723.
32. H. T. Tan, Y. Chen, C. Zhou, X. Jia, J. Zhu, J. Chen, X. Rui, Q. Yan and Y. Yang, *Applied Catalysis B: Environmental*, 2012, **119–120**, 166-174.
33. Y. Jiao, H. Jiang and F. Chen, *ACS Catalysis*, 2014, **4**, 2249-2257.
34. S. Chen, R. Si, E. Taylor, J. Janzen and J. Chen, *The Journal of Physical Chemistry C*, 2012, **116**, 12969-12976.
35. C. Xu, Z. Tian, P. Shen and S. P. Jiang, *Electrochimica Acta*, 2008, **53**, 2610-2618.
36. H. Itoh and T. Sugimoto, *J. Colloid Interface Sci.*, 2003, **265**, 283-295.
37. J. P. Cheng, J. Yu, D. Shi, D. S. Wang, Y. F. Liu, F. Liu, X. B. Zhang and J. G. Li, *Appl. Phys. A*, 2012, **106**, 837-842.
38. Q. He, T. Yuan, S. Wei, N. Haldolaarachchige, Z. Luo, D. P. Young, A. Khasanov and Z. Guo, *Angewandte Chemie*, 2012, **124**, 8972-8975.
39. B. Astinchap, R. Moradian, A. Ardu, C. Cannas, G. Varvaro and A. Capobianchi, *Chemistry of Materials*, 2012, **24**, 3393-3400.
40. Q. He, T. Yuan, X. Zhang, X. Yan, J. Guo, D. Ding, M. A. Khan, D. P. Young, A. Khasanov, Z. Luo, J. Liu, T. D. Shen, X. Liu, S. Wei and Z. Guo, *The Journal of Physical Chemistry C*, 2014, **118**, 24784-24796.
41. C. T. Wu, K. M. K. Yu, F. Liao, N. Young, P. Nellist, A. Dent, A. Kroner and S. C. E. Tsang, *Nature communications*, 2012, **3**, 1050.
42. R. N. Singh and R. Awasthi, *Catalysis Science & Technology*, 2011, **1**, 778-783.
43. J. Yang, C. Tian, L. Wang and H. Fu, *Journal of Materials Chemistry*, 2011, **21**, 3384-3390.
44. Q. Guo, D. Liu, J. Huang, H. Hou and T. You, *Microchimica Acta*, 2014, 1-7.
45. U. Schlotterbeck, C. Aymonier, R. Thomann, H. Hofmeister, M. Tromp, W. Richtering and S. Mecking, *Advanced Functional Materials*, 2004, **14**, 999-1004.
46. X. Guo, P. Brault, G. Zhi, A. Caillard, G. Jin and X. Guo, *The Journal of Physical Chemistry C*, 2011, **115**, 24164-24171.
47. K. Sato, A. Kovács and Y. Hirotsu, *Thin Solid Films*, 2011, **519**, 3305-3311.
48. I. Castellanos-Rubio, M. Insausti, I. G. de Muro, D. C. Arias-Duque, J. Hernández-Garrido, T. Rojo and L. Lezama, *J Nanopart Res*, 2015, **17**, 1-13.
49. X. Zhang, P. Zhang, H. Yu, Z. Ma and S. Zhou, *Catal Lett*, 2015, **145**, 784-793.
50. J. Zhu, S. Wei, H. Gu, S. B. Rapole, Q. Wang, Z. Luo, N. Haldolaarachchige, D. P. Young and Z. Guo, *Environ. Sci. Technol.*, 2012, **46**, 977-985.
51. J. Y. Kim, K. Park, S. Y. Bae, G. C. Kim, S. Lee and H. C. Choi, *Journal of Materials Chemistry*, 2011, **21**, 5999-6005.
52. S. Bhuvaneswari, P. M. Pratheeksha, S. Anandan, D. Rangappa, R. Gopalan and T. N. Rao, *Physical Chemistry Chemical Physics*, 2014, **16**, 5284-5294.
53. Q. Han, Liu, Xu, Chen, Wang and H. Zhang, *The Journal of Physical Chemistry C*, 2007, **111**, 5034-5038.

54.   J. Lu, X. Jiao, D. Chen and W. Li, *The Journal of Physical Chemistry C*, 2009, **113**, 4012-4017.

55.   I. T. Kim, G. A. Nunnery, K. Jacob, J. Schwartz, X. Liu and R. Tannenbaum, *The Journal of Physical Chemistry C*, 2010, **114**, 6944-6951.

56.   T. Pillo, R. Zimmermann, P. Steiner and S. Hüfner, *Journal of Physics: Condensed Matter*, 1997, **9**, 3987.

57.   K. Noack, H. Zbinden and R. Schlögl, *Catal Lett*, 1990, **4**, 145-155.

58.   S. L. Zhang and J. R. Zhang, *physica status solidi (b)*, 1994, **182**, 421-427.

59.   M. P. Felicissimo, O. N. Martyanov, T. Risse and H. J. Freund, *Surface Science*, 2007, **601**, 2105-2116.

60.   C. Du, M. Chen, W. Wang and G. Yin, *ACS Applied Materials & Interfaces*, 2010, **3**, 105-109.

61.   H. Huang and X. Wang, *Journal of Materials Chemistry*, 2012, **22**, 22533-22541.

62.   Y. Wang, Q. He, K. Ding, H. Wei, J. Guo, Q. Wang, R. O'Connor, X. Huang, Z. Luo, T. D. Shen, S. Wei and Z. Guo, *Journal of The Electrochemical Society*, 2015, **162**, F755-F763.

63.   J. Wang, H. Zhou, D. Fan, D. Zhao and C. Xu, *Microchim Acta*, 2015, **182**, 1055-1061.

64.   J. J. Wang, G. P. Yin, J. Zhang, Z. B. Wang and Y. Z. Gao, *Electrochimica Acta*, 2007, **52**, 7042-7050.

65.   P. Wang, B. Lai, H. Li and Z. Du, *Bioresource Technology*, 2013, **134**, 30-35.

66.   J. Wang, R. E. Winans, S. L. Anderson, S. Seifert, B. Lee, P. J. Chupas, Y. Ren, S. Lee and Y. Liu, *The Journal of Physical Chemistry C*, 2013, **117**, 22627-22635.

67.   F. Liao, T. W. B. Lo, D. Sexton, J. Qu, C.-T. Wu and S. C. E. Tsang, *Catalysis Science & Technology*, 2015, **5**, 887-896.

68.   I. Matanović, F. H. Garzon and N. J. Henson, *The Journal of Physical Chemistry C*, 2011, **115**, 10640-10650.

69.   C. Xu, P. k. Shen and Y. Liu, *Journal of Power Sources*, 2007, **164**, 527-531.

70.   Z. Wen, S. Yang, Y. Liang, W. He, H. Tong, L. Hao, X. Zhang and Q. Song, *Electrochimica Acta*, 2010, **56**, 139-144.

Appendix A

for

Chapter 3 Ultrafine FePd Nanoalloys Decorated Multiwalled Cabon Nanotubes toward

Enhanced Ethanol Oxidation Reaction
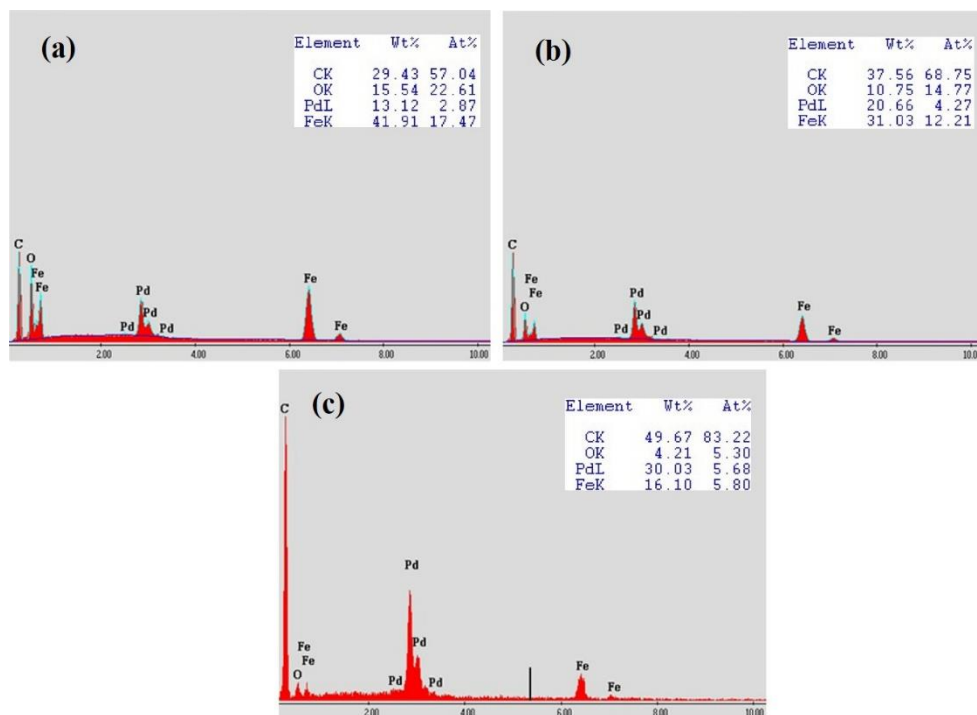
Figure A3.11. Energy dispersive spectroscopy (EDS) of (a) FePd-Fe$_2$O$_3$(3:10)/MWNTs, (b) FePd-Fe$_2$O$_3$(3:5)/MWNTs and (c) FePd-Fe$_3$C/MWNTs.

The high resolution of Fe 2p in (a) Fe$_3$O$_4$/MWNTs, (b) Pd-Fe$_2$O$_3$(3:10)/MWNTs, (c) FePd-Fe$_2$O$_3$(3:5)/MWNTs and (e) FePd-Fe$_3$C/MWNTs are shown in Figure A3.12(A). No satellite peak around 718 eV is observed in Fe$_3$O$_4$/MWNTs, different from that in Pd-Fe$_2$O$_3$(3:10)/MWNTs and FePd-Fe$_2$O$_3$(3:5)/MWNTs, indicating different iron existence forms. The curve fittings of Pd 3d of (a) Pd-Fe$_2$O$_3$(3:10)/MWNTs and (b) FePd-Fe$_3$C/MWNTs are also provided in Figure A3.12 (B), only two peaks similar to that of Pd-Fe$_2$O$_3$(3:5)/MWNTs are observed indicating the formation of PdFe alloy.
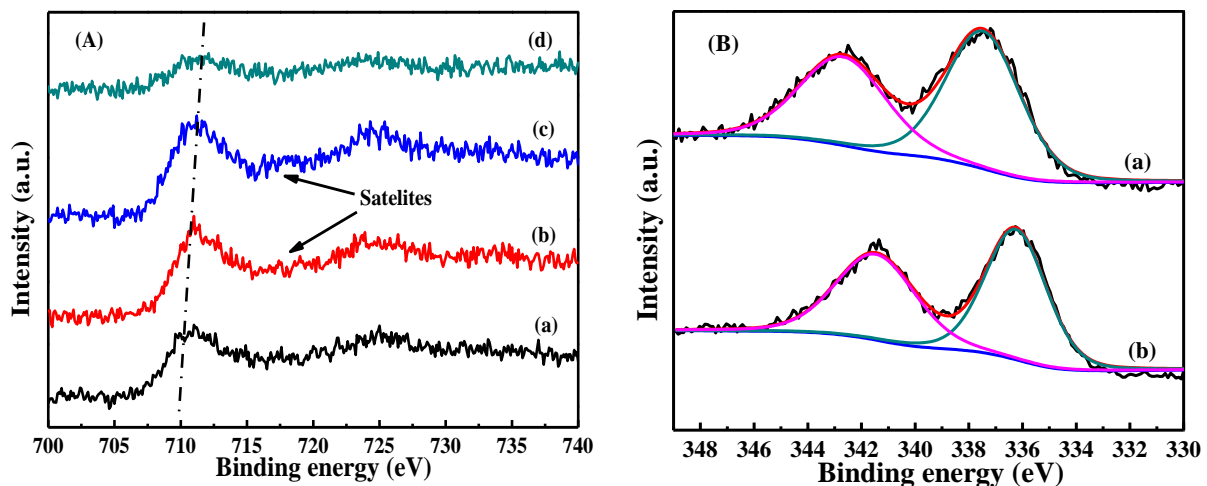
Figure A3.12. (A) XPS of Fe 2p as (a) Fe_3O_4/MWNTs, (b) Pd-Fe_2O_3(3:10)/MWNTs, (c) FePd-Fe_2O_3(3:5)/MWNTs and (d) FePd-Fe_3C/MWNTs, (B) curve fittings of Pd 3d in (a) Pd-Fe_2O_3(3:10)/MWNTs and (b) FePd-Fe_3C/MWNTs

Chapter 4 Electropolymerized Polyaniline/Manganese Iron Oxide

Hybrids with Enhanced Color Switching Response and

Electrochemical Energy Storage

This chapter is revised based on a paper first authored by myself.

My priority contribution to this paper include (i) development of the problem into a work, (ii) identification of the study area and objectives, (iii) design and conducting of the experiment, (iv) gathering and rendering literature, (v) processing and analysis the experimental data, (vi) pulling various contributions into a single paper. (vii) writing the paper.

Abstract

Polyaniline (PANI) nanocomposites embedded with manganese iron oxide ($MnFe_2O_4$) nanoparticles were prepared as thin films by electropolymerizing aniline monomers onto indium tin oxide (ITO) glass slides pre-spin-coated with $MnFe_2O_4$ nanoparticles. The shift of the characteristic peaks of PANI/$MnFe_2O_4$ in UV-visible absorption spectra and fourier transform infrared spectroscopy (FT-IR) indicate a formation of composites film and a chemical interaction between the PANI matrix and $MnFe_2O_4$ particles, which is also confirmed by the SEM images. A coloration efficiency of 92.31 cm^2 C^{-1} was obtained for the PANI/$MnFe_2O_4$ nanocomposites film, higher than that of the pristine PANI film, 80.13 cm^2 C^{-1}, suggesting a synergistic effect between the $MnFe_2O_4$ particles and the PANI matrix. An enhanced areal capacitance as 4.46 mF cm^{-2} was also achieved in the PANI/$MnFe_2O_4$ nanocomposites film compared with that of 3.95 mF cm^{-2} in the pristine PANI film from the CV at a scan rate of 5 mV s^{-1}. The enhanced performance of the composite films are attributed to the pseudocapacitive property of $MnFe_2O_4$ and the rougher morphology caused by the embedment of $MnFe_2O_4$ particles into the PANI matrix. Finally, the

sulfuric acid (H_2SO_4) concentration and temperature effects on the supercapative behavior of the pristine PANI and its $MnFe_2O_4$ nanocomposites films were studied, suggesting positive effects of decreasing H_2SO_4 concentration and increasing temperature during a low temperature range, relative higher temperatures can destroy the PANI structure and cause the degradation of PANI.

4.1. Introduction

As a promising type of sustainable and renewable energy storage device, electrochemical capacitors have merits such as long cycle life, lower maintenance cost and environmental friendliness.[1, 2] They have been widely applied in portable electronics, hybrid electric vehicles, memory backup systems, and large industrial equipment.[3-5] The high power density vs. batteries and the high energy density vs. conventional capacitors enable electrochemical capacitors a good choice to fill in the gap between the batteries and the conventional electrostatic capacitors.[6, 7] Electrochemical capacitors are classified into two categories based on different charge storage mechanisms, i.e., (i) electric double layer capacitors (EDLCs), which proceed through a non-Faradic process based on the ion adsorption between the interfaces of electrodes and electrolyte; and (ii) pseudocapacitors employing a Faradic process that stores energy through fast surface redox reaction.[8] Even though the carbon materials are usually employed as EDLCs electrodes due to their long cycle life ($> 10^5$ cycles), the applications is largely restricted by their low energy densities.[9] Pseudocapacitors based on redox reactions of metal oxides and conducting polymer materials are emerging as more competitive due to the higher specific capacitance.[10-12]

Conducting polymers have received dramatic research interests in pseudocapacitors due to several beneficial characteristics including tunable electrical properties, flexibility, and high processability from solution.[13, 14] Solution-processable conductive polymers have been widely investigated as electrode materials because of the facile inexpensive way to form thin-film electrodes, which offer tunable thickness, high conductivity, and excellent optical transparency and electrochromism.[15, 16] In particular, polyaniline (PANI) has attracted much more attention due to its relatively higher electrochemical and thermal stabilities, low cost, and high conductivity.[17-19] Specially, highly reversible pseudocapacitance arising from the versatile redox reactions and

97

corresponding color change make PANI a promising candidate for both electrochemical capacitors [20, 21] and electrochromic (EC) applications.[22, 23]

Nowadays, different PANI/metal oxide composites have been prepared and employed for various applications.[24] For example, PANI/BaTiO$_3$,[25] PANI/SnO$_2$,[26, 27] PANI/Co$_3$O$_4$,[28, 29] PANI/TiO$_2$,[30] PANI/V$_2$O$_5$[31] and PANI/WO$_3$[32, 33] have been investigated and they demonstrated improved magnetic, dielectric, humidity sensing, catalytic, electrochromic and supercapacitive properties. Furthermore, much work has been focused on spinel transition metal oxides (AB$_2$O$_4$) which contains two metal elements providing the feasibility to tune the energy density and working voltage by varying the metal content.[34] Among the AB$_2$O$_4$, manganese iron oxide (MnFe$_2$O$_4$) as a common ferrite material has been widely utilized in magnetic recording and microwave absorption fields.[35] MnFe$_2$O$_4$ was also reported as anode materials for supercapacitors.[36] Unfortunately, the supercapacitive performance of the MnFe$_2$O$_4$-based electrodes is not satisfying due to the high charge-transfer resistance originating from the poor electrical conductivity of MnFe$_2$O$_4$.[37, 38] The hybrid of conducive PANI with MnFe$_2$O$_4$ is anticipated to address this challenge and is promising for combined electrochromic and supercapacitive applications.

Different forms of materials have been employed to incorporate metal oxides into polymers to optimize properties in the synthesized nanocomposites.[39-42] Film as an efficient one can provide a two-dimensional (2D) nanostructure thus decreasing the diffusion path length of ions and lead to high charge/discharge rates.[43-46] Nowadays, the structure and composition of the electrodes as main factors affecting the performances of supercapacitor have been widely investigated.[47, 48] However, few studies have been conducted regarding the effects of operating conditions like electrolyte concentration and temperature, which are inevitable factors need to be considered during practical applications.[49-51] To the best of our knowledge, a comprehensive study of the

electrochemical and electrochromic properties as well as the electrolyte concentration and temperature effects on the supercapacitive behavior of the PANI/ $MnFe_2O_4$ nanocomposites film have not been studied yet.

In this work, the PANI/$MnFe_2O_4$ nanocomposites thin film was prepared by a facile combined spin coating and electropolymerization method, i.e., the aniline monomers in sulfuric acid solutions were electrodeposited onto $MnFe_2O_4$ coated indium tin oxide (ITO) glass slides, which were prepared by spin coating technique. Pristine PANI and pure $MnFe_2O_4$ films on the ITO glass were also synthesized using the same method as control experiments. The structure and morphology of the composites film were studied using fourier transform infrared spectroscopy (FT-IR) and scanning electron microscope (SEM). The optical properties, capacitive behaviors of the composites film were investigated using ultraviolet-visible (UV- visible) absorption spectra, spectroelectrochemistry (SEC), cyclic voltammetry (CV) and galvanostatic charge-discharge measurements. The electrolyte concentration and temperature effects on the supercapacitive behavior of the PANI/Mn_2FeO_4 nanocomposites film were investigated by varying the H_2SO_4 concentration from 0.5 to 2.0 M and applying different temperature as 2, 22 and 50 °C.

4.2. Experimental

4.2.1. Materials

Aniline (C_6H_7N, $\geqslant$99.0%), sulfuric acid (H_2SO_4, 95.0%-98.0%) and hydrogen peroxide solution (PERDROGEN® 30% H_2O_2 (w/w)), ethanol (HPLC, 99.8%), ammonium hydroxide (NH_4OH, 28.86 wt%) were all purchased from Fisher Scientific. Manganese iron oxide nanopowders ($MnFe_2O_4$, 99.99%, 28 nm, stock #: US 3912, CAS # 1344-43-0) were purchased from US Research Nanomaterials, Inc. The microscope glass slides and indium tin oxide (ITO) coated glass slides were obtained from Fisher and NanoSci Inc, respectively. Before the usage of

the ITO coated glass slides, they were first sonicated in ethanol for 10 min, and then immersed in an aqueous solution containing 4.0 mL NH_4OH, 4.0 mL H_2O_2 and 20.0 mL deionized water for 10 min. Finally, the ITO glasses were sonicated in deionized water for another 10 min and died naturally. Deionized water was used throughout the experiments.

4.2.2. Thin Film Electrode Preparation

For the synthesis of $MnFe_2O_4$ film, 1.0 mg Mn_2FeO_4 was dissolved in 10.0 mL ethanol solution under 30 min sonication. The $MnFe_2O_4$ film was prepared by drop casting about 1.0 mL $MnFe_2O_4$ suspension onto the ITO glass and maintained at 2000 rpm for 20 s. The film was dried naturally overnight. The electropolymerization of aniline onto the as-treated ITO glass or formed $MnFe_2O_4$ film was performed on an electrochemical working station VersaSTAT 4 potentiostat (Princeton Applied Research). A typical three electrode electrochemical cell was employed, in which a saturated calomel electrode (SCE) served as the reference electrode, a platinum (Pt) wire served as the counter electrode and the $MnFe_2O_4$ coated ITO glass or bare ITO glass slide with an effective area of 4.0 cm^2 served as the working electrode. A long path length home-made spectroelectrochemical cell with Teflon cell body with front and rear windows clapped with two steel plates was used when the ITO glass slide was used as the working electrode for optical characterizations. A typical electrochemical polymerization was performed 10 cycles scanned back and forth from 0 to +1.2 V vs. SCE at a scan rate of 50 mV/s in 0.5 M H_2SO_4 aqueous solution containing 0.1 M aniline.

4.2.3. Characterizations

The morphologies of the thin films grown on the ITO glass slides were characterized by scanning electron microscope (SEM, Hitachi S4300). The FT-IR spectrometer coupled with an ATR accessory (Bruker Inc. Vector 22) was used to characterize the surface functionality of the

thin films grown on the ITO glass slides in the range of 2000 to 500 cm^{-1} at a resolution of 4 cm^{-1}. The UV-visible spectra of the pristine PANI film and MnFe$_2$O$_4$-PANI hybrid film deposited on the ITO coated glass slide were observed in the range of 200-800 nm at room temperature using a UV-visible spectrophotometer (Jasco V-670 spectrophotometer and spectralon was used as a reference).

The electrochemical behaviors of pure Mn$_2$FeO$_4$ film, pristine PANI film, and PANI/ Mn$_2$FeO$_4$ nanocomposites film were investigated by CV scanned from -0.2 to 0.8 V vs. SCE at a series of scan rates and galvanostatic charge-discharge measurements with different current densities in 1.0 M H$_2$SO$_4$ aqueous solution. The electrochemical impedance spectroscopy (EIS) was carried out in the frequency range from 100, 000 to 0.01 Hz at a 5 mV amplitude referring to the open circuit potential (OCP). The spectroelectrochemistry measurements were performed on a Jasco V-670 spectrophotometer coupled with the potentiostat for applying electrochemical potentials. The *In situ* chronocoulometry (CC) were conducted under a square-wave voltage of 0.8 and -0.2 V with a pulse width of 20 s. The electrolyte concentration and temperature effects on the supercapacitive behaviors were investigated by varying the H$_2$SO$_4$ concentration from 0.5 to 2.0 M and applying different temperatures as 2, 22 and 50 °C using the same measurements as CV, galvanostatic charge-discharge and EIS.

4.3. Results and Discussion

4.3.1. Materials Characterization

The cyclic voltammogram (CV) curves obtained during the potentiodynamic electropolymerization growth of PANI onto the bare and MnFe$_2$O$_4$ coated ITO glass slides are shown in Figure B4.11(A&B). The pristine PANI and PANI/MnFe$_2$O$_4$ nanocomposites films are prepared by sweeping the potential between 0 and 1.2 V at a scan rate of 50 mV/s in 0.5 M H$_2$SO$_4$

solution containing 0.1 M aniline. The film growth can be verified by the monotonously increased current with increasing the CV cycle. Similar CV patterns except lower anodic current peaks are observed for the PANI/MnFe$_2$O$_4$ nanocomposites film growth, which is probably attributed to the increased resistance due to the introduction of MnFe$_2$O$_4$ film on the ITO glass slide. In addition, it is observed that the anodic irreversible peaks started at around + 0.9 V for both pristine PANI and PANI/MnFe$_2$O$_4$ nanocomposites films, which indicate the oxidation of aniline monomers and the initiation of the electropolymerization of PANI.[52]

The mass of monomers electropolymerized onto the substrate can be roughly estimated from the total Faradic charges consumed in the electropolymerization assuming an average of 2.5 electrons per aniline monomer in emeradine,[53, 54]

$$m = \frac{CM_m}{2.5F} \tag{1}$$

where m is the mass of PANI polymerized onto the substrate, gram (g); C is the total Faradic charges consumed in the electropolymerization, coulomb (C), M_m is the molecular mass of aniline monomers (93.13 g/mol), and F is Faraday constant (96485 C/mol). About 0.032 and 0.029 μg polymers were calculated for the pristine PANI film and PANI/MnFe$_2$O$_4$ nanocomposites film, respectively. The fewer amount of PANI in the PANI/MnFe$_2$O$_4$ nanocomposites film further confirms the increased resistance caused by the introduced MnFe$_2$O$_4$.

Figure 4.1(A) displays the FT-IR spectra of the pristine PANI and PANI/MnFe$_2$O$_4$ nanocomposites films in the region of 2000-500 cm^{-1}. For the pristine PANI thin film onto ITO, Figure (a), the peaks at 1559 and 1483 cm^{-1} correspond to the characteristic C=C stretching mode of the quinoid and benzenoid rings, respectively.[55] The peaks at 1299 and 1234 cm^{-1} are attributed to the C–N and C=N stretching mode.[56, 57] The peaks at 1126 and 796 cm^{-1} are assigned to the in-plane and out-of-plane bending of the C-H.[58, 59] For the PANI/MnFe$_2$O$_4$ nanocomposites film,

102

Figure (b), the characteristic peaks of PANI are mainly observed due to the dominant PANI. However, it is noticed that all the characteristic peaks corresponding to PANI in the PANI/MnFe$_2$O$_4$ nanocomposites film are shifting to higher wavenumbers compared with the pristine PANI film, indicating the interactions between MnFe$_2$O$_4$ and PANI due to the π-π stacking , electrostatic interactions as well as hydrogen bonding between MnFe$_2$O$_4$ and the -NH group of PANI.[60, 61]

Figure 4.1(B) represents the UV-visible spectra of the pure MnFe$_2$O$_4$, pristine PANI and MnFe$_2$O$_4$/PANI nanocomposites films in the wavelength range of 200-800 nm. The FT-IR spectrum of MnFe$_2$O$_4$ (Figure (a)) displays characteristic peaks of ferrite at around ~ 568 cm^{-1}, corresponding to the stretching vibration of tetrahedral group complexes.[41] For the pristine PANI films, Figure (b), two distinct absorption bands located at around 300 and 600 nm are assigned to the excitation of amine (π - π* electronic transition of benzenoid ring) and imine (electron transition from benzenoid to quinoid ring) of the polymer chains.[62, 63] Similar absorption spectrum is observed in the PANI/MnFe$_2$O$_4$ nanocomposites, Figure (c), implying a dominant role of PANI.[64] However, a considerable red shift from 253 to 267 nm with a higher intensity is observed in the MnFe$_2$O$_4$/PANI nanocomposites film due to the formed guest-host band between the -NH groups in PANI chains and O-metal part in MnFe$_2$O$_4$.[60]

The SEM characterization was also employed to investigate the morphology variation for the composites films. Figure 4.2(a-c) shows the SEM images of pure MnFe$_2$O$_4$, pristine PANI and MnFe$_2$O$_4$/PANI nanocomposites films deposited on ITO, respectively. For the pure MnFe$_2$O$_4$ film, Figure 4.2(a), MnFe$_2$O$_4$ particles exhibit a roughly spherical-like morphology on the ITO glass slide, confirming the successful spin coating of MnFe$_2$O$_4$ on the ITO glass. Figure 4.2(b) shows the SEM image of the pristine PANI film on the ITO coated glass slide, the short fiber-liked PANI
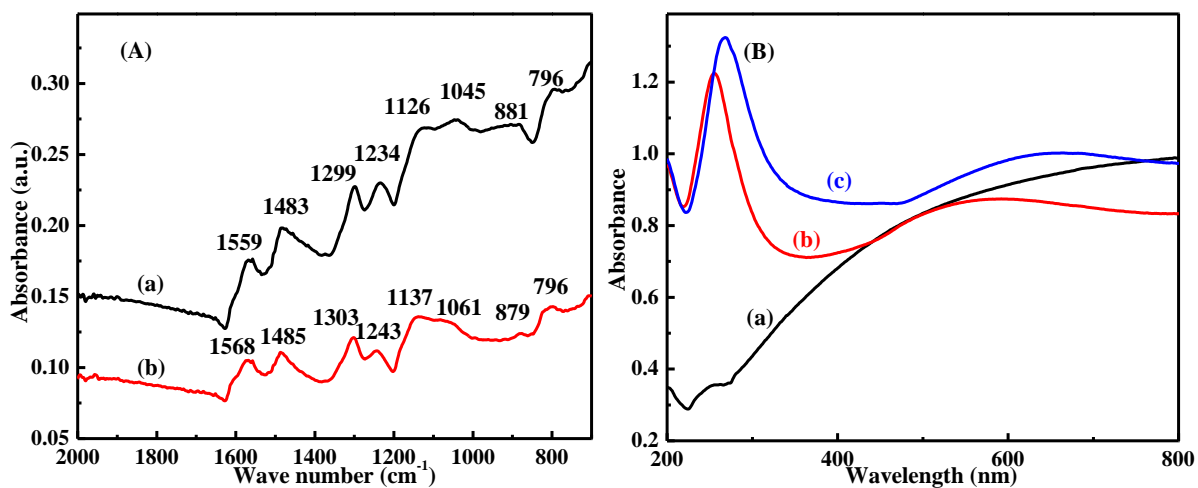
Figure 4.1. (A) FT-IR spectra of (a) pristine PANI film and (b) PANI/ MnFe₂O₄ nanocomposites film, (B) UV-visible absorption spectra of (a) pure MnFe₂O₄ film, (b) pristine PANI film, and (c) PANI/MnFe₂O₄ nanocomposites film, respectively.
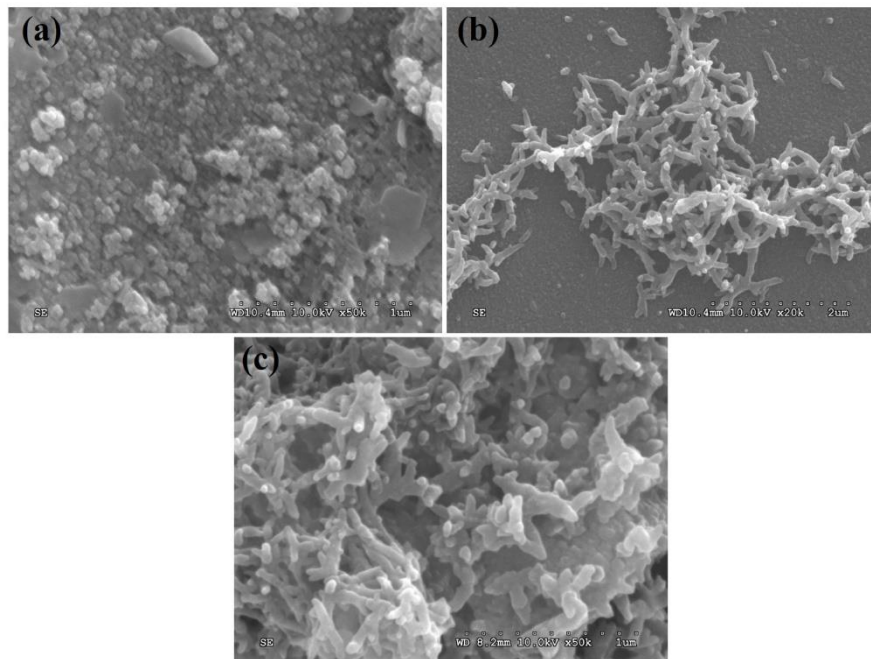
Figure 4.2. SEM images of (a) pure $MnFe_2O_4$ film, (b) pristine PANI film and (c) $MnFe_2O_4$/PANI nanocomposites film.

is successfully formed on the ITO glass slide through this electropolymerization method. For the PANI/MnFe$_2$O$_4$ nanocomposites film, Figure 4.2(c), the morphology of the film is roughly similar to that of pristine PANI, it is clearly seen that the PANI polymer is coated on the surface of MnFe$_2$O$_4$ particles during the *in-situ* polymerization process. A hydrogen bonding model has been employed to explain this wrap behavior of polymer on metal oxide.[65] PANI chains are first formed due to the inner hydrogen bonding which further lead to a PANI network structure, furthermore, the bonds between PANI and the oxygen atoms in MnFe$_2$O$_4$ also facilitate the embedment of the MnFe$_2$O$_4$ particles in the PANI matrix thus form a stable structure. This pattern has been confirmed by similar morphologies observed in the PANI/TiO$_2$, PANI/SnO$_2$ and PANI/Fe$_3$O$_4$ composites.[26, 66, 67]

4.3.2. Electrochromic Behaviors

Figure 4.3(a&b) shows the UV-Vis transmission spectra of the pristine PANI and PANI/MnFe$_2$O$_4$ nanocomposites films at different potentials in 1.0 M H$_2$SO$_4$, respectively. For both films from 0.8 to -0.2 V, similar UV-vis spectra are clearly observed as the transmittance decrease monotonously when increasing potential, indicating an increasingly oxidized PANI. Furthermore, the small absorbance band at around 700 nm is characteristic of the emeraldine base form of PANI due to the π- π* transition in the quinoid ring,[68] which implies the dominant role of PANI in the hybrid PANI/MnFe$_2$O$_4$ film. Correspondingly, varying colors of the nanocomposites film are obtained upon applying different potentials. Figure 4.4 shows the digital photograph of color switching at different potentials in 1.0 M H$_2$SO$_4$. The photos were taken after applying different potentials on the film for 20 s. The PANI/MnFe$_2$O$_4$ film displayed light yellow at -0.2 V (reduced state), light green at 0.5 V, blue at 0.8 V (partially oxidized state), and finally dark blue
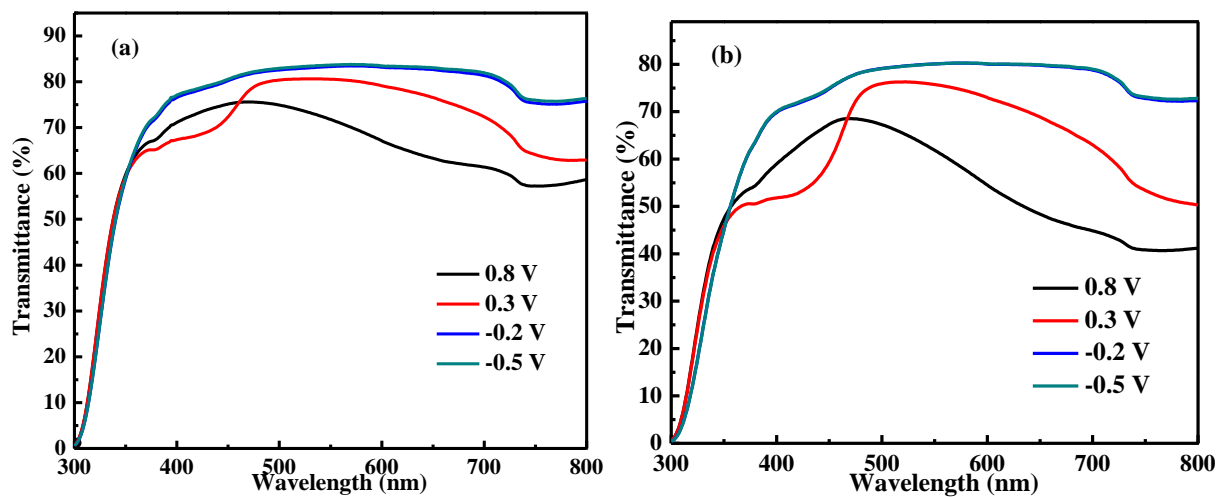
Figure 4.3. UV-Vis spectra of (a) pristine PANI film and (b) PANI/MnFe$_2$O$_4$ nanocomposites film onto ITO glass in 1.0 M H$_2$SO$_4$ aqueous solution at different potentials.
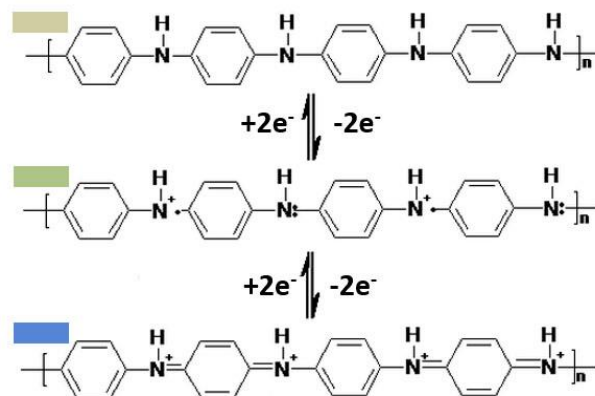
Figure 4.4. Digital photograph and corresponding mechanism of color switching of the PANI/MnFe$_2$O$_4$ nanocomposites film onto ITO at different potentials as -0.2, 0.5, 0.8 and 1.0 V in 1.0 M H$_2$SO$_4$.

at 1.0 V (fully oxidized state). The corresponding mechanism is also illustrated at the bottom of Figure 4.4.

The coloration switching responses of the pristine PANI and PANI/MnFe$_2$O$_4$ nanocomposites films are studied by applying potential steps of 0.8 and -0.2 V with a pulse width of 20 s. Figure 4.5(a-d) shows the transmittance-time (on the left) and the corresponding charge density-time curves (on the right) at 633 nm under an alternative square-wave voltage of 0.8 and -0.2 V. The transmittance modulations (transmittance difference at the bleached and colored states in the electrochromic materials) of 16.2 and 35.2% are calculated for the pristine PANI and PANI/MnFe$_2$O$_4$ nanocomposites films, respectively. The coloration time (τ_c) and bleaching time (τ_b) are defined as the time required for a 90% change in the full transmittance modulation, respectively.[69] For the pristine PANI film, Figure 4.5(a), τ_b is found to be 9.52 s and τ_c is 7.47 s from the cycles in the transmittance-time curve. However, it is obtained from Figure 4.5(c) that the PANI/MnFe$_2$O$_4$ nanocomposites film exhibits a much faster τ_b as 4.79 s and slight slow coloration time as 9.61 s than that of the pristine PANI film. Even though the composite film exhibits larger electrical resistance than pure PANI film due to the introduction of MnFe$_2$O$_4$, which might not be good for the redox reactions that give rise to the color switching. The faster switching response observed in the composite film can be explained by the differed morphology from that of pure PANI film, where in the former MnFe$_2$O$_4$ particles were embedded in the PANI matrix and facilitates the H$^+$ intercalation/deintercalation during the reactions; the unique donor-acceptor electronic structure occurring in the composite also contributes to a faster color switching.[70, 71]

Coloration efficiency (CE or η) is an important consideration of electrochromic materials for practical applications such as display and window devices. It is defined as the change in the optical
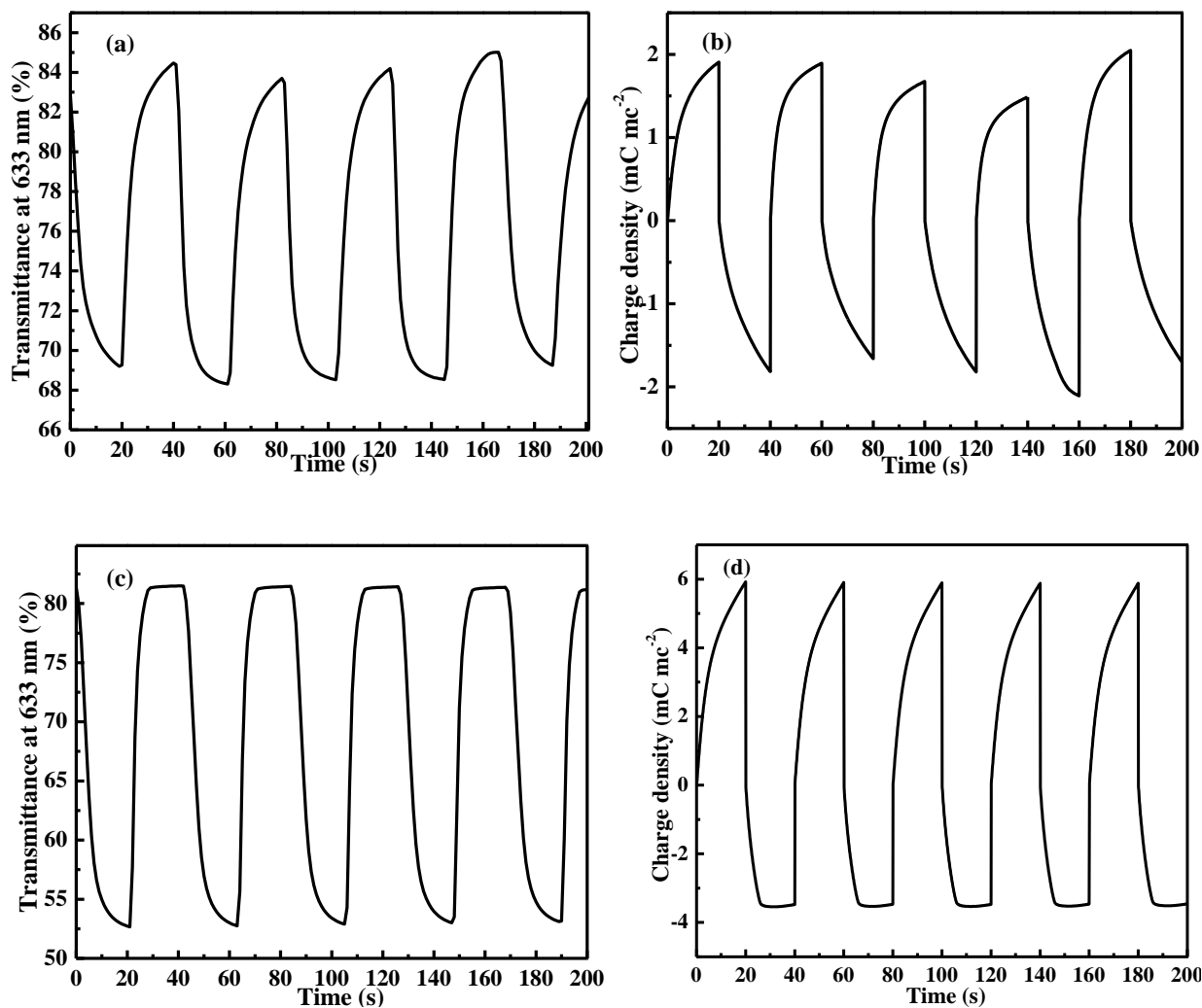
Figure 4.5. In situ transmittance and corresponding chronocoulometry of (a&b) pristine PANI and (c&d) PANI/MnFe$_2$O$_4$ nanocomposites films onto ITO glass at 633 nm in 1.0 M H$_2$SO$_4$ aqueous solution. The tests were conducted under a square-wave voltage of 0.8 and -0.2 V with a pulse width of 20 s.

density (OD) per unit charge (Q) inserted into (or extracted from) the electrochromic films, i.e., the amount of energy to affect a color change. The CE is calculated from Equation (2) and (3):[72]

$$\eta = \Delta OD(\lambda)/Q_d \tag{2}$$

$$\Delta OD = \log\left[T_{colored}/T_{bleached}\right] \tag{3}$$

where ΔOD is the change in the optical density, λ is the dominant wavelength for the material, Q_d is the charge density (injected/ejected charges per unit electrode area), $T_{bleached}$ refers to the aatransmittance of the film in the bleached state, and $T_{colored}$ refers to the varying transmittance of the film during the coloring process.[73] Figure 4.6 depicts the plots of the calculated ΔOD obtained from the second cycle in the transmittance-time curve at a wavelength of 633 nm, Figure 4.5(a&c), versus the corresponding inserted charge density obtained from charge density-time curve, Figure 4.5(b&d). The η is extracted as the slope of the line fitting to the linear region of the curve. The values of η are found to be 80.13 and 92.31 cm^2 C^{-1} for the pristine PANI film and the PANI/MnFe$_2$O$_4$ nanocomposites film, respectively. The enhanced CE for the nanocomposites film indicates an improved color switching response ability as fewer charges injected can contribute to greater optical density change than that of the pristine PANI film. The η value of PANI/MnFe$_2$O$_4$ nanocomposites film (92.31 cm^2 C^{-1}) is also comparable with a lot excellent reported films such as NiO microflake film (146.9 cm^2 C^{-1}),[74] WO$_3$/graphene film (96.1 cm^2 C^{-1}),[75] PANI/WO$_3$ film (98.4 cm^2 C^{-1})[73] and PEDOT: PSS/WO$_3$ film (117.7 cm^2 C^{-1}),[76] which enable it promising applications in EC devices. Finally, it is clearly seen that the transmittance vs. time and charge density vs. time curves of PANI/MnFe$_2$O$_4$ nanocomposites film are more stable than that of pristine PANI film, which further indicates a stabilizing role of the inner MnFe$_2$O$_4$ layer.
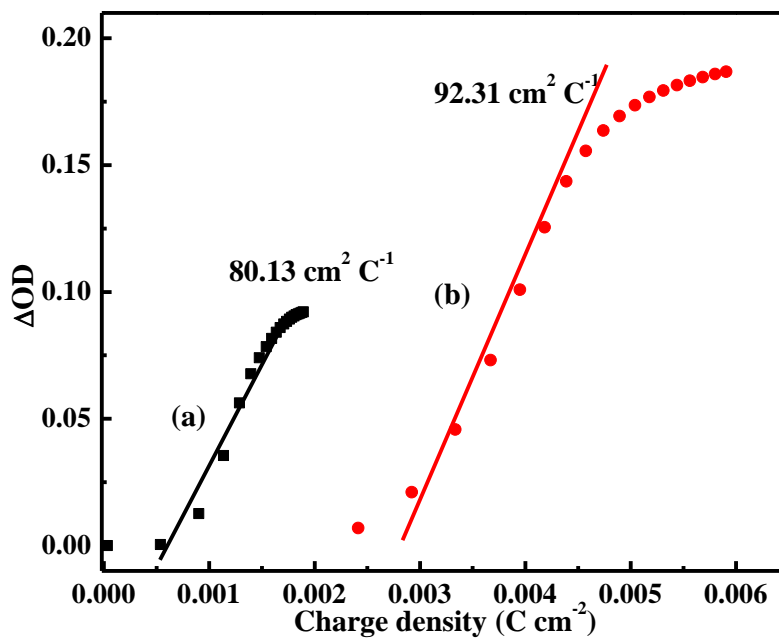
Figure 4.6. The plot of in situ optical density (ΔOD) versus charge density of (a) pristine PANI film and (b) PANI/MnFe$_2$O$_4$ nanocomposites film. The optical density was measured at 633 nm at 0.8 V in 1.0 M H$_2$SO$_4$ aqueous solution.

4.3.3. Capacitive Energy Storage Performances

Figure 4.7(a-c) depicts the CV curves of the pristine PANI, PANI/MnFe$_2$O$_4$ and MnFe$_2$O$_4$ films grown on the ITO coated glass slides in 1.0 M H$_2$SO$_4$ aqueous solution at a scan rate of 5 mV/s from -0.2 to 0.8 V. For the pristine PANI film, Figure 4.7(a), two typical redox pairs as A/A' at 0.16/-0.10 V corresponding to the transition between leucoemeraldine and emeraldine state of PANI, and B/B' at 0.58/0.40 V corresponding to the exchange between emeraldine and pernigraniline states are clearly observed, indicating the typical pesudocapacitance characteristics of PANI.[77, 78] For the PANI/MnFe$_2$O$_4$ nanocomposites film, Figure 4.7(b), the same characteristic peaks of PANI are also obtained due to the dominant PANI in the hybrid PANI/MnFe$_2$O$_4$ film. In addition, it is worth noting that the potential ranges between the typical redox peaks as A/A' and B/B' in the PANI/MnFe$_2$O$_4$ nanocomposites film are larger than that of the pristine PANI. The wide potential range implies harder oxidation/reduction processes in the hybrid PANI/MnFe$_2$O$_4$ film compared with that of pristine PANI film, which probably due to the increased resistance in the PANI/MnFe$_2$O$_4$ nanocomposites film. However, for the bare MnFe$_2$O$_4$ film in Figure 4.7(c), no obvious peaks are observed due to its small amount and negligible supercapacitive activity of MnFe$_2$O$_4$.

EIS as a powerful technique that gives a wealth of information regarding the internal resistance of the electrode materials as well as the resistance between the electrode and the electrolyte was also employed, Figure 4.8(a-c). The Nyquist plots of the pure MnFe$_2$O$_4$ film, pristine PANI film and PANI/MnFe$_2$O$_4$ nanocomposites film onto the ITO glass were conducted at OCP in the frequency range from 100 kHz to 0.01 Hz with ac-voltage amplitude of 5 mV, respectively. The Nyquist plot is divided into two regions as the high-frequency region and the low-frequency region. During the high-frequency range, the intercept of the curve with the real axis represents the equivalent series resistance (*ESR*), which mainly arises from the electrolyte
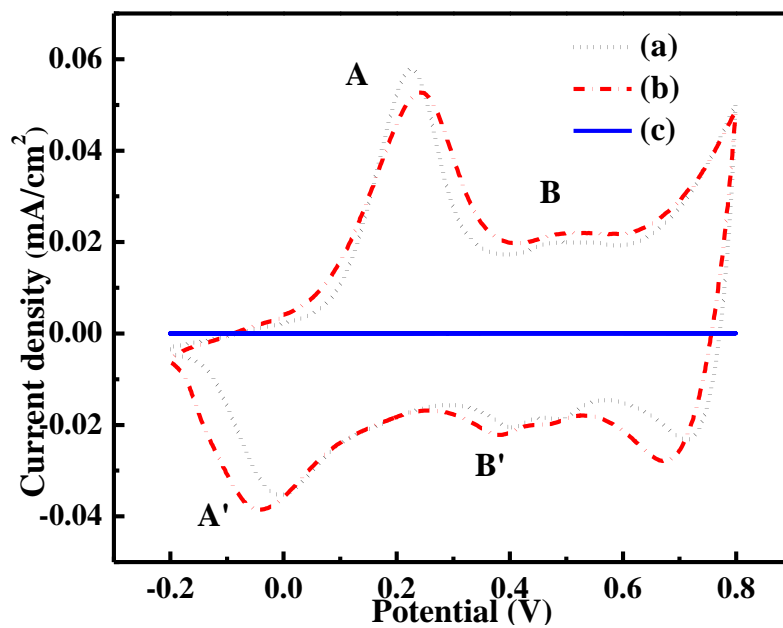
Figure 4.7. CV curves of (a) pristine PANI film, (b) PANI/MnFe$_2$O$_4$ nanocomposites film and (c) pure MnFe$_2$O$_4$ film onto ITO glass in 1.0 M H$_2$SO$_4$ at a scan rate of 5 mV/s.
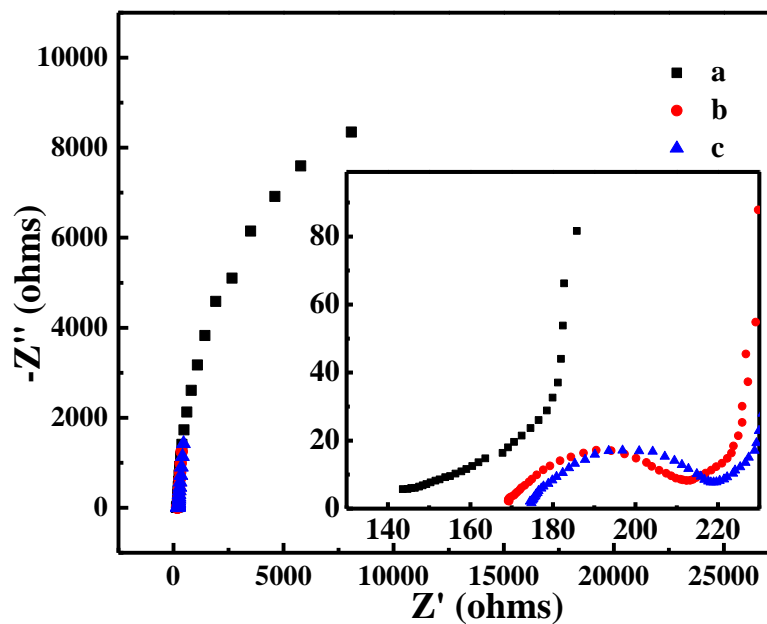
Figure 4.8. Electrochemical impedance spectroscopy (Nyquist plots) of (a) pure $MnFe_2O_4$ film, (b) pristine PANI film and (c) PANI/$MnFe_2O_4$ nanocomposites film onto ITO glass in 1.0 M H_2SO_4 with a frequency range from 100 kHz to 10 mHz using a perturbation amplitude of 5 mV at the open potential. Inset is the enlarged part of high frequency region.

resistance, the intrinsic resistance of the active material, and the contact resistance at the active material/current collector interface.[79] The *ESR* values are approximately 140, 170 and 176 Ω for the pure $MnFe_2O_4$, pristine PANI, and $PANI/MnFe_2O_4$ nanocomposites films, respectively. Even though the pure $MnFe_2O_4$ film exhibits the lowest *ESR* value due to the small amount of $MnFe_2O_4$, it displays much larger resistance throughout the whole frequency range. The increased *ESR* values observed for the pristine PANI and $PANI/MnFe_2O_4$ nanocomposites films are probably due to the added PANI material. In addition, the increased *ESR* value of the $PANI/MnFe_2O_4$ nanocomposites film compared with that of the pristine PANI film confirms again that the underlayered $MnFe_2O_4$ film has increased the total resistance. However, the almost overlap of the two lines in the low-frequency region implies an approximately equal migration of the ions regardless the effect of $MnFe_2O_4$. Another important parameter is the diameter of the semicircles in the high-frequency to mid-frequency region, which represents the charge transfer resistance (R_{ct}) between the electrode and the electrolyte interface. The observed equivalent semicircles for both the pristine PANI and $PANI/MnFe_2O_4$ indicate that the R_{ct} is mainly aroused from PANI in the $PANI/MnFe_2O_4$ nanocomposites film. Furthermore, for the pristine PANI and $PANI/MnFe_2O_4$ nanocomposites films, the slope of the straight lines are much sharper compared with that of the pure $MnFe_2O_4$ film, indicating ideal capacitive properties of these two.

The areal capacitance of the films, which is perceived as a better indicator to evaluate the performance of thin film-based supercapacitors for applications in small scale electronics and stationary energy storage devices,[80, 81] is calculated from the CV curves at different scan rates from -0.2 to 0.8 V in 1.0 M H_2SO_4 aqueous solution using Equation (4): [82]

$$C_s = \left(\int i dV \right) \big/ (2S \times \Delta V \times v)$$

(4)

where C_s is the areal capacitance in F cm^{-2}, $\int idV$ is the integrated area of the CV curve, S is the surface area of active materials in the single electrode in cm^2, ΔV is the scanned potential window in V, and ν is the scan rate in mV/s.

The CV curves (on the left) and corresponding capacitance dependence on the scan rate plots (on the right) of the pristine PANI and PANI/MnFe$_2$O$_4$ nanocomposites films are provided in Figure B4.12(a&b), respectively. It is clearly seen that the cathodic peaks shift negatively and the anodic peaks shift positively when increasing the scan rate from 5 to 100 mV/s, which probably due to the internal resistance of the electrode.[83] Both increased area capacitances with decreasing the scan rate are observed for the pristine PANI and PANI/MnFe$_2$O$_4$ nanocomposites films as indicated in the capacitance vs. scan rate plots. The linear increase in the capacitance with decreasing the scan rate suggests a good rate producing ability of these films.[84] The direct impact of increasing scan rate is on the diffusion of H$^+$ into the PANI matrix, the H$^+$ is unable to approach the inner surface of the electrode at higher scan rates and the materials deep within the pores contribute little to the reaction thus result in decreased capacitances. However, the relatively slow diffusion speeds at lower scan rates are able to ensure the ions in the electrolyte to diffuse near the electrode/electrolyte interface to get full access to the inner MnFe$_2$O$_4$ electrode materials and contribute to the increased capacitances. It is clear that the capacitances of the pristine PANI (2.38 and 3.13 mF cm^{-2}) are higher than that of the PANI/MnFe$_2$O$_4$ nanocomposites film (1.88 and 2.74 mF cm^{-2}) at higher scan rates such as 100 and 50 mV/s. Since the upper layer PANI largely contributes to the capacitance at higher scan rates, the larger PANI amount confirmed by CV synthesis results mainly accounts for the increased capacitance of the pristine PANI film. In contrast, the areal capacitances of the PANI/MnFe$_2$O$_4$ nanocomposites film are larger than that of the pristine PANI film (4.05 and 4.46 mF cm^{-2} vs. 3.87 and 3.95 mF cm^{-2} at 5 and 10 mV/s,

respectively). Since the MnFe$_2$O$_4$ particles are largely covered by PANI matrix, they are negligible in contributing to the capacitance at high scan rates. However, their capacitances will become increasingly exploited with decreasing the scan rate as more and more electrode materials will be accessible by the ions and contribute to increased capacitances.[85-87] The PANI/MnFe$_2$O$_4$ nanocomposites film retains 42.13 % of the capacitance at higher scan rate, compared to 69.3 % for the pristine PANI film, indicating a worse ion diffusion in the former at higher scan rates due to the inner layered MnFe$_2$O$_4$ film.

The galvanostatic charge-discharge measurements by chronopotentiometry (CP) are also carried out on the films in 1.0 M H$_2$SO$_4$ aqueous solution in order to evaluate the areal capacitance using Equation (5):[82]

$$C_s = (i \times t)/(S \times \Delta V)$$

(5)

where C_s is the areal capacitance in F cm^{-2}, i is the discharge current in A, t is the discharge time in s, S is the surface area of the active materials in the single electrode in cm^2, ΔV is the scanned potential window (excluding IR drop in the beginning of the discharge) in V.

Figure B4.13(a&b) shows the potential responses of the pristine PANI and PANI/MnFe$_2$O$_4$ nanocomposites films under different currents (on the left) and the corresponding plots of current density vs. areal capacitance (on the right). Typical pseudocapacitive galvanostatic charge/discharge curves are presented, which are not ideal straight lines, indicating that the reactions are faradic processes. In addition, the IR drop is found to decrease with decreasing the charge/discharge current density due to the increasingly exploited electrode. For the corresponding capacitance variation, the areal capacitance of each film is observed to increase with decreasing the current density due to the better ion diffusion and improved electrode access. Negligible capacitance difference between the two films is observed at 0.32 mA cm^{-2} due to the less deposited

PANI and the increased film resistance in PANI/MnFe$_2$O$_4$ nanocomposites film. The capacitances

of the PANI/MnFe$_2$O$_4$ nanocomposites film gradually exceed those of the pristine PANI film due

to the increasingly available MnFe$_2$O$_4$ layer at 0.04 and 0.08 mA cm^{-2}. It's noticeable that the areal

capacitance of the PANI/MnFe$_2$O$_4$ nanocomposites is enhanced to 4.10 mF cm^{-2} compared with

that of the pristine PANI film (3.67 mF cm^{-2}) at 0.04 mA cm^{-2}, which is also consistent with the

capacitance variation trend obtained from the CV results. Even though the capacitance of this

PANI/MnFe$_2$O$_4$ nanocomposites film can be directly enhanced through increasing PANI sweeping

cycles , the 10 cycles produced 4.10 mF cm^{-2} at 0.04 mA cm^{-2} is still comparable with a lot reported

values such as 5.83 mF cm^{-2} of CNFs/PANI/RGO film at 0.0043 mA cm^2,[88] 4.1 mF cm^{-2} of

PANI/WO$_3$ film at a current density of 0.02 mA cm^{-2} [89] and 6.3 mF cm^{-2} for PANI/GO film at 0.16

mA cm^{-2}.[90] However, the mass capacitance of this hybrid film can reach an extraordinary level (>

1000 mF/g) due to the ultra-small amount of active materials.

4.3.4. H$_2$SO$_4$ Concentration Effect on Electrochemical Behavior

The electrolyte, known as the ''blood'' for supercapacitors, plays an important role in

governing the rate capability and energy density of supercapacitors. Investigating the

concentration effect of H$_2$SO$_4$, a common electrolyte used in PANI-based supercapacitors, is of

great significance for practical usages.[91] Three concentrations as 0.5, 1.0 and 2.0 M are selected to

study the concentration effect on the pristine PANI and PANI/MnFe$_2$O$_4$ nanocomposites films.

Characterizations such as CV, galvanostatic charge-discharge and EIS are employed to investigate

the H$_2$SO$_4$ concentration effect on the supercapacitive behaviors, Figure 4.9. The CV curves of the

pristine PANI and PANI/MnFe$_2$O$_4$ nanocomposites film are conducted at 20 mV/s in the

corresponding electrolytes, Figure 4.9(a&b). Similar CV curves with a clear area decrease are

obtained, indicating the negative role of increasing the H$_2$SO$_4$ concentration on the capacitance,

the capacitances of PANI/MnFe$_2$O$_4$ nanocomposite film are calculated to decrease from 4.51, 4.23, to 3.76 mF cm^{-2} for 0.5, 1.0 and 2.0 M H$_2$SO$_4$, respectively. In addition, it is clearly seen from Figure 4.9(a&b) that the typical redox pair peaks shift widening the potential differences between the redox peaks, indicating a worse reversibility with increasing the H$_2$SO$_4$ concentration. Figure 4.9(c&d) depicts the galvanostatic charge-discharge curves of the pristine PANI and PANI/MnFe$_2$O$_4$ nanocomposites films at a current density of 0.08 mA cm^{-2}, respectively. Similar decreased discharging times are also observed for both films with increasing the H$_2$SO$_4$ concentration, which are consistent with the CV results. In addition, the increased IR drops observed in Figure 4.9(c&d) also suggest deteriorated performances which would be explained by the corresponding EIS Nyquist impedance plots, Figure 4.9(e&f), performed in the frequency range of 100, 000 to 0.01 Hz with a 5 mV amplitude referring to OCP. Similar curves are obtained for both PANI and PANI/MnFe$_2$O$_4$ films as small semicircles in the high frequency ranges and following tale in the low frequency ranges for all the H$_2$SO$_4$ concentrations. Same trends as decreased *ESR* and increased *R$_{ct}$* values are simultaneously observed for both films with increasing the H$_2$SO$_4$ concentration. Since electrolyte resistance is usually predominant in determining *ESR*,[92] it is deduced that the increasingly available H$^+$ ions would mainly account for the decreased *ESR* values. However, the increased *R$_{ct}$* values determined from the increased diameter of semicircles clearly indicate harder charge transfer processes with increasing the H$_2$SO$_4$ concentration which would mainly account for the deteriorated performances. Ion diffusion coefficient (D) was also calculated according to Equation A1 and provided in Figure B4.14 as 0.5 M (1.51×10^{-12} cm^2/s) > 1.0 M (3.29×10^{-13} cm^2/s) > 2.0 M (7.31×10^{-14} cm^2/s) for pristine PANI and 0.5 M (3.28×10^{-13} cm^2/s) > 1.0 M (9.51×10^{-14} cm^2/s) > 2.0 M (2.18×10^{-14} cm^2/s) for PANI/MnFe$_2$O$_4$ nanocomposites film, which is consistent with the CV and galvanostatic charge-discharge results.

Figure 4.9. H_2SO_4 effect (0.5, 1.0 and 2.0 M) on the supercapacitive behavior of pristine PANI film (a,c and e) and PANI/MnFe$_2$O$_4$ nanocomposites film (b, d, and f). (a&b), CV conducted at a scan rate of 20 mV/s from -0.2 - 0.8 V, (c&d) galvanostatic charge-discharge at current density of 0.08 mA cm^{-2}, (e&f), EIS performed from 100 kHz to 0.01 Hz with 5 mV amplitude at the open potential
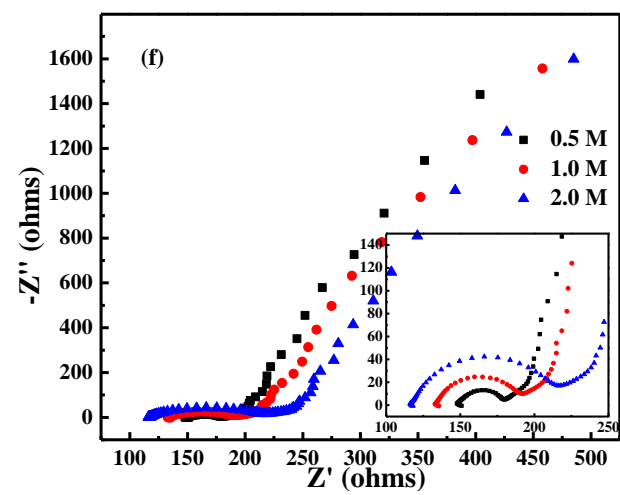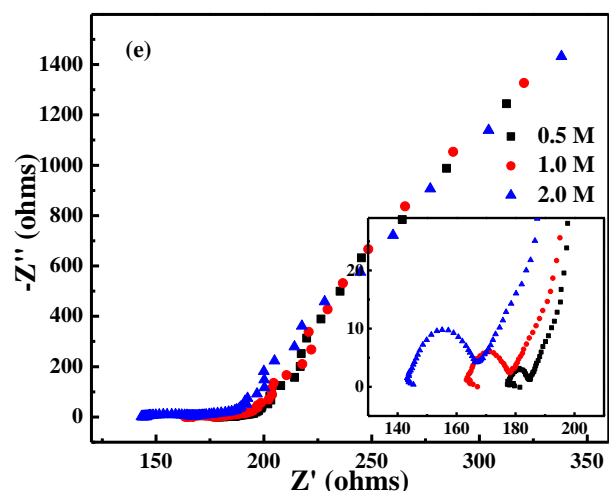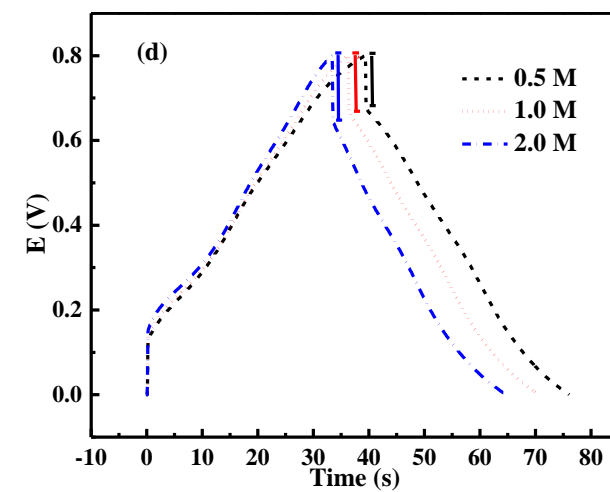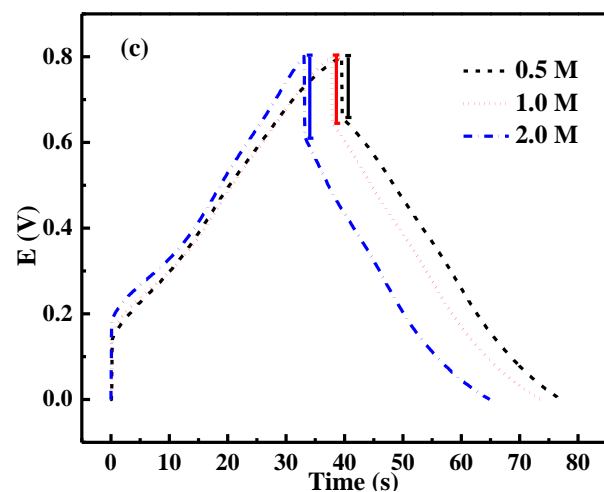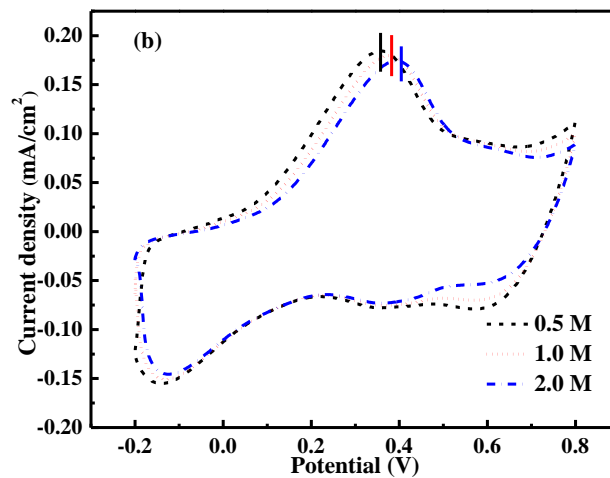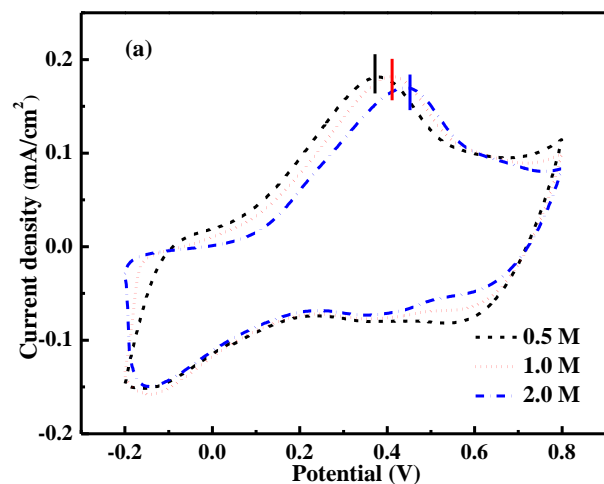
4.3.5. Temperature Effect on Electrochemical Behavior

According to the above experimental results, 0.5 M H_2SO_4 electrolyte was selected to study the effect of temperature on the supercapacitive properties of the pristine PANI and PANI/MnFe$_2$O$_4$ nanocomposites films. Three temperatures as 2, 22 and 50 ºC represent cold, normal, and hot weather were selected to evaluate the temperature effect using CV, galvanostatic charge-discharge, and EIS characterizations as the same logic. Figure 4.10(a-f) displays the CV, galvanostatic charge-discharge, and EIS characterizations of the pristine PANI film (a, c and e) and PANI/MnFe$_2$O$_4$ nanocomposites film (b, d and f), respectively. For the CV curves, Figure 4.10(a&b), they were conducted at a scan rate of 20 mV s^{-1} at different temperatures. The slight area increase is first observed for both the pristine PANI and PANI/MnFe$_2$O$_4$ films with increasing the temperature from 2 to 22 ºC, suggesting a positive role of temperature in enhancing the supercapacitive property due to the greatly enhanced ion mobility.[50, 51, 93] However, a clearly area decreases are following observed as the temperature increased to 50 ºC. The degradations of the pristine PANI and PANI/MnFe$_2$O$_4$ nanocomposites films at high temperatures are mainly responsible for the worse performance, which is demonstrated by the first 6 and 3 CV cycles at 50 ºC as shown in Figure B4.16(a&b). For the galvanostatic charge-discharge curves, Figure 4.10(c&d), similar trends to that of the CV results are observed, demonstrating that increasing temperature in the low temperature range can enhance the performance but the PANI structure will be destroyed when continue increasing to high temperature. In order to further investigate the operating temperature effect on the kinetics transfer process, EIS tests were performed at the open circuit condition in a frequency range from 100 kHz to 0.01 Hz with ac-voltage amplitude of 5 mV. It is clearly seen from Figure 4.10(e&f) that the *ESR* values of both the films follow an order as *ESR* (2 ºC) < *ESR* (22 ºC) due to the enhanced mobility of ions when increasing temperature,

Figure 4.10. Temperature effect (2, 22 and 50 ℃) on the supercapacitive behavior of pristine PANI film (a,c and e) and PANI/MnFe$_2$O$_4$ nanocomposites film (b, d, and f) in 0.5 M H$_2$SO$_4$. (a&b), CV conducted at a scan rate of 20 mV/s from -0.2-0.8 V. (c&d), galvanostatic charge-discharge curves with a current density of 0.08 mA cm^{-2}. (e&f), EIS performed from 100 kHz to 0.01 Hz with an amplitude of 5 mV at the open potential.
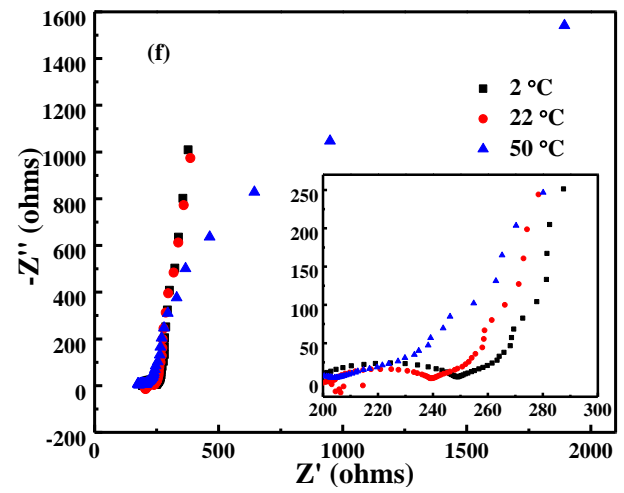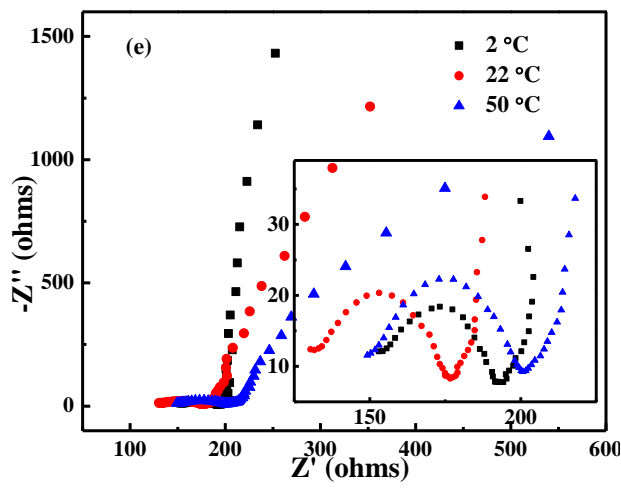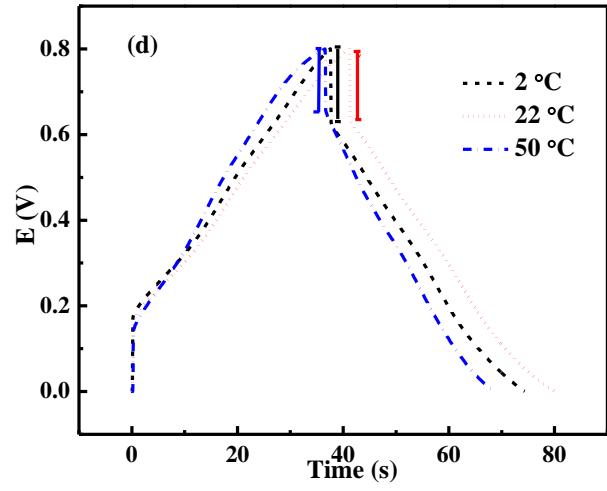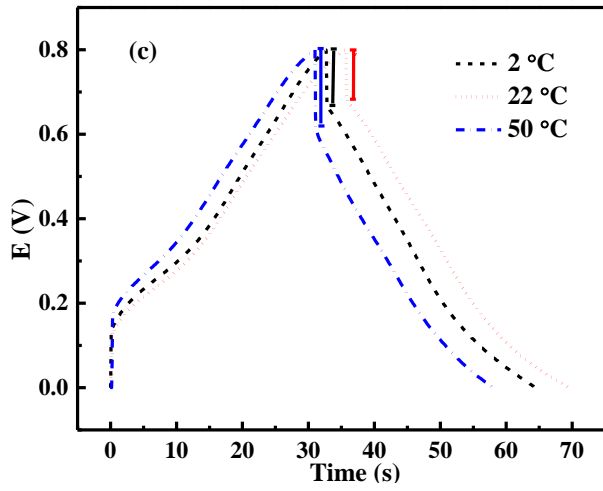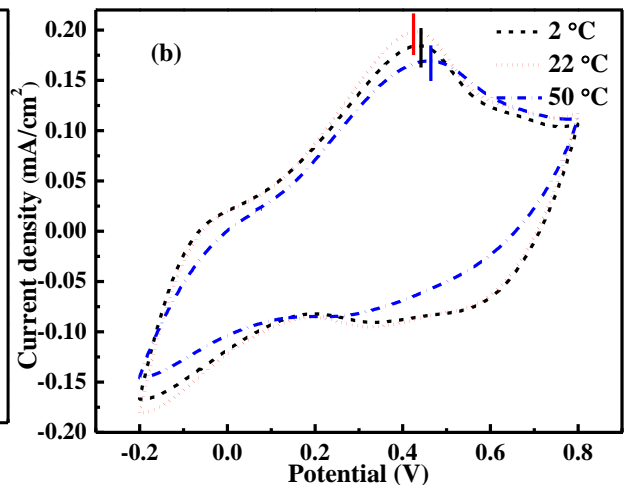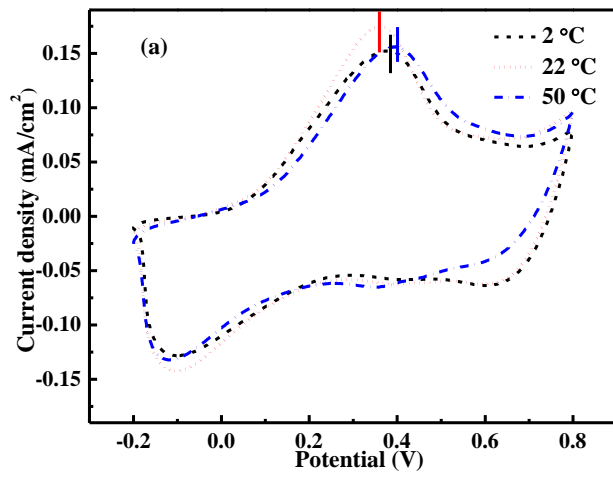
which is also consistent with the calculated D values as 2 ℃ (4.21×10^{-13} cm^2/s) < 22 ℃ (4.23×10^{-13} cm^2/s) for pristine PANI and 2 ℃ (4.23×10^{-13} cm^2/s) < 22 ℃ (6.68×10^{-13} cm^2/s) for PANI/MnFe$_2$O$_4$ nanocomposites film from Figure B4.15. However, the increased *ESR* and R_{ct} values in the pristine film and the disappeared semicircle in the PANI/MnFe$_2$O$_4$ nanocomposites films at 50 ℃ is subsequently observed and attributed to the destruction effect of high temperature on the PANI structure, demonstrating by the decreased D values as pristine PANI (3.31×10^{-13} cm^2/s) and PANI/MnFe$_2$O$_4$ nanocomposites (5.22×10^{-13} cm^2/s) at 50 ℃.

4.4. Conclusions

A PANI matrix embedded with MnFe$_2$O$_4$ particles nanocomposites film has been successfully prepared by an electrodeposition of PANI monomers onto a MnFe$_2$O$_4$ coated ITO glass method. A multi-color electrochromic phenomenon displayed at different potentials has been observed in this nanocomposites film due to the dominant PANI component in the composites. A higher coloration efficiency and a faster switching response than that of the pristine PANI film are obtained due to the inner interactions between the PANI matrix and the MnFe$_2$O$_4$ particles as well as the resulted rougher morphology. The PANI/MnFe$_2$O$_4$ nanocomposites film also exhibits an enhanced areal capacitance compared to that of the pristine PANI film at low scan rates due to the capacitive role of MnFe$_2$O$_4$. A negative role of increasing H$_2$SO$_4$ concentration on the supercapacitive behaviors of pristine PANI and PANI/MnFe$_2$O$_4$ nanocomposites films has been demonstrated by the increased R_{ct} values. The positive role of increasing the temperature during the relative low temperature range on both the pristine PANI and PANI/MnFe$_2$O$_4$ composites films has been obtained due to the greatly facilitated mobility of ions. However, both fast degradations of pristine PANI and PANI/MnFe$_2$O$_4$ nanocomposites films structure have been observed implying a destroying role of the relatively high temperatures. These novel PANI/MnFe$_2$O$_4$

nanocomposites films, that can be easily produced, have demonstrated considerable electrochromic and capacitive behaviors, which make them suitable for application in devices integrated the functions of EC and energy storage.

4.5. References

1. H. Wang, E. Zhu, J. Yang, P. Zhou, D. Sun and W. Tang, *J. Phys. Chem. C*, 2012, **116**, 13013-13019.
2. W. Fan, C. Zhang, W. W. Tjiu, K. P. Pramoda, C. He and T. Liu, *ACS Appl. Mater. Interfaces*, 2013, **5**, 3382-3391.
3. Z. Gao, W. Yang, J. Wang, B. Wang, Z. Li, Q. Liu, M. Zhang and L. Liu, *Energy & Fuels*, 2012, **27**, 568-575.
4. S. Dhibar and C. K. Das, *Ind. Eng. Chem. Res.*, 2014, **53**, 3495-3508.
5. C. Yuan, B. Gao, L. Shen, S. Yang, L. Hao, X. Lu, F. Zhang, L. Zhang and X. Zhang, *Nanoscale*, 2011, **3**, 529-545.
6. Y. Yin, C. Liu and S. Fan, *J. Phys. Chem. C*, 2012, **116**, 26185-26189.
7. J. Zhang and X. S. Zhao, *ChemSusChem*, 2012, **5**, 818-841.
8. H. Wei, C. He, J. Liu, H. Gu, Y. Wang, X. Yan, J. Guo, D. Ding, N. Z. Shen, X. Wang, S. Wei and Z. Guo, *Polymer*, 2015, **67**, 192-199.
9. Y. Li, X. Zhao, P. Yu and Q. Zhang, *Langmuir*, 2012, **29**, 493-500.
10. Y. Xiao, Q. Zhang, J. Yan, T. Wei, Z. Fan and F. Wei, J. Electroanal. Chem., 2012, 684, 32-37.
11. K. Wang, J. Huang and Z. Wei, *J. Phys. Chem. C*, 2010, **114**, 8062-8067.
12. D. Susanti, D.-S. Tsai, Y.-S. Huang, A. Korotcov and W.-H. Chung, *J. Phys. Chem. C*, 2007, **111**, 9530-9537.
13. Y. Wu, J. Zhang, Z. Fei and Z. Bo, *J. Am. Chem. Soc.*, 2008, **130**, 7192-7193.
14. Y. Xia and J. Ouyang, *J. Mater. Chem.*, 2011, **21**, 4927-4936.
15. J. Jang and J. H. Oh, *Adv. Funct. Mater.*, 2005, **15**, 494-502.
16. J. Jang, J. Ha and J. Cho, *Adv. Mater.*, 2007, **19**, 1772-1775.
17. M. R. Anderson, B. R. Mattes, H. Reiss and R. B. Kaner, *Science*, 1991, **252**, 1412-1415.
18. A. G. MacDiarmid and A. J. Epstein, *Faraday Discuss. Chem. Soc.*, 1989, **88**, 317-332.
19. Y. Zhao, H. Wei, M. Arowo, X. Yan, W. Wu, J. Chen, Y. Wang and Z. Guo, *Phys. Chem. Chem. Phys.*, 2015, **17**, 1498-1502.
20. S. Zhou, H. Zhang, Q. Zhao, X. Wang, J. Li and F. Wang, *Carbon*, 2012, **52**, 440–450.
21. L. Mao, K. Zhang, H. S. O. Chan and J. Wu, *J. Mater. Chem.*, 2012, **22**, 80-85.
22. A. Watanabe, K. Mori, Y. Iwasaki, Y. Nakamura and S. Niizuma, *Macromolecules*, 1987, **20**, 1793-1796.
23. C. H. B. Silva, N. A. Galiote, F. Huguenin, É. Teixeira-Neto, V. R. L. Constantino and M. Temperini, *J. Mater. Chem.*, 2012, **22**, 14052-14060.
24. C. Yang, H. Wei, L. Guan, J. Guo, Y. Wang, X. Yan, X. Zhang, S. Wei and Z. Guo, *J. Mater. Chem. A*, 2015, **3**, 14929-14941.
25. P. Patil, J.-M. Lee, Y.-K. Seo, Y. K. Hwang, Y.-U. Kwon, S. H. Jhung and J.-S. Chang, *J. Nanosci. Nanotechnol.*, 2009, **9**, 318-326.
26. H. Pang, C. Huang, J. Chen, B. Liu, Y. Kuang and X. Zhang, *J Solid State Electrochem.*, 2010, **14**, 169-174.
27. L. Geng, Y. Zhao, X. Huang, S. Wang, S. Zhang and S. Wu, *Sens. Actuators, B*, 2007, **120**, 568-572.
28. S. Patil, S. C. Raghavendra, M. Revansiddappa, P. Narsimha and M. V. N. Ambika Prasad, *Bull Mater Sci.*, 2007, **30**, 89-92.

29. B. Nandapure, S. Kondawar, M. Salunkhe and A. Nandapure, *J. Compos. Mater.*, 2012, **47**, 559-567.
30. S. Sarmah and A. Kumar, *Indian J Phys.*, 2011, **85**, 713-726.
31. L. Shao, J.-W. Jeon and J. L. Lutkenhaus, *J. Mater. Chem. A*, 2013, **1**, 7648-7656.
32. J. Zhang, J.-p. Tu, D. Zhang, Y.-q. Qiao, X.-h. Xia, X.-l. Wang and C.-d. Gu, *J. Mater. Chem.*, 2011, **21**, 17316-17324.
33. O. Tovide, N. Jaheed, N. Mohamed, E. Nxusani, C. E. Sunday, A. Tsegaye, R. F. Ajayi, N. Njomo, H. Makelane, M. Bilibana, P. G. Baker, A. Williams, S. Vilakazi, R. Tshikhudo and E. I. Iwuoha, *Electrochim. Acta*, 2014, **128**, 138-148.
34. Z. Wang, X. Zhang, Y. Li, Z. Liu and Z. Hao, *J. Mater. Chem. A*, 2013, **1**, 6393-6399.
35. Y. Fu and X. Wang, *Ind. Eng. Chem. Res.*, 2011, **50**, 7210-7218.
36. B. Li, Y. Fu, H. Xia and X. Wang, *Mater. Lett.*, 2014, **122**, 193-196.
37. W. Wei, X. Cui, W. Chen and D. G. Ivey, *Chem. Soc. Rev.*, 2011, **40**, 1697-1721.
38. I. Kotutha, E. Swatsitang, W. Meewassana and S. Maensiri, *Jpn. J. Appl. Phys.*, 2015, **54**, 06FH10.
39. L. Zheng, Y. Xu, D. Jin and Y. Xie, *Chemistry – An Asian Journal*, 2011, **6**, 1505-1514.
40. X. Lu, W. Zhang, C. Wang, T. C. Wen and Y. Wei, *Prog. Polym. Sci.*, 2011, **36**, 671-712.
41. B. Senthilkumar, K. Vijaya Sankar, C. Sanjeeviraja and R. Kalai Selvan, *J. Alloys Compd.*, 2013, **553**, 350-357.
42. K. Xie, J. Li, Y. Lai, Z. a. Zhang, Y. Liu, G. Zhang and H. Huang, *Nanoscale*, 2011, **3**, 2202-2207.
43. Q. Wu, Y. Xu, Z. Yao, A. Liu and G. Shi, *ACS Nano*, 2010, **4**, 1963-1970.
44. L. J. Sun, X. X. Liu, K. K. T. Lau, L. Chen and W.-M. Gu, *Electrochim. Acta*, 2008, **53**, 3036-3042.
45. D. S. Patil, J. S. Shaikh, D. S. Dalavi, S. S. Kalagi and P. S. Patil, *Mater. Chem. Phys.*, 2011, **128**, 449-455.
46. J. Ge, G. Cheng and L. Chen, *Nanoscale*, 2011, **3**, 3084-3088.
47. Y. Zhang, H. Feng, X. Wu, L. Wang, A. Zhang, T. Xia, H. Dong, X. Li and L. Zhang, *Int. J. Hydrogen Energy*, 2009, **34**, 4889-4899.
48. G. Wang, L. Zhang and J. Zhang, *Chem. Soc. Rev.*, 2012, **41**, 797-828.
49. R. Vellacheri, A. Al Haddad, H. Zhao, W. Wang, C. Wang and Y. Lei, *Nano Energy*, 2014, **8**, 231-237.
50. X. Liu and P. G. Pickup, *Energy Environ. Sci.*, 2008, **1**, 494-500.
51. W. Liu, X. Yan, J. Lang and Q. Xue, *J. Mater. Chem.*, 2012, **22**, 8853-8861.
52. C. Buron, B. Lakard, A. Monnin, V. Moutarlier and S. Lakard, *Synth. Met.*, 2011, **161**, 2162-2169.
53. C. Peng, D. Hu and G. Z. Chen, *Chem. Commun.*, 2011, **47**, 4105-4107.
54. A. R. Elkais, M. M. Gvozdenović, B. Z. Jugović, J. S. Stevanović, N. D. Nikolić and B. N. Grgur, *Prog. Org. Coat.*, 2011, **71**, 32-35.
55. A. Kellenberger, E. Dmitrieva and L. Dunsch, *J. Phys. Chem. B*, 2012, **116**, 4377-4385.
56. L. Feng, L. Yan, Z. Cui, C. Liu and W. Xing, *J. Power Sources*, 2011, **196**, 2469-2474.
57. H. Gu, Y. Huang, X. Zhang, Q. Wang, J. Zhu, L. Shao, N. Haldolaarachchige, D. P. Young, S. Wei and Z. Guo, *Polymer*, 2011, **53**, 801–809.
58. W. A. El-Said, C. H. Yea, J. W. Choi and I. K. Kwon, *Thin Solid Films*, 2009, **518**, 661-667.

59.   J. Zhu, S. Wei, L. Zhang, Y. Mao, J. Ryu, N. Haldolaarachchige, D. P. Young and Z. Guo, *J. Mater. Chem.*, 2011, **21**, 3952-3959.

60.   J. Singh, A. P. Bhondekar, M. L. Singla and A. Sharma, *ACS Appl. Mater. Interfaces*, 2013, **5**, 5346-5357.

61.   H. Wang, Q. Hao, X. Yang, L. Lu and X. Wang, *ACS Appl. Mater. Interfaces*, 2010, **2**, 821-828.

62.   G. Zhang and F. Yang, *Phys. Chem. Chem. Phys.*, 2011, **13**, 3291-3302.

63.   P. Khiew, N. Huang, S. Radiman and M. S. Ahmad, *Mater. Lett.*, 2004, **58**, 516-521.

64.   S. Ameen, M. S. Akhtar, Y. S. Kim, O. B. Yang and H. S. Shin, *Colloid. Polym. Sci.*, 2011, **289**, 415-421.

65.   L. Li, J. Jiang and F. Xu, *Eur. Polym. J.*, 2006, **42**, 2221-2227.

66.   R. Ganesan and A. Gedanken, *Nanotechnology*, 2008, **19**, 435709.

67.   X. Han and Y.-S. Wang, *Phys. Scr.*, 2007, **2007**.

68.   W. Huang and A. MacDiarmid, *Polymer*, 1993, **34**, 1833-1845.

69.   A. A. Argun, P. H. Aubert, B. C. Thompson, I. Schwendeman, C. L. Gaupp, J. Hwang, N. J. Pinto, D. B. Tanner, A. G. MacDiarmid and J. R. Reynolds, *Chem. Mater.*, 2004, **16**, 4401-4412.

70.   J. Zhang, J. p. Tu, D. Zhang, Y. q. Qiao, X. h. Xia, X. l. Wang and C. d. Gu, *J. Mater. Chem.*, 2011, **21**, 17316-17324.

71.   A. Sonavane, A. Inamdar, H. Deshmukh and P. Patil, *J. Phys. D: Appl. Phys.*, 2010, **43**, 315102.

72.   C. M. Amb, A. L. Dyer and J. R. Reynolds, *Chem. Mater.*, 2010, **23**, 397-415.

73.   H. Wei, X. Yan, S. Wu, Z. Luo, S. Wei and Z. Guo, *J. Phys. Chem. C*, 2012, **116**, 25052-25064.

74.   D. Ma, G. Shi, H. Wang, Q. Zhang and Y. Li, *Nanoscale*, 2013, **5**, 4808-4815.

75.   C. Fu, C. Foo and P. S. Lee, *Electrochim. Acta*, 2014, **117**, 139-144.

76.   H. Ling, L. Liu, P. S. Lee, D. Mandler and X. Lu, *Electrochim. Acta*, 2015, **174**, 57-65.

77.   A. Rudge, J. Davey, I. Raistrick, S. Gottesfeld and J. P. Ferraris, *J. Power Sources*, 1994, **47**, 89-107.

78.   F. Fusalba, P. Gouérec, D. Villers and D. Bélanger, *J. Electrochem. Soc.*, 2001, **148**, A1.

79.   H. Mi, X. Zhang, X. Ye and S. Yang, *J. Power Sources*, 2008, **176**, 403-409.

80.   J. Liu, J. Jiang, M. Bosman and H. J. Fan, *J. Mater. Chem.*, 2012, **22**, 2419-2426.

81.   Y.-Y. Horng, Y.-C. Lu, Y.-K. Hsu, C.-C. Chen, L.-C. Chen and K.-H. Chen, *J. Power Sources*, 2010, **195**, 4418-4422.

82.   Z. Wei, K. Wang, H. Wu, Y. Meng and Y. Zhang, *Energy Environ. Sci.*, 2012, **5**, 8384-8389.

83.   J. Yan, T. Wei, B. Shao, Z. Fan, W. Qian, M. Zhang and F. Wei, *Carbon*, 2010, **48**, 487-493.

84.   S. H. Mujawar, S. B. Ambade, T. Battumur, R. B. Ambade and S.-H. Lee, *Electrochim. Acta*, 2011, **56**, 4462-4466.

85.   H. Xia, C. Hong, B. Li, B. Zhao, Z. Lin, M. Zheng, S. V. Savilov and S. M. Aldoshin, *Adv. Funct. Mater.*, 2015, **25**, 627-635.

86.   J. Broughton and M. Brett, *Electrochim. Acta*, 2004, **49**, 4439-4446.

87.   Y.-P. Lin and N.-L. Wu, *J. Power Sources*, 2011, **196**, 851-854.

88.   X. Wang, K. Gao, Z. Shao, X. Peng, X. Wu and F. Wang, *J. Power Sources*, 2014, **249**, 148-155.

89. A. C. Nwanya, C. J. Jafta, P. M. Ejikeme, P. E. Ugwuoke, M. V. Reddy, R. U. Osuji, K. I. Ozoemena and F. I. Ezema, *Electrochim. Acta*, 2014, **128**, 218-225.
90. H. Wei, J. Zhu, S. Wu, S. Wei and Z. Guo, *Polymer*, 2013, **54**, 1820-1831.
91. H. Li, J. Wang, Q. Chu, Z. Wang, F. Zhang and S. Wang, *J. Power Sources*, 2009, **190**, 578-586.
92. W. Liu, X. Yan, J. Lang and Q. Xue, *J. Mater. Chem.*, 2012, **22**, 8853-8861.
93. W. Li, K. Xu, L. An, F. Jiang, X. Zhou, J. Yang, Z. Chen, R. Zou and J. Hu, *J. Mater. Chem. A*, 2014, **2**, 1443-1447.

Appendix B

for

Chapter 4 Electropolymerized Polyaniline/Manganese Iron Oxide Hybrids with Enhanced

Color Switching Response and Electrochemical Energy Storage
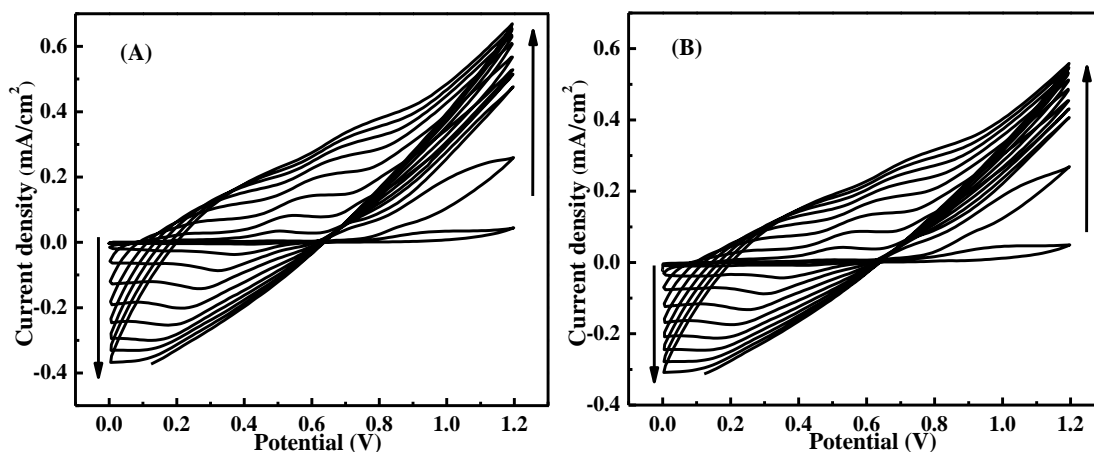
Figure B4.11. Electropolymerization synthesis of PANI onto (A) bare and (B) MnFe$_2$O$_4$ coated ITO glasses at a scan rate of 50 mV/s in 0.5 M H$_2$SO$_4$ aqueous solution containing 0.1 M aniline.
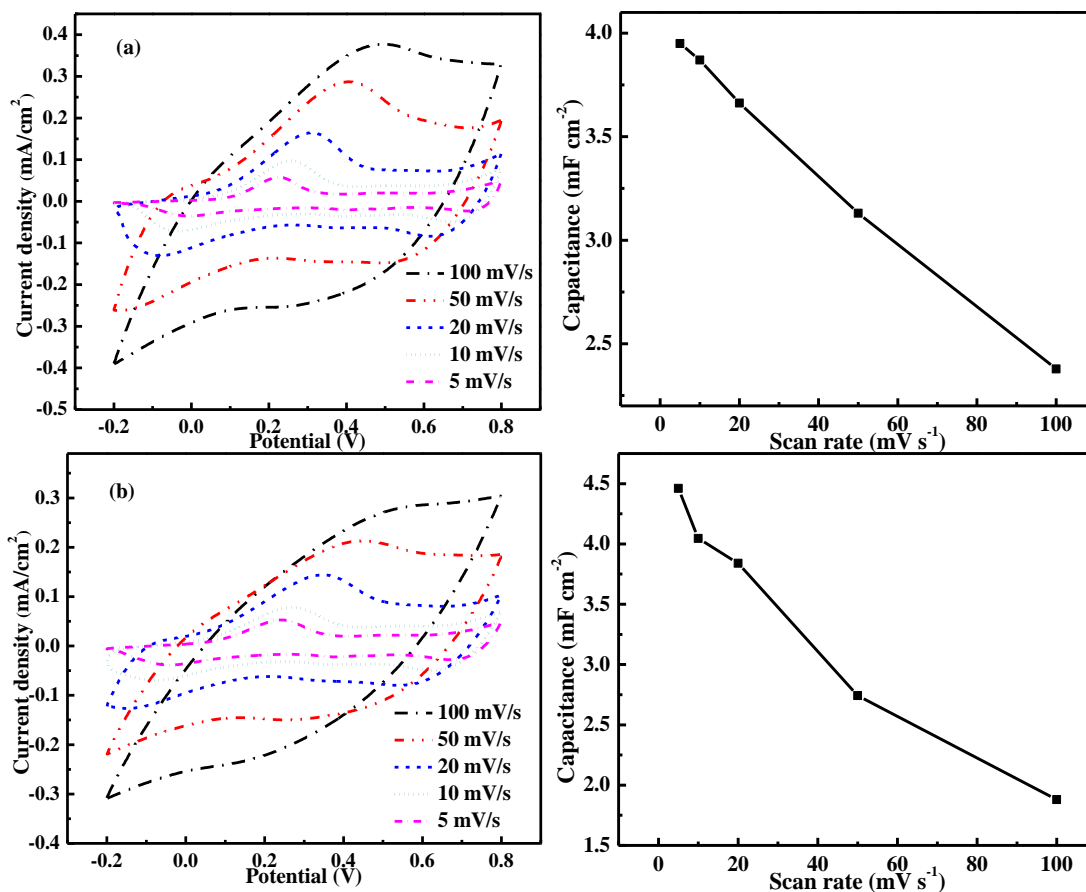
Figure B4.12. CV curves (left) and corresponding scan rate dependent areal capacitance (right) of (a) pristine PANI film and (b) PANI/MnFe$_2$O$_4$ nanocomposite film at different scan rates under a potential range from -0.2 to 0.8 V in 1.0 M H$_2$SO$_4$ aqueous solution.
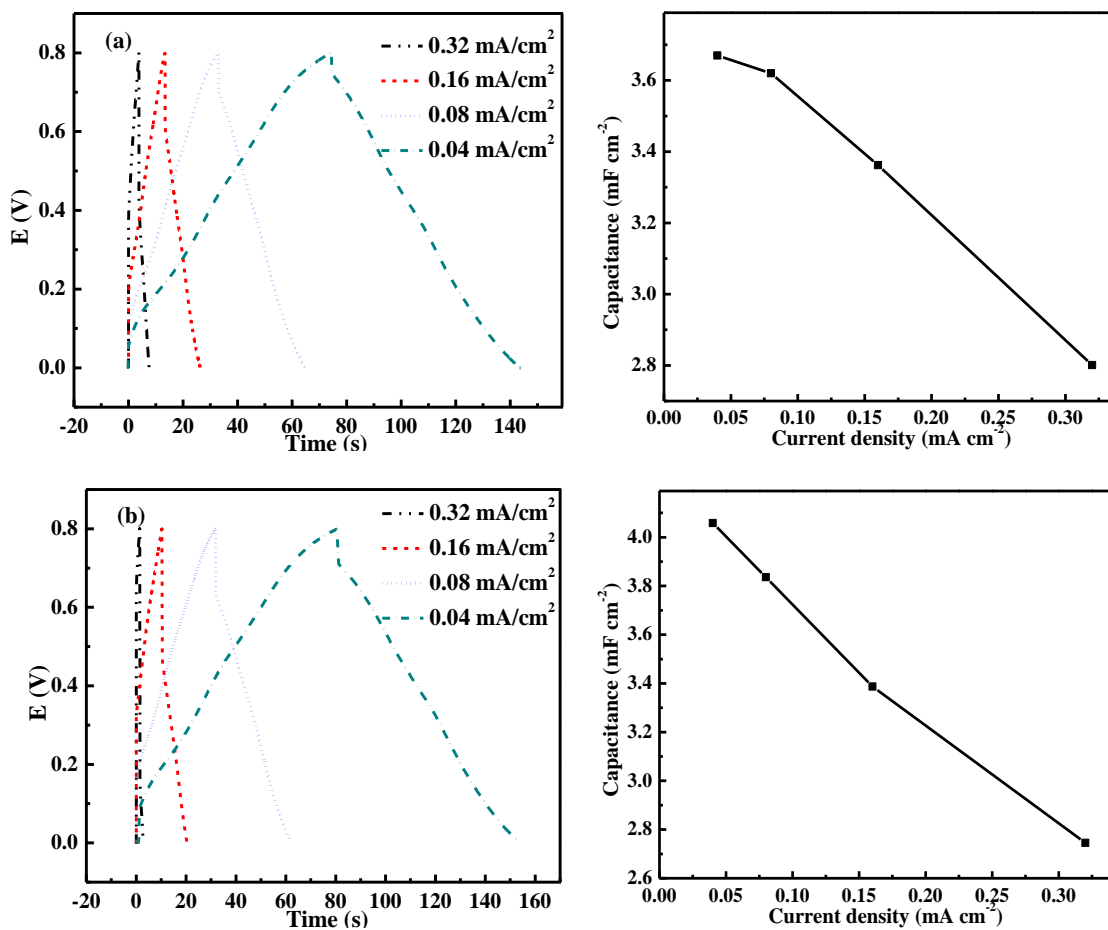
Figure B4.13. Galvanostatic charge-discharge curves (on the left) and corresponding current density dependent areal capacitance (on the right) of (a) pristine PANI film and (b) PANI/MnFe$_2$O$_4$ nanocomposite film in 1.0 M H$_2$SO$_4$ aqueous solution.
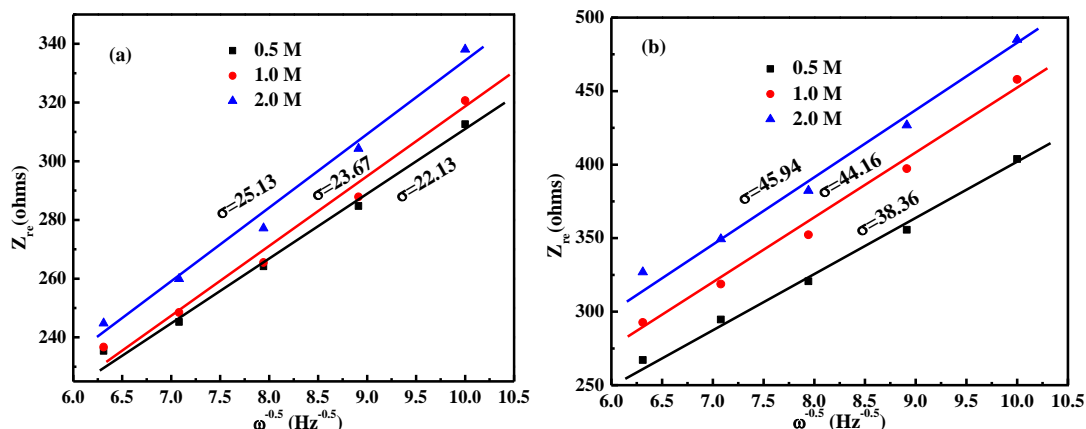
Figure B4.14. The Warburg factor σ of (a) pristine PANI and (b) PANI/Mn$_2$FeO$_4$ nanocomposites films conducted in 0.5, 1.0 and 2.0 M H$_2$SO$_4$ aqueous solution.
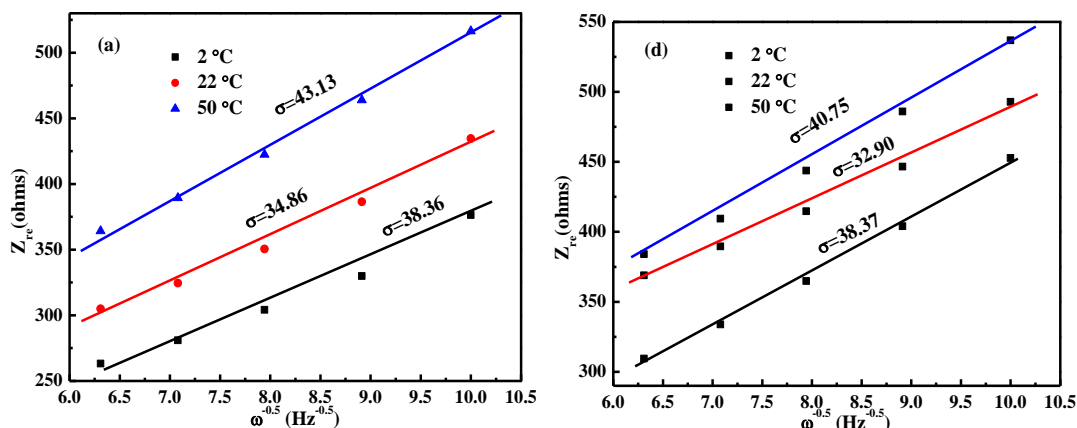
Figure B4.15. The Warburg factor σ of (a) pristine PANI and (b) PANI/Mn$_2$FeO$_4$ nanocomposites films conducted in 2, 22 and 50 °C H$_2$SO$_4$ aqueous solution.

The anion diffusion coefficient can be calculated from Equation A(1):

$$D = R^2 T^2 / (2A^2 n^4 F^4 C^2 \sigma^2) \hspace{3cm} \text{A(1)}$$

where D is the diffusion coefficient of the HSO$_4^-$ anions, R is the gas constant (8.314), T is the absolute temperature, A is the surface area of the electrode (4 cm^2), n is the number of electrons per molecule during the oxidization (n is 2), F is the Faraday constant (96485 sA/mol), C is the concentration of ions (mol/cm^3), σ is the Warburg factor which can be obtained from the slopes in the low frequency region (<1 Hz) of EIS (Figure B4.14&15).

135
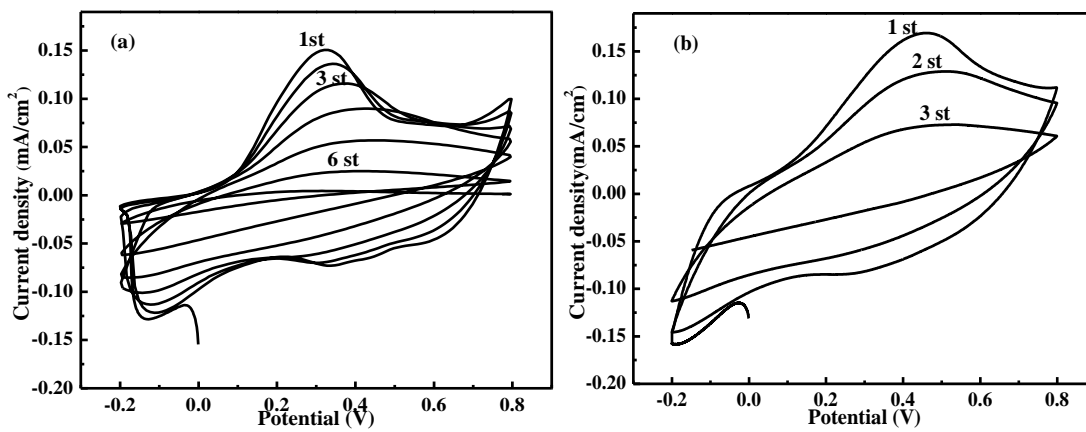
Figure B4.16. The first 6 and 3 CVs of the pristine PANI and PANI/MnFe₂O₄ nanocomposite films at 50 ºC.

Chapter 5 Double Reinforced Graphene Energy Storage by KOH Activation and Nitrogen Doping

Abstract

For the goal of synthesizing high performance supercapacitor electrode materials to meet the pressing requirements of energy storage, nitrogen doped activated graphene (N-AG) was successfully synthesized by employing two steps of KOH activating and following nitrogen doping using a hydrothermal method. Continuously increased I_D/I_G ratios were observed in Raman spectra after the KOH activation and following N-doping process, indicating increased defects due to the etching effect of KOH and the introduced nitrogen defects on graphene sheet. Stacked graphene with damaged sheets on the surface was clearly seen in transmission electron microscopy (TEM) image after the KOH etching. The successful dopant of N was demonstrated by X-ray photoelectron spectroscopy (XPS) spectra and energy-dispersive X-ray spectroscopy (EDS) mapping, confirming this effective hydrothermal N doping method. The N-AG exhibited largely enhanced capacitance (186.63 F/g) and cycling stability compared with that of nitrogen doped graphene (N-G, 50.88 F/g) and activated graphene (AG, 58.38 F/g) due to the combined positive effects of KOH activation and N-doping. This facile hydrothermal method through combining the KOH activation and nitrogen doping processes is of great significance of scaling the production, the synthesized N-AG represents a promising alternative candidate to commonly used electrode materials in supercapacitor.

5.1. Introduction

Electrochemical storage device with high energy and power density are highly desired with the fast-growing market for portable electronics, hybrid electric vehicles and stand-by power systems. Due to their high power densities, fast charging/discharging rate, sustainable cycling life and excellent cycle stability, ultracapacitors based on electrostatic interactions between ions in the electrolyte and electrodes, occurring in so-called electrical double layers (EDLs) are widely explored and become a promising technique to utilize intermittent renewable energy.[1–3] Different carbon nanomaterials such as activated carbon,[4] carbon black,[5,6] carbon onions,[7,8] carbon nanotubes[9,10] and carbon nanofibers[11,12] have been widely employed for electrode materials of ultracapacitors due to their high specific surface area and excellent conductivity. However, pure carbon materials based ultracapacitors always exhibit low capacitances which largely limit their applications to complementary energy storage devices to batteries.[13] In order to resolve the insufficient capacitance issue, another class of capacitors as pseudocapacitors was developed, which employed metal oxides[14,15] and conducting polymers[16,17] to store electrical energy based on the redox reaction near the surfaces of those active materials.[18] However, the poor cycle lives of most pseudocapacitors are the main limitations as the redox reactions are not fully reversible and also accompanied with the swell-shrinkage of electrode.[19–21] In this case, the strategy of introducing pseudocapacitance properties to the electrode materials of ultracapacitors is a promising route to increase the capacitances to those of pseudocapacitors while utilize the robust charging mechanisms of ultracapacitors for their excellent cycle lives.[12,22,23]

Among all the carbon materials, graphene with an atom-thick two dimensional (2D) carbon structures has been widely investigated due to its unique electrical, chemical, thermal, and mechanical properties.[24–27] Nowadays, In order to advance its various potential applications such

as nanoelectronics, energy storage/conversion, and catalysis,[28] dramatic scientific endeavors have been launched toward the optimization of graphene by manipulating its electronic, mechanical, chemical and structural properties.[29,30] Reconstructed graphene could potentially result in localized highly reactive regions and thus unexpected properties.[31] For example, enriching reactive oxygen functional groups on graphene sheets can provide ample covalent bonding sites for the chemical functionalization.[32,33] In addition, introducing heteroatoms into the carbon frameworks is another effective way to improve the specific performances of graphene.[34] For example, certain heteroatom (B, S, N and P) dopant seems to be the most promising choice for enhancing capacity, surface wettability and electronic conductivity of graphene while maintaining the superb cycle ability.[35–38] Among them, nitrogen (N)-doped carbon has been extensively investigated recently, the synthesized N-graphene exhibits excellent performance in oxygen reduction reaction (ORR) and lithium ion battery due to its unique electronic interactions between the lone-pair of nitrogen and the π-system of graphic carbon.[39,40] Nowadays, two approaches as post-treatment in N-environment or in-situ doping using N-containing precursors are mainly employed to achieve this goal.[41] However, their complicated preparation procedures and high cost of manipulations largely restrict the practical uses in large scale. Therefore, an easy operation method producing N-graphene with uniform and high-concentration nitrogen is still urgently needed.

Alternatively, it is generally accepted that the capacitance and power capability of the carbon materials are largely related to their electrolyte-accessible surface area and the kinetics within active materials.[42] Chemical activation has been proven as a high efficient method to obtain carbons with high specific surface area and narrow micropore distribution.[43–46] Among all the chemical activation agents, potassium hydroxide (KOH) as a strong alkaline is very promising due to its etching nature, negligible activation temperature, high yields, resulted well defined

micropore size distribution and ultrahigh specific surface area.[46,47] Enhanced performances of numerous kinds of carbon such as carbon black,[48] coals,[49] chars,[50] fibers,[45] nonotubes[44] and graphenes[51] have been observed after KOH activation. Furthermore, since a large number of defects can be introduced on the graphene sheets after KOH etching, it is expected that different nitrogen doping levels can be obtained on the KOH activated graphene due to the altered mechanical structure and electron transfer pathway.

Herein, we reported a facile hydrothermal method combining both KOH activation and N-doping processes to synthesize nitrogen doped activated graphene (N-AG) using exfoliated graphene oxide (GO) solution as precursor. GO simply suffers N-doping and KOH activation was also synthesized as N-graphene (N-G) and porous graphene (AG) as control experiments. These reactions were carried out in a mild hydrothermal environment employing KOH and ammonia as reactants. The defects variation on graphene sheets after KOH activation and N-doping was investigated by Raman spectra and X-ray photoelectron spectroscopy (XPS). The morphology of graphene was revealed by scanning electron microscopy (SEM) and transmission electron microscopy (TEM). The doped N element was confirmed by the XPS and energy-dispersive X-ray spectroscopy (EDS) mapping. The supercapacitive performance and kinetics comparison were proceeded by cyclic voltammetry (CV), galvanostatic charge-discharge and electrochemical impedance spectroscopy (EIS) measurements. Cycling performance was also included to evaluate the practical application.

5.2. Experimental

5.2.1. Materials

Natural graphite powders were supplied by Bay Carbon Inc, USA. Potassium persulfate ($K_2S_2O_8$, ≥99.0%), phosphorus pentoxide (P_2O_5, ≥98.0%) and potassium permanganate (KMnO$_4$,

≥99.0%) were purchased from Sigma Aldrich. Potassium hydroxide (KOH, BioXtra, ≥85% KOH basis), ammonium hydroxide (NH_4OH, Assay: 28.0 to 30.0 w/w %), sulfuric acid (H_2SO_4, 93-98%), hydrochloric acid (HCl, 37.5%) and hydrogen peroxide aqueous solution (PERDROGEN® 30% H_2O_2 (w/w)) were purchased from Alfa Aesar. The dialysis membrane (Spectra/Por, molecular weight cut off (MWCO): 12000-14000) was commercially obtained from Spectrum Laboratories, Inc. All the materials were used as received without any further treatment.

5.2.2. Synthesis Method

Graphite oxide (GO) was synthesized following the modified Hummers method.[25] For the synthesis of nitrogen doped graphene (N-G) and KOH activated graphene (AG), 26.0 g homogeneous GO solution (0.338 g GO) was first transferred to a 40 mL teflon lined hydrothermal autoclave, 3 mL NH_4OH solution or well dissolved KOH solution (4.05 g KOH, mass KOH : GO = 12:1) was added, the solution was diluted to 40 mL by DI water and sealed maintaining at 150 ºC for 3 hrs. After cooling down, the precipitates were collected by filtration and washed with water for 3 times, the products were dried naturally for 72 hours. Reduced graphene oxide (RGO) was also obtained following the same procedure using simple GO solutions as a control experiment. For the synthesis of N-AG, 0.2 g synthesized AG powders were uniformly grinded and dissolved in 30 mL water, which undergo a 30 min sonication to achieve a uniform distribution, the AG solution was then transferred to a 40 mL autoclave added with 1.80 mL NH_4OH solution (same NH_4OH/AG ratio as that of NH_4OH/GO). Similar procedures were following proceeded to obtain the N-AG powder products.

5.2.3. Preparation of Working Electrode

Three electrode system was employed to characterize the supercapacitive property. The working glassy carbon electrode with a diameter of 3 mm was successively polished with 1.0 and

0.05 μm alumina powders on a microcloth wetted with doubly distilled water to produce an electrode with a mirror-like surface. For the preparation of sample coated electrode, 5.0 mg graphene was added to 1.0 mL ethanol solution of nafion (the content of nafion is 0.1 wt%), then the mixture was treated for 30 min with ultrasonication to form a uniform suspension. The obtained suspension (5 μL) was dropped on the surface of the well-treated glassy carbon electrode. Finally, the resultant modified glassy carbon electrode was dried naturally at room temperature.

5.2.4. Characterizations

Raman spectra were obtained using a Horiba Jobin-Yvon LabRam Raman confocal microscope with 785 nm laser excitation at a 1.5 cm^{-1} resolution at room temperature.

The microstructure of the sample was observed on a JEOL JEM-2100 transmission electron microscopy (TEM) and a JSM-6700F field emission scanning electron microscope (SEM). The element distributions were examined by using an energy-dispersive X-ray spectroscopy (EDS) detector attached to the SEM.

X-ray photoelectron spectroscopy (XPS) was conducted on a Kratos Analytical spectrometer, using Al Ka = 1486.6 eV radiation as the excitation source, under a condition of anode voltage of 12 kV and an emission current of 10 mA. The element peaks were deconvoluted into the components on a Shirley background.

5.2.5. Electrochemical Evaluations

The electrochemical experiments were conducted in a conventional three-electrode cell. The as-prepared glassy carbon electrode deposited with active materials was used as the working electrode, platinum wire as the counter electrode, and saturated calomel electrode (SCE) (0.241 V vs. SHE) serving as reference electrode. All the potentials were referred to the SCE.

Cyclic voltammogram (CV) ranging from 0 to 1.0 V at a series of scan rates and galvanostatic charge-discharge (GCD) measurements from 0 to 0.8 V with different current densities were conducted in 1.0 M H_2SO_4 aqueous solution. Electrochemical impedance spectroscopy (EIS) was carried out in the frequency range of 100, 000 to 0.01 Hz with a 5 mV amplitude referring to the open circuit potential. The cycling stability was investigated through evaluating capacitance retention by running 1000 galvanostatic charge-discharge cycles. Corresponding capacitance, energy & power densities, simulated charge transfer resistance as well as capacitance retention values were obtained and compared.

5.3. Research and Discussions

5.3.1. Raman Analysis

Raman spectrum is a powerful tool to characterize the crystalline structure of carbon-based materials due to their strong response to the specific electronic property. Figure 5.1(a-d) shows the Raman spectra of RGO, N-G, AG and N-AG, respectively. Similar D and G band located around 1300 and 1600 cm^{-1} are clearly seen for all the graphenes. The G band is attributed to the E_{2g} phonon mode of in-plane sp^2 carbon atoms while the D band is induced by the interruption of regular hexagonal network structure such as in-plane defects, edge defects and dangling bonds. The intensity ratio of D to G band (I_D/I_G, donated as R) is a reliable indicator to evaluate the degree of structural defects on the graphene sheets and a higher R value means more defects and disordered structure on the graphene surface. The calculated R values are provided in Table 5.1, It is clearly obtained that the R value follows an order as N-AG (1.301) > AG (1.232) > N-G (1.046) > pure graphene (1.038), indicating that the amount of defect is increased monotonously after KOH activation and N-doping processes, respectively. In addition, the role of KOH activation is more predominant as confirmed by the largely increased R value, indicating a great increase of defects

or edge area on graphene sheets due to the KOH etching. Finally, an obvious negative shift of G band (from 1596 to 1581 cm^{-1}) is clearly seen after KOH activation as shown in Figure 5.1(c&d), the negative shifts are probably due to the uniaxial tensile strain on graphene, suggesting an reduction of GO by KOH.[52–54] The in-plane crystalline size (L_a) is also calculated using the following Equation (1) and summarized in Table 5.1.

$$La = \frac{560}{E_\lambda^4}\left(\frac{I_D}{I_G}\right)^{-1}$$

(1)

where E_λ is the excitation laser energy in eV used in the Raman measurement. It is clearly seen from Table 5.1 that the L_a value is inversely proportional to the R value, indicating that the basal structure of graphene has been affected due to the introduced N containing sites and increased defects caused by KOH activation. Notably, the largely decreased L_a values of AG and N-AG are probably attributed to the KOH etching caused stack of graphene.

5.3.2. Morphology Characterization

The morphology variation of these four graphene was characterized by SEM as shown in Figure 5.2(a-d), TEM images were also provided inset each SEM image. It is clearly seen from Figure 5.2(a) that the RGO maintains a typical crumpled graphene structure, which is further confirmed by the inset TEM image. For N-G, Figure 5.2(b), similar morphologies have been observed, indicating a negligible effect of ammonia on the morphology of RGO. However, it is clearly seen from Figure 5.2(c) that the graphene sheets are inclined to stack together after the KOH activation, which is probably due to the hydroxide reduction resulted decrease of oxygen containing groups on graphene sheet. In addition, a high amount of pyrolytic carbon is also noticed on their surface

Table 5.1. Summary of the I_D/I_G (R) and L_a values of different graphenes

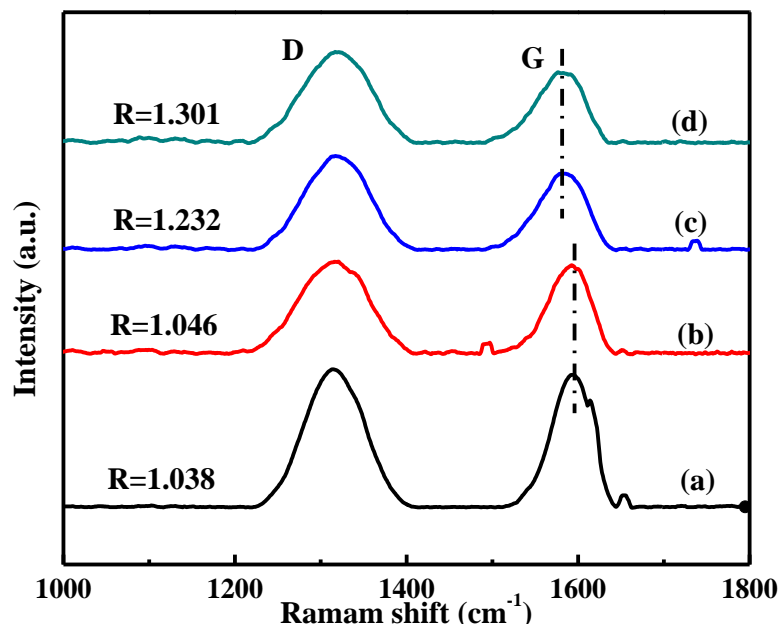| Sample ID	R	L_a (nm)
Pure graphene	1.038	86.57
N-G	1.046	85.91
AG	1.232	72.94
N-AG	1.301	69.07

Figure 5.1. Raman spectra of (a) RGO, (b) N-G, (c) AG and (d) N-AG

of graphene due to the KOH etching effect, which is further disclosed in the TEM image as a large concentration of defects are generated on the graphene surface, giving rise to increased edge area. Furthermore, the HRTEM image at the edge of AG clearly shows the graphite layers, implying that KOH activation treatment can induce the stacking of graphene which is also consistent with the negative shift of G band in Raman. In contrast, a more fluffy structure of graphene is obtained for N-AG, Figure 5.2(d), which is probably attributed to the sonicated process and the implanted oxygen containing groups form ammonia. However, the typical stack structure has not been changed for N-AG as confirmed by the inset TEM image. In order to further characterize the element distributions in N-AG, EDS elemental mapping characterization was also employed and displayed in Figure 5.2(e-h), uniform distributions of C (blue), O (green), K (red) and N (white) bright dots are clearly seen, confirming the good distribution of corresponding elements and the effectiveness of this hydrothermal method. For the existence of K, most studies suggest that the hydroxide reduction can lead to H_2, K metal, and carbonates as illustrated by the reaction.[44]

$$6KOH + C \leftrightarrow 2K + 3H_2 + 2K_2CO_3$$

In addition, this successful N doping method is also confirmed by the EDS mapping images of N-G as shown in Figure C5.7

5.3.3. XPS Investigation

XPS as a powerful tool to investigate the composition and valence state of contained elements was also employed to characterize the structural variation of graphene as shown in Figure 5.3. Figure 5.3(A) discloses the wide scan surveys of (a) RGO, (b) N-G, (c) AG and (d) N-AG. Common peaks as C1s and O 1s are both seen for all these four graphene, indicating the existence of oxygen containing groups. Furthermore, for AG and N-AG, Figure 5.3A(c&d), obvious peaks assigned to K 2s (378 eV) and K 2p3 (290 eV) are also observed, indicating the containment of K which comes
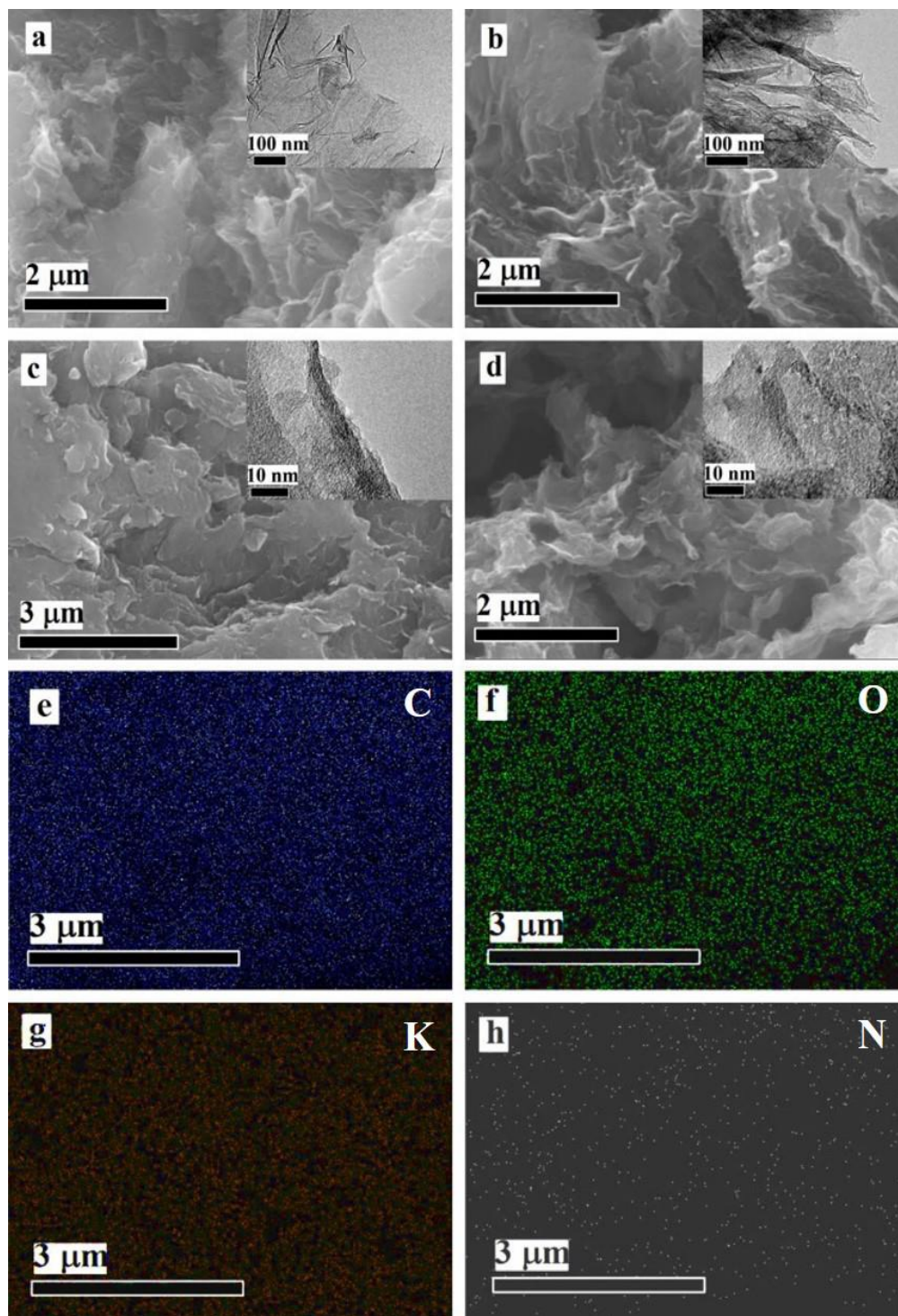
Figure 5.2. SEM image of (a) RGO, (b) N-G, (c) AG and (d) N-AG, inset is the corresponding TEM image. EDS mappings of N-AG are also provided as (e) C, (f) O, (g) K and (h) N.

Figure 5.3. XPS image as (A) wide scan survey of (a) RGO, (b) N-G, (c) AG and (d) N-AG, (B) curve fitting of N in N-G (bottom) and N-AG (top), (C) curve fitting of C in RGO (bottom) and N-G (top), (D) curve fitting of C in AG (bottom) and N-AG (top), (E) curve fitting of O in RGO (bottom) and N-G (top) and (F) curve fitting of O in AG (bottom) and N-AG (top)
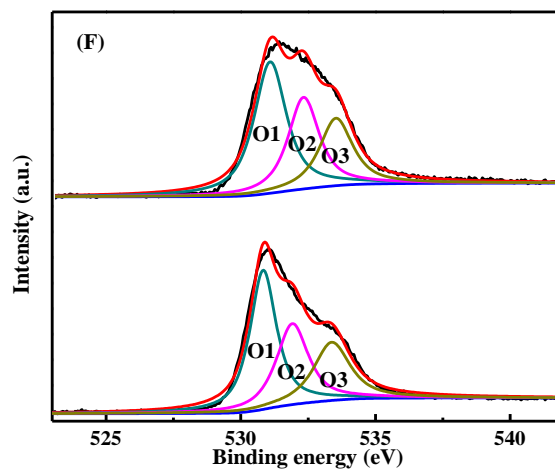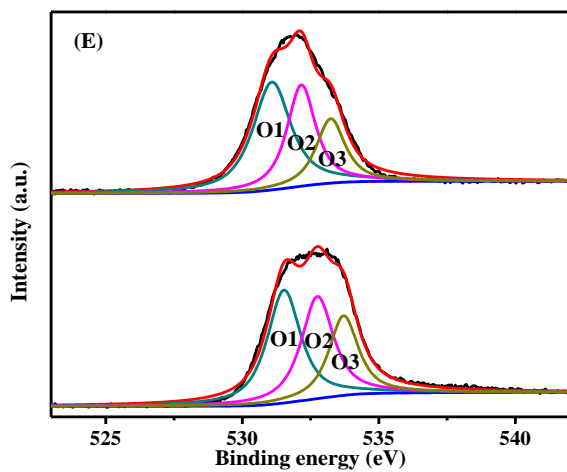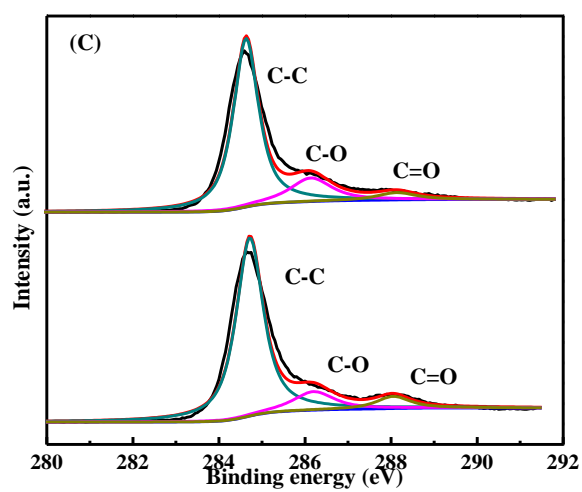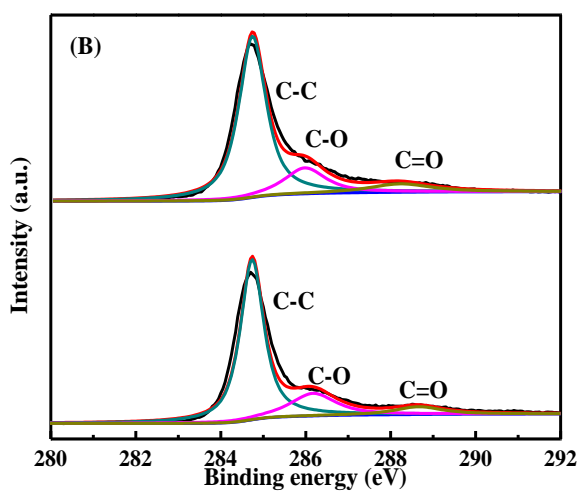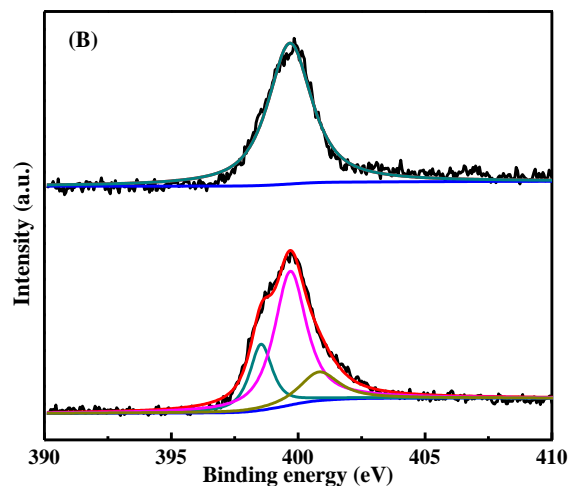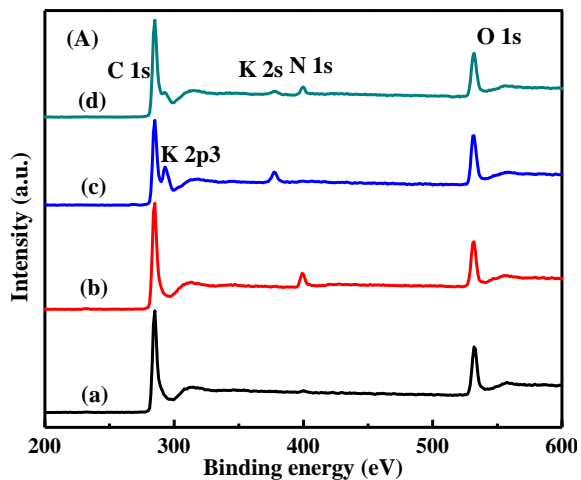
from the KOH precursor. In addition, for N-G and N-AG, Figure 5.3A(b&d), clear peak belonging

to N 1s is clearly seen around 400 eV, demonstrating the successful dopant of N. In order to obtain

detailed information about the dopant N, high-resolution curve fitting of N is further proceeded

for N-G and N-AG as shown in Figure 5.3(B). For bottom located N-G, three peaks with binding

energies at 398.6, 400.0, and 401.7 eV representing pyridinic, pyrrolic, and quaternary nitrogen

are clearly obtained, pyridinic and pyrrolic N can contribute to the increase of Fermi energy (E_f)

and density of states (DOS) of graphene, while quaternary nitrogen is described as "graphitic

nitrogen" which have a p-doping effect.[55] In details, pyridinic-N refers to nitrogen atoms at the

edge of graphene planes, each of which is bonded to two carbon atoms and donates one p-electron

to the aromatic π systems. Pyrrolic-N refers to nitrogen atoms that are bonded to two carbon atoms

and contribute to the π system with two p-electons. Quaternary nitrogen is also called "substituted

nitrogen", in which nitrogen atoms are incorporated into the graphene layer and replace carbon

atoms within a graphene plane.[56] Numerous studies have reported that the enhanced

electrocatalytic activity is mainly attributed to puridinic-N and/or pyrrolic-N.[57] In contrast, for the

top N-AG, only one peak belonging to pyrrolic nitrogen is obtained, different curve fitting results

are probably due to the KOH activation process. For the curve fitting of C, Figure 5.3(B&C), three

main groups as C-C (284.6), C-O (286.5) and C=O (288.2) are obtained for all the graphene

samples, which originate from the oxidation and destruction of the sp^2 atomic structures of pristine

graphene, indicating the existence of oxygen containing groups regardless of the KOH activating

and N-doping processes. Figure 5.3(E&F) shows the curve fitting of O in the four graphene. The

XPS spectra are fitted to get detailed chemical bonding information about the element O with

carbon. Three peaks located around 531.08, 532.03, and 533.04 eV can be assigned to the species

of O_1, C=O (oxygen doubly bonded to aromatic carbon), O_2, C-OH (oxygen singly bonded to

aliphatic carbon), and O_3, C-O-C/HO-C=O, respectively.[58,59] It is clearly seen from Figure 5.3(F) that the ratio of $(O_2+O_3)/O_1$ is largely decreased after KOH activation, indicating a decrease of oxygen containing groups due to the hydroxide reduction which is also consistent with the TEM results about the graphene stack phenomenon. However, slight increases of O_2 and O_3 have been found for N-AG, top of Figure 5.3(F), indicating an increase of implanted oxygen containing groups during the reaction with ammonia.

5.3.4 Capacitance Investigation

The capacitive performances of the graphene based electrodes were studied using cyclic voltammogram (CV) at a high scan rate of 500 mV/s within a potential range of -0.2 to 0.8 V in 1.0 M H_2SO_4 as shown in Figure 5.4(A), The CV curves at other scan rates (1000, 200, 100, 50 and 20 mV/s) are also provided in Figure C5.8. Higher current densities and larger enclosed CV areas are clearly seen in N-AG, followed by AG, N-G and RGO, indicating more energy is stored in the N-AG due to the increased etched edge area and the introduced N-defects. It is clearly seen from Figure. C5.8a that all the RGO exhibit nonrectangular CV curves with one obvious pair of redox peaks around 0.4/0.3V which indicate the existence of oxygen-containing functionalities.[60] However, these redox peaks are largely depressed and the shape becomes more rectangular after N doping as confirmed by all the CV curves of N-G in Figure C5.8b, indicating the positive role of dopant N and the ideal double layer capacitor nature with a charge/ discharge process. However, the redox peaks still existed in AG after KOH activation as shown in Figure 5.4(A)c. In addition, a largely increased peak area of AG is observed compared with that of RGO due to the increased rough structure increased specific surface area, indicating the positive role of KOH activation. For N-AG, Figure 5.4(A)d, depressed redox peaks were observed due to the introduced N-defects. Obviously, it is seen from Figure 5.4(A) that the N-AG exhibits a much higher current density than
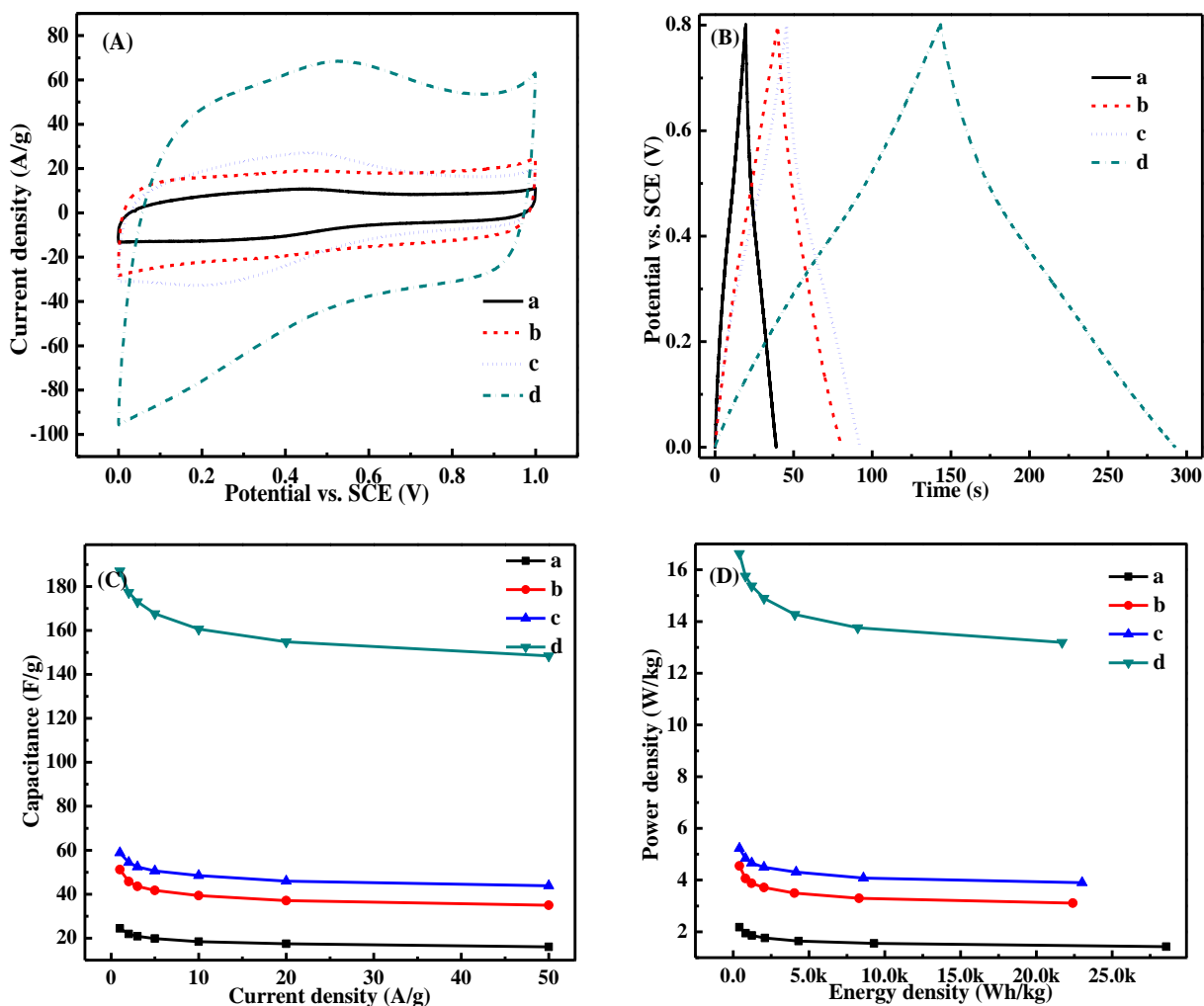
Figure 5.4. (A) CV conducted at a scan rate of 500 mV/s and (B) Charge−discharge with a current density as 1 A/g, (C) specific capacitance dependence on current density and (D) Ragone plot of (a) RGO, (b) N-G, (c) AG and (d) N-AG measured in 1.0 M H_2SO_4 aqueous solution, the data is normalized to the mass of graphene.

other graphene counterparts, suggesting that N-AG is the most promising materials as supercapacitor electrodes among all the samples.

Galvanostatic charge-discharge (GCD) as a reliable method for measuring the specific capacitance of supercapacitor was also conducted in the same H_2SO_4 solution from 0 to 0.8 V with a current density as 1 A/g as shown in Figure 5.4(B). The GCD measurements with different current densities were also provided in Figure C5.9. The increase in the discharging time always represents a higher capacitance. It is obtained that the capacitance of graphene can be greatly enhanced through the KOH activation and the N doping as confirmed by the discharging time order as RGO < N-G < AG < N-AG. The specific capacitances of different graphene samples calculated from the CV at 500 mV/s and the charge-discharge at 1 A/g are summarized in Table 5.2, the capacitance values observed in CV and C-d curves follow the same order as N-AG > AG > N-G > RGO, confirming the positive roles of KOH activation and N-doping respectively. Furthermore, the correlation between the specific capacitance and the current density for these four graphene samples is also presented in Figure 5.4C. The N-AG has the highest capacity among all samples at all the same scan rate. For instance, the N-AG achieves a specific capacitance as 186.63 F/g with 1 A/g current density, which is three and four times higher than the specific capacity for AG (58.38 F/g) and N-G (24.25 F/g), respectively. Notably, the capacitance shows almost nine times larger than that of RGO (24.25 F/g), indicating a dramatic capacitance increase when combining KOH activation with N-doping processes. Furthermore, the N-AG shows a capacity of 186.63 and 154.33 F/g with 1 and 50 A/g current density, respectively, suggesting a good rate capability for N-AG supercapacitors. In addition, the voltage drop at the initiation of the discharge is extremely small of N-AG among all the graphene samples, indicating a very low equivalent

Table 5.2. Summary of capacitance, energy density and power density values of different graphenes calculated for CV and GCD results.

Graphene	CV C$_s$. 500 mV/s (F/g)	C-d C$_s$. 1 A/g (F/g)	Energy density (Wh/kg)	Power density (W/kg)
RGO	16.30	24.25	2.16	404.25
N-G	34.63	50.88	4.52	397.05
AG	37.86	58.38	5.19	403.54
N-AG	104.21	186.63	16.59	399.22

series resistance (ESR) in the supercapacitor and the potential of N-AG for high-power operations. The Ragone plot of these four graphene as shown in Figure 5.4(D) further confirms the enhancement in power density of N-AG. Similar power density trend was clearly observed as N-AG > AG > N-G > RGO with similar range of energy density. The as-developed N-AG also outperforms graphene reported previously and is also even comparable to those of metal oxide/graphene and polymer/graphene composites in terms of capacitance and energy density.[61–65] It should be noted that, besides the appealing electrochemical properties as supercapacitor, the facile prepared N-AG may also show considerable performances regarding oxygen reduction reaction (ORR) and Li-ion batteries, which is pivotal to its wide practical applications.[39,40]

5.3.5. EIS Characterization

Electrochemical impedance spectroscopy (EIS) as a power technique to obtain a further fundamental understanding of the inherent reaction kinetics of the electrode materials was also employed. Figure 5.5 presents the semicircular Nyquist plots of imaginary (Z", Ω) versus real (Z', Ω) components of impedance conducted in the frequency range of 100, 000 to 0.01 Hz with a 5 mV amplitude referring to open potential in 1.0 M H_2SO_4. The enlarged part of the high frequency region is also provided, no resistor-capacitor (RC) loops or semicircles appear in the high frequency region, indicating a negligible charge resistance.[66] The excellent capacitance performance can be signified by the vertical approached line of high frequency part, the closer the line to the Y-axis, the better the performance of the graphene electrode. It is clearly seen from the enlarged high frequency part that the slope of the graphene samples follow an order as N-AG > AG > N-G > RGO, demonstrating enhanced reaction kinetics due to the KOH activation and N doping and is also in good consistence with the CV and GCD analysis. In order to further analyze the EIS behavior comprehensively and deeply, simulations were performed on the basis of the

157

equivalent-circuit model using ZsimpWin commercial software based on an equivalent electric circuit as shown inset of Figure 5.5, where R is the total resistance during charge transfer and Q is the non-ideal capacitance. The simulated results and associated % error are provide in Table 5.3. Almost the same R values are clearly obtained due to the same solution resistance. Furthermore, it is clearly observed that the Q value increased monotonously as N-AG > AG > N-G > RGO, indicating the same energy storage trend after KOH activation and N-doping.

5.3.6. Cycling performance

Since a long cycling performance is among the most important criteria for supercapacitors, the cycling performance is conducted using GCD for 1000 cycles with a current density of 1 A/g. The cycling performances with specific capacitances are shown in Figure 5.6. It is clearly seen that all the graphene electrodes exhibit excellent performance due to the charging mechanisms of ultracapacitors. All the capacitances have a great retention after 1000 cycles and follow the same order as initial capacitances. However, an obvious capacitance increase is clearly seen for N-AG due to the electro-activation, which implies its great potential application as supercapacitor materials due to this comparable capacitance as that of pesudocapacitors and the excellent cycling performance, highlighting that N-AG have an excellent electrochemical stability and a high degree of reversibility. The above results clearly reveal that the electrochemical performance of graphene can be greatly enhanced combining KOH activation and nitrogen doping processes.

5.4. Conclusions

A facile hydrothermal synthesis method combining KOH activation and N-doping was successfully employed to synthesize nitrogen doped activated graphene, which is economically and effectively at a very high yield, implying feasibility for mass production. The synthesized N-
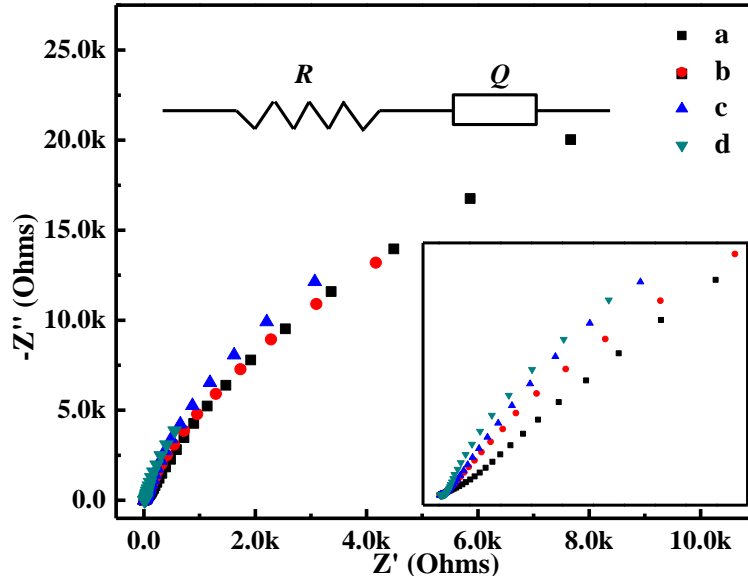
Figure 5.5. Nyquist plot of (a) RGO, (b) N-G, (c) AG and (d) N-AG, respectively. The inset is the enlarged part of high frequency region.

Table 5.3. Impedance components for different electrodes by fitting the experimental data using Zsimp-Win software based on the equivalent circuit presented inset of Figure 5.5

electrode	R/Ω		Q/C		n	
	value	error %	value	error %	value	error %
RGO	5.504	1.907	0.00042	1.675	0.8219	0.517
N-G	5.402	2.293	0.00089	2.25	0.8556	0.7615
AG	8.193	3.46	0.00102	3.57	0.855	1.309
N-AG	11.11	4.558	0.00331	5.443	0.8476	2.481
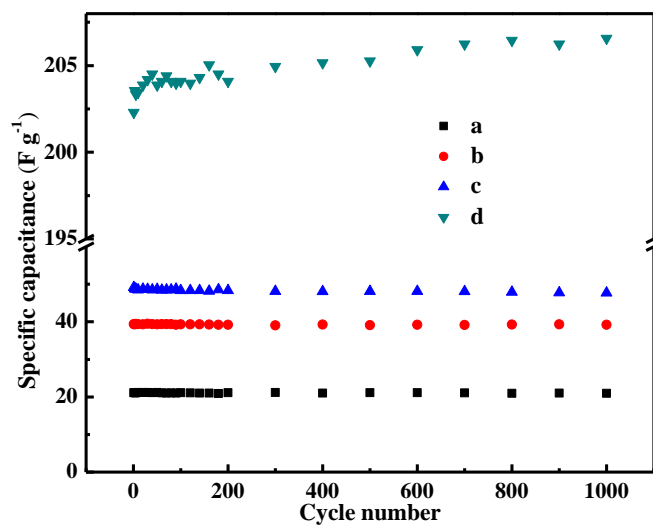
Figure 5.6. Cycling performance as a function of cycling number at a current density of 1 A/g for (a) RGO, (b) N-G, (c) AG and (d) N-AG, respectively

AG exhibited relatively decreased oxygen containing groups with increased defects due to the etching nature of KOH and the doped N-sites. These unique properties endow them as promising electrodes for supercapacitors with high capacity, excellent rate capability, and long-term stability. Due to the possibility of scalable synthesis and prominent properties, the N-AG can offer attractive opportunities for both fundamental study and potential industrial applications in catalysis, adsorption, energy storage, and energy conversion systems.

5.5. References

1. A. Burke, J. Power Sources, 2000, 91, 37–50.
2. M. D. Stoller, S. Park, Y. Zhu, J. An and R. S. Ruoff, Nano Lett., 2008, 8, 3498–3502.
3. J. Chen, C. Li and G. Shi, J. Phys. Chem. Lett., 2013, 4, 1244–1253.
4. G. Xu, C. Zheng, Q. Zhang, J. Huang, M. Zhao, J. Nie, X. Wang and F. Wei, Nano Res., 2011, 4, 870–881.
5. P. Kossyrev, J. Power Sources, 2012, 201, 347–352.
6. N. Jäckel, D. Weingarth, M. Zeiger, M. Aslan, I. Grobelsek and V. Presser, J. Power Sources, 2014, 272, 1122–1133.
7. J. K. McDonough, A. I. Frolov, V. Presser, J. Niu, C. H. Miller, T. Ubieto, M. V. Fedorov and Y. Gogotsi, Carbon, 2012, 50, 3298–3309.
8. Y. Gao, Y. S. Zhou, M. Qian, X. N. He, J. Redepenning, P. Goodman, H. M. Li, L. Jiang and Y. F. Lu, Carbon, 2013, 51, 52–58.
9. B. Kim, H. Chung and W. Kim, Nanotechnology, 2012, 23, 155401.
10. Y. J. Kang, H. Chung, C.-H. Han and W. Kim, Nanotechnology, 2012, 23, 65401.
11. Y.-H. Hsu, C.-C. Lai, C.-L. Ho and C.-T. Lo, Electrochimica Acta, 2014, 127, 369–376.
12. L.-F. Chen, X.-D. Zhang, H.-W. Liang, M. Kong, Q.-F. Guan, P. Chen, Z.-Y. Wu and S.-H. Yu, ACS Nano, 2012, 6, 7092–7102.
13. H. M. Jeong, J. W. Lee, W. H. Shin, Y. J. Choi, H. J. Shin, J. K. Kang and J. W. Choi, Nano Lett., 2011, 11, 2472–2477.
14. H. Wang, Z. Xu, H. Yi, H. Wei, Z. Guo and X. Wang, Nano Energy, 2014, 7, 86–96.
15. Y. Jiang, P. Wang, X. Zang, Y. Yang, A. Kozinda and L. Lin, Nano Lett., 2013, 13, 3524–3530.
16. H. Wei, Y. Wang, J. Guo, X. Yan, R. O'Connor, X. Zhang, N. Z. Shen, B. L. Weeks, X. Huang, S. Wei and Z. Guo, ChemElectroChem, 2015, 2, 119–126.
17. Y. Zhao, H. Wei, M. Arowo, X. Yan, W. Wu, J. Chen, Y. Wang and Z. Guo, Phys Chem Chem Phys, 2015, 17, 1498–1502.
18. V. Augustyn, P. Simon and B. Dunn, Energy Environ. Sci., 2014, 7, 1597.
19. K. Kai, Y. Kobayashi, Y. Yamada, K. Miyazaki, T. Abe, Y. Uchimoto and H. Kageyama, J. Mater. Chem., 2012, 22, 14691.
20. G. A. Snook, P. Kao and A. S. Best, J. Power Sources, 2011, 196, 1–12.
21. J. Yang, T. Lan, J. Liu, Y. Song and M. Wei, Electrochimica Acta, 2013, 105, 489–495.
22. F. Su, C. K. Poh, J. S. Chen, G. Xu, D. Wang, Q. Li, J. Lin and X. W. Lou, Energy Env. Sci, 2011, 4, 717–724.
23. G. Lota, B. Grzyb, H. Machnikowska, J. Machnikowski and E. Frackowiak, Chem. Phys. Lett., 2005, 404, 53–58.
24. A. K. Geim and K. S. Novoselov, Nat. Mater., 2007, 6, 183–191.
25. Y. Wang, Q. He, H. Qu, X. Zhang, J. Guo, J. Zhu, G. Zhao, H. A. Colorado, J. Yu, L. Sun, S. Bhana, M. A. Khan, X. Huang, D. P. Young, H. Wang, X. Wang, S. Wei and Z. Guo, J Mater Chem C, 2014, 2, 9478–9488.
26. J. Zhu, M. Chen, Q. He, L. Shao, S. Wei and Z. Guo, RSC Adv., 2013, 3, 22790.
27. Y. Wang, H. Wei, Y. Lu, S. Wei, E. Wujcik and Z. Guo, Nanomaterials, 2015, 5, 755–777.
28. A. K. Geim, Science, 2009, 324, 1530–1534.

29. Z. Wen, X. Wang, S. Mao, Z. Bo, H. Kim, S. Cui, G. Lu, X. Feng and J. Chen, Adv. Mater., 2012, 24, 5610–5616.
30. D. Chen, L. Tang and J. Li, Chem. Soc. Rev., 2010, 39, 3157.
31. V. M. Pereira, A. H. Castro Neto, H. Y. Liang and L. Mahadevan, Phys. Rev. Lett., 2010, 105.
32. G. Goncalves, P. A. A. P. Marques, C. M. Granadeiro, H. I. S. Nogueira, M. K. Singh and J. Grácio, Chem. Mater., 2009, 21, 4796–4802.
33. V. Georgakilas, M. Otyepka, A. B. Bourlinos, V. Chandra, N. Kim, K. C. Kemp, P. Hobza, R. Zboril and K. S. Kim, Chem. Rev., 2012, 112, 6156–6214.
34. L. Dai, Acc. Chem. Res., 2013, 46, 31–42.
35. J. Han, L. L. Zhang, S. Lee, J. Oh, K.-S. Lee, J. R. Potts, J. Ji, X. Zhao, R. S. Ruoff and S. Park, ACS Nano, 2013, 7, 19–26.
36. F. Razmjooei, K. P. Singh, M. Y. Song and J.-S. Yu, Carbon, 2014, 78, 257–267.
37. C. N. R. Rao, K. Gopalakrishnan and A. Govindaraj, Nano Today, 2014, 9, 324–343.
38. X. Wang, G. Sun, P. Routh, D.-H. Kim, W. Huang and P. Chen, Chem Soc Rev, 2014, 43, 7067–7098.
39. D. Geng, Y. Chen, Y. Chen, Y. Li, R. Li, X. Sun, S. Ye and S. Knights, Energy Environ. Sci., 2011, 4, 760.
40. H. Wang, C. Zhang, Z. Liu, L. Wang, P. Han, H. Xu, K. Zhang, S. Dong, J. Yao and G. Cui, J. Mater. Chem., 2011, 21, 5430.
41. H. Wang, T. Maiyalagan and X. Wang, ACS Catal., 2012, 2, 781–794.
42. N. P. Wickramaratne, J. Xu, M. Wang, L. Zhu, L. Dai and M. Jaroniec, Chem. Mater., 2014, 26, 2820–2828.
43. Y. Zhu, S. Murali, M. D. Stoller, K. J. Ganesh, W. Cai, P. J. Ferreira, A. Pirkle, R. M. Wallace, K. A. Cychosz, M. Thommes, D. Su, E. A. Stach and R. S. Ruoff, Science, 2011, 332, 1537–1541.
44. E. Raymundo-Piñero, P. Azaïs, T. Cacciaguerra, D. Cazorla-Amorós, A. Linares-Solano and F. Béguin, Carbon, 2005, 43, 786–795.
45. S.-H. Yoon, S. Lim, Y. Song, Y. Ota, W. Qiao, A. Tanaka and I. Mochida, Carbon, 2004, 42, 1723–1729.
46. J. Wang and S. Kaskel, J. Mater. Chem., 2012, 22, 23710.
47. K. Kierzek, E. Frackowiak, G. Lota, G. Gryglewicz and J. Machnikowski, Electrochimica Acta, 2004, 49, 515–523.
48. D. Lozano-Castelló, M. A. Lillo-Ródenas, D. Cazorla-Amorós and A. Linares-Solano, Carbon, 2001, 39, 741–749.
49. H. Marsh, D. S. Yan, T. M. O'Grady and A. Wennerberg, Carbon, 1984, 22, 603–611.
50. J. A. Maciá-Agulló, B. C. Moore, D. Cazorla-Amorós and A. Linares-Solano, Carbon, 2004, 42, 1367–1370.
51. T. Kim, G. Jung, S. Yoo, K. S. Suh and R. S. Ruoff, ACS Nano, 2013, 7, 6899–6905.
52. T. M. G. Mohiuddin, A. Lombardo, R. R. Nair, A. Bonetti, G. Savini, R. Jalil, N. Bonini, D. M. Basko, C. Galiotis, N. Marzari, K. S. Novoselov, A. K. Geim and A. C. Ferrari, Phys. Rev. B, 2009, 79.
53. C. Casiraghi, Phys. Status Solidi RRL - Rapid Res. Lett., 2009, 3, 175–177.
54. Y. Liu, D. Zhang, Y. Shang and C. Guo, Bull. Mater. Sci., 2014, 37, 1529–1533.
55. S. H. Park, J. Chae, M.-H. Cho, J. H. Kim, K.-H. Yoo, S. W. Cho, T. G. Kim and J. W. Kim, J Mater Chem C, 2014, 2, 933–939.

56. Y. Shao, S. Zhang, M. H. Engelhard, G. Li, G. Shao, Y. Wang, J. Liu, I. A. Aksay and Y. Lin, J. Mater. Chem., 2010, 20, 7491.
57. C. Zhang, R. Hao, H. Liao and Y. Hou, Nano Energy, 2013, 2, 88–97.
58. A. Ganguly, S. Sharma, P. Papakonstantinou and J. Hamilton, J. Phys. Chem. C, 2011, 115, 17009–17019.
59. L. Zhang, L. Ji, P.-A. Glans, Y. Zhang, J. Zhu and J. Guo, Phys. Chem. Chem. Phys., 2012, 14, 13670.
60. S.-Y. Yang, K.-H. Chang, H.-W. Tien, Y.-F. Lee, S.-M. Li, Y.-S. Wang, J.-Y. Wang, C.-C. M. Ma and C.-C. Hu, J Mater Chem, 2011, 21, 2374–2380.
61. S. R. C. Vivekchand, C. S. Rout, K. S. Subrahmanyam, A. Govindaraj and C. N. R. Rao, J. Chem. Sci., 2008, 120, 9–13.
62. Y. Xu, K. Sheng, C. Li and G. Shi, ACS Nano, 2010, 4, 4324–4330.
63. N. A. Kumar, H.-J. Choi, Y. R. Shin, D. W. Chang, L. Dai and J.-B. Baek, ACS Nano, 2012, 6, 1715–1723.
64. Y. Wang, H. Sun, R. Zhang, S. Yu and J. Kong, Carbon, 2013, 53, 245–251.
65. B. Wang, J. Park, C. Wang, H. Ahn and G. Wang, Electrochimica Acta, 2010, 55, 6812–6817.
66. C. Xiang, M. Li, M. Zhi, A. Manivannan and N. Wu, J. Mater. Chem., 2012, 22, 19161.

Appendix C

for

Chapter 5 Double Reinforced Graphene Energy Storage by KOH Activation and Nitrogen

Doping

Synthesis of GO

Specifically, prior to the Hummers synthesis of GO, natural graphite powders were first experienced a pre-oxidation process in order to promote the complete oxidation of graphite. In detail, 3.0 g natural graphite powders, 4.0 g $K_2S_2O_8$ and 4.0 g P_2O_5 were weighed and mixed together following with an addition of 12 mL H_2SO_4, the mixture was then heated up to 80 °C and kept for 6 hrs. After cooled down to room temperature, distilled water was used to dilute and wash the products till the rinsed water turned neutral. The pre-oxidized product was dried at room temperature overnight naturally in preparation for the following Hummers oxidation process. The intermediate product was dispersed in 120 mL H_2SO_4 at 0 °C following with a gradual addition of 15.0 g $KMnO_4$, stirring was maintained in the meantime for the removal of heat while the temperature was controlled below 20 °C. The mixture was transferred to a water bath and kept at 35 °C for 2 hrs under magnetic stirring to complete the oxidation process. Finally, 250 mL distilled water was added in and 15 min later, another 700 mL distilled water and 20 mL H_2O_2 solution were added in sequence to terminate the oxidation reaction. The solution turned from blackish purple to bright yellow and was filtered and washed with 1 L HCl aqueous solution (1:9 v/v) to remove metal ions. The obtained GO slurry was re-dispersed with certain amount of distilled water to form a 1.5 wt% diluted suspension, which was further subjected to a dialysis process within a dialysis membrane package to completely remove the residual metal ions and acid. The final concentration of the as-synthesized GO aqueous solution was determined by measuring the weight difference before and after drying at 60 °C overnight as 1.31 wt%.

Calculations of Capacitance, Energy Density and Power Density

The capacitance of the electrodes was calculated from the corresponding CV curves at different scan rates from the corresponding CV curves at different scan rates from 0 to 1 V in 1.0 M H_2SO_4 aqueous solution using Equation (1):

$$C_s = \left(\int idV\right)\big/(2m \times \Delta V \times v) \tag{1}$$

Where C_s is the specific capacitance in F/g, $\int idV$ is the integrated area of the CV curve, m is the mass of the active materials in the single electrode in g, ΔV is the scanned potential window in V, and v is the scan rate in V/s.

The capacitance from the GCD curves was calculated using Equation (2):

$$C_s = (i \times t)/(m \times \Delta V) \tag{2}$$

Where C_s is the specific gravimetric capacitance in F/g, i is the discharge current in A, t is the discharge time in s, m is the mass of the active materials on the working electrode in g, and ΔV is the scanned potential window in V (excluding the IR drop at the beginning of the discharge process).

The energy density, E, and power density, P, of the electrode materials were calculated from Equations (3) and (4), respectively,

$$E = \frac{C_s \Delta V^2}{7.2} \tag{3}$$

$$P = \frac{3600E}{t} \tag{4}$$

where E is the specific energy density in Wh/kg, P is the specific power density in W/kg, C_s is the specific capacitance in F/g, ΔV is the scanned potential window (excluding IR drop at the beginning of the discharge process) in V, and t is the discharge time in s.
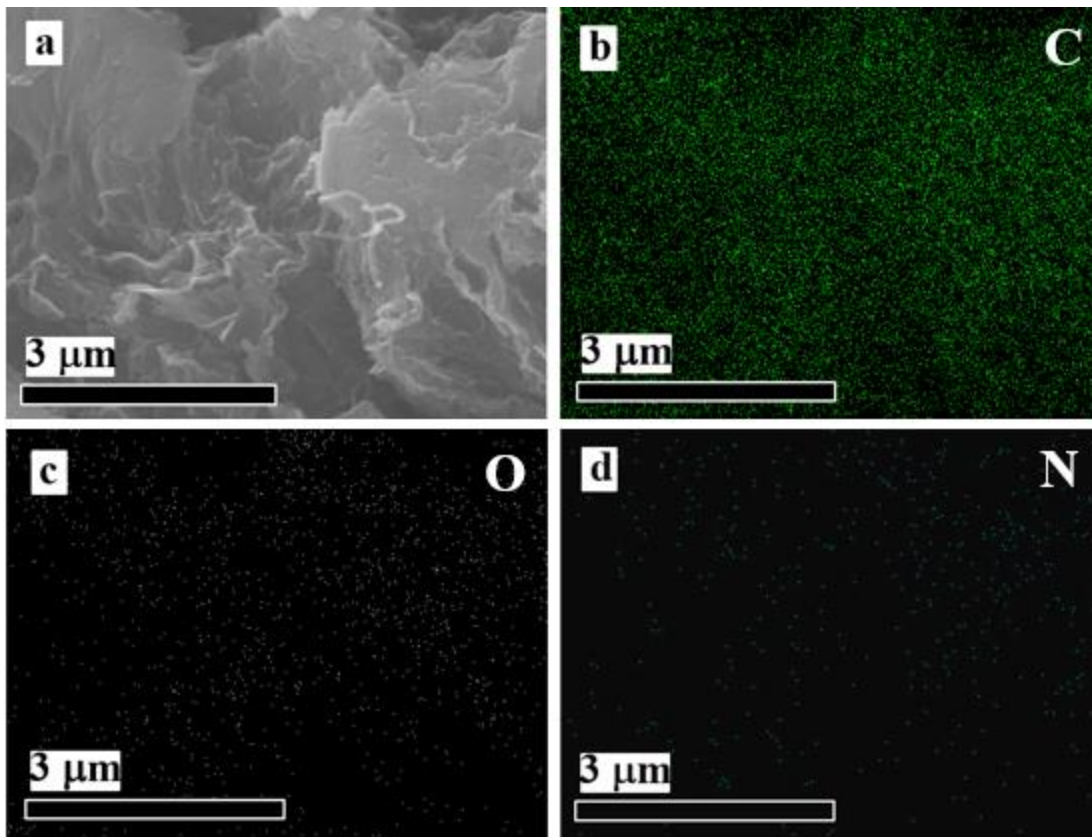
168

Figure C5.7. (a) SEM image of NG and corresponding EDS images of (b) C, (c), O and (d) N.
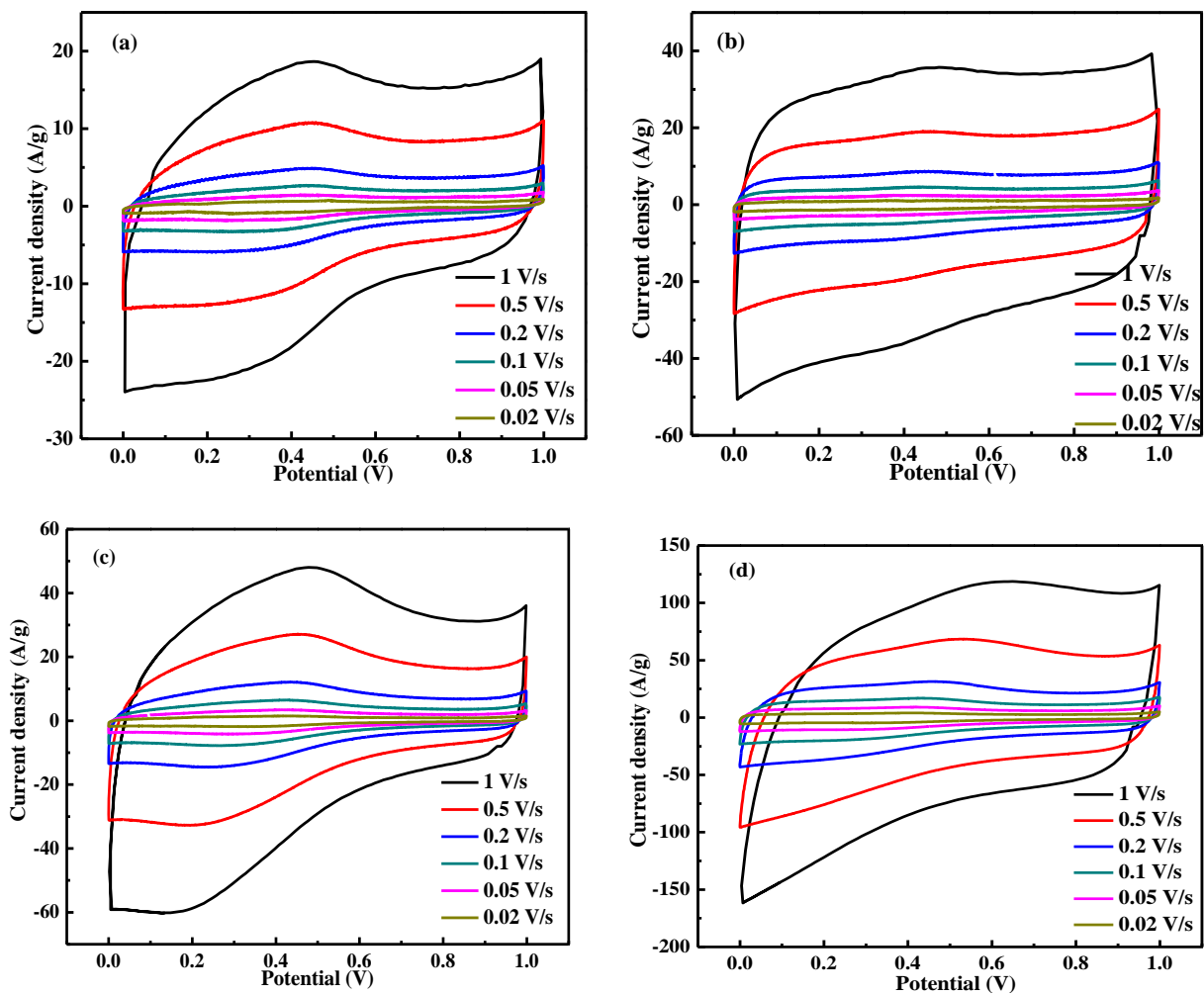
Figure C5.8. CV curves of (a) RGO, (b) N-G, (c) AG and (d) N-AG in 1.0 M H$_2$SO$_4$ with different scan rate ranging from 0.02 to 1 V/s.
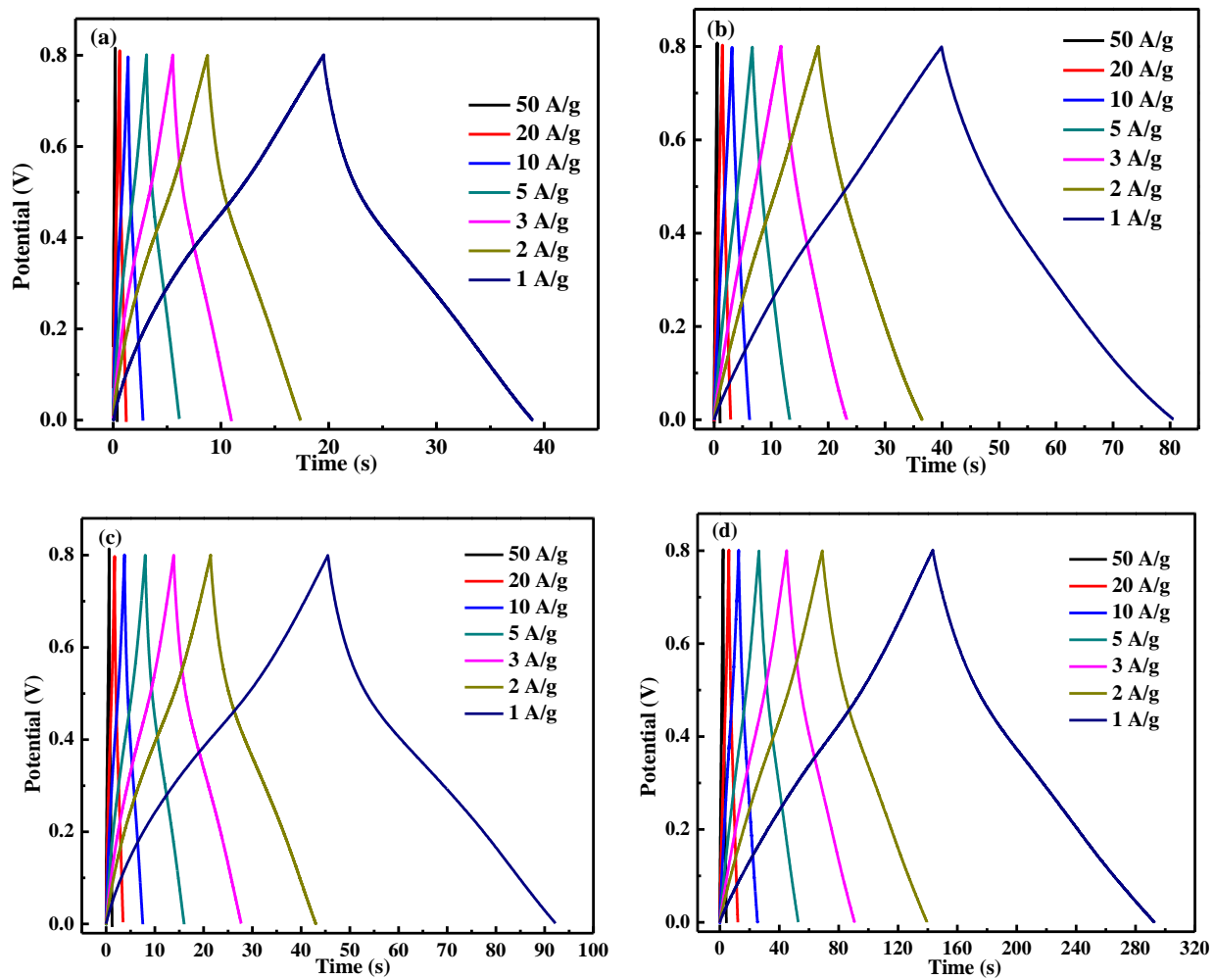
Figure C5.9. Charge−discharge curves of (a) RGO, (b) N-G, (c) AG and (d) N-AG in 1.0 M H2SO4 with different current densities ranging from 1 to 50 A/g

Chapter 6 Conclusions and Future Work

A series of innovative electrode nanocomposites have been synthesized in this dissertation and applied in energy storage and conversion systems such as fuel cells, supercapacitors and electrochromics. The nanocomposites fabrications can not only overcome the inherent drawbacks of each simple component but also incorporate all the advantages of specific components into one nanocomposite that finally improve the performances and widen their applications. In Chapter 2, Pd/MWNTs catalysts with different Pd loadings have been prepared by simple thermal decomposing different amount of $Pd(acac)_2$ in the presence of amount-fixed MWNTs-COOH in a refluxing xylene solution. Increased Pd NPs size and loading were clearly observed with increasing the $Pd(acac)_2$ precursor amount. Clear agglomerations were observed in high Pd loading nanocatalysts due to the saturation of defects on the tube wall surface. Increased Pd loadings with decreased precursor conversions were calculated from TGA result with increasing the $Pd(acac)_2$ amount. The electrochemical performance toward EOR demonstrated that Pd/MWNTs-2:1 gave the highest specific Pd activity and tolerance stability. However, EIS, LSV and corresponding Tafel characterizations showed greatly declined charge transfer resistances and enhanced reaction kinetics with increasing the Pd loading. Combined investigations of the precursor conversion and catalytic activity imply that Pd/MWNTs-2:1 exhibited the best catalytic performance towards EOR with economic synthesis. In Chapter 3, hierarchical FePd-Fe_2O_3/MWNTs nanocatalysts as ultrafine FePd alloy deposited on Fe_2O_3 NPs which were further evenly distributed on MWNTs have been successfully prepared by simple thermal decomposing $Pd(acac)_2$ and $Fe(CO)_5$ in a refluxing DMF solution in the presence of MWNTs-COOH. The formation of FePd alloy has been successfully confirmed by the crystalline structures and composition investigations through XRD and XPS spectra. The unique hierarchical structure has also been disclosed by TEM. Electro-characterizations such as CV, CA and EIS demonstrated an enhanced catalytic activity of the FePd-

Fe$_2$O$_3$(3:5)/MWNTs nanocatalysts towards EOR compared with Pd/MWNTs. Modified electronic properties of Pd by Fe, easily proceeded poisoning species on Fe$_2$O$_3$ and the optimal component ratios of PdFe, Fe$_2$O$_3$ and MWNTs substrate are mainly account for the greatly enhanced catalytic performance. In Chapter 4, a PANI matrix embedded with MnFe$_2$O$_4$ particles hybrid film has been successfully prepared by electrodepositing PANI monomers onto a MnFe$_2$O$_4$ coated ITO glass. A multi-color electrochromic phenomenon displayed at different potentials has been observed in this nanocomposites film due to the dominant PANI component in the composites. A higher coloration efficiency and a faster switching response than that of the pristine PANI film have been obtained due to the inner interactions between the PANI matrix and the MnFe$_2$O$_4$ particles as well as the resulted rougher morphology. The PANI/MnFe$_2$O$_4$ nanocomposites film also exhibits an enhanced areal capacitance compared to that of the pristine PANI film at low scan rates due to the capacitive role of MnFe$_2$O$_4$ and the rougher morphology. A negative role of increasing H$_2$SO$_4$ concentration on the energy storage behaviors of pristine PANI and PANI/MnFe$_2$O$_4$ nanocomposites films has been demonstrated by the increased R_{ct} values. The positive role of increasing the temperature during the relative low temperature range on both the pristine PANI and PANI/MnFe$_2$O$_4$ composites films has been obtained due to the greatly facilitated mobility of ions. However, both fast degradations of pristine PANI and PANI/MnFe$_2$O$_4$ nanocomposites films structure have been observed which implies a destroying role of the relatively high temperatures. The enhanced electrochromic and capacitive behaviors of the easily produced PANI/MnFe$_2$O$_4$ film make it suitable for application in devices integrating both functions of electrochromic and energy storage. In Chapter 5, a facile hydrothermal synthesis method combining KOH activation and N-doping was successfully employed to synthesize nitrogen doped activated graphene. This method is economically and effectively at a very high yield, implying feasibility for mass production. The

synthesized N-AG exhibited relatively decreased oxygen containing groups with increased defects due to the etching nature of KOH, the N-doping purpose can be successfully achieved by this effective N doping method. These unique properties endow the synthesized N-AG as a promising electrode for supercapacitors with high capacity, excellent rate capability, and long-term stability.

For future plans, since it's proved that the electrochemical and physical properties of carbon materials are extremely sensitive to doped heteroatoms (N, B, S and P), the doped atoms can modify the energy band structure of carbon materials thus influence the electronic structure and chemical reactivity while maintaining the robust framework of the carbon. The heteroatoms doped carbon materials (x-C) are expected to contribute to the catalytic activity of Pd-based catalysts and the distribution status of Pd due to the altered electric structure and introduced defects. A possible future research project is to further synthesize Pd-based nanocatalysts by probing the suitable E, MO, and x-C species as well as optimizing the ratios to give the highest performance. In addition, for the combined energy storage and electrochromic applications, different nanofillers such as inorganic electrochromic materials and highly conductive materials will be further employed to synthesize multilayer PANI-based films to enhance the energy storage and electrochromic performances based on the introduced multicolor phenomenon and improved conductivity.

Vita

Yiran Wang was born in Henan, China. He enrolled in Professor. Zhanhu Guo's group at Lamar University and received his M.S degree in Chemical Engineering in December, 2014. After graduation, he transferred as a Ph.D student to the Chemical & Biomolecular Engineering Department at University of Tennessee, Knoxville. He continued his Ph.D study in Professor Zhanhu Guo's research group, and worked on carbon & polymer based nanocomposites for energy storage & conversion systems. Yiran Wang received a Doctor of Philosophy Degree in Chemical Engineering from the University of Tennessee, Knoxville in December, 2016.